UC Irvine

UC Irvine Electronic Theses and Dissertations

Title

Illuminating the Optical Properties and Photochemistry of Nitroaromatics in Different Atmospheric Environments

Permalink

https://escholarship.org/uc/item/2zh28465

Author

Dalton, Avery

Publication Date

2024

Peer reviewed|Thesis/dissertation

eScholarship.org Powered by the California Digital Library
University of California

UNIVERSITY OF CALIFORNIA,
IRVINE

Illuminating the Optical Properties and Photochemistry of Nitroaromatics in Different Atmospheric Environments

DISSERTATION

submitted in partial satisfaction of the requirements
for the degree of

DOCTOR OF PHILOSOPHY

in Chemistry

by

Avery Bryan Dalton

Dissertation Committee:
Professor Sergey Nizkorodov, Chair
Professor Craig Murray
Professor Joseph Patterson

2024

Chapter 2 © 2021 American Chemical Society
Chapter 3 © 2023 Royal Society of Chemistry
Chapter 4 © 2023 American Chemical Society
Chapter 6 © 2024 American Chemical Society
All other material © 2024 Avery Bryan Dalton

DEDICATION

To my grandma, Juanita. For always pulling for me.

TABLE OF CONTENTS

LIST OF FIGURES

LIST OF TABLES

ACKNOWLEDGMENTS

There are numerous people who have helped me accomplish the work in this dissertation, and words on a page cannot adequately express the depth of my gratitude. I will start by thanking my advisor, Prof. Sergey Nizkorodov, who gave me the license to learn and try new things. There have been many strange events in the world since I joined the group a few years ago, and knowing that Sergey would support me through it all allowed me to focus entirely on the science. Whether I was learning new programming languages, or reading extremely niche papers on excited state chemistry, he was always eager to hear what I was working on and willing to offer any advice he had. Especially when he would just randomly throw in these nuggets of information that somehow answered all of my questions at once. Beyond the science, he was always happy to drink coffee and chat about life in general, which was always much appreciated. Thank you Sergey for all of the support, I would not have accomplished this feat if not for you!

I am also exceedingly grateful to Prof. Craig Murray, who allowed me to spend some time working in his group in the summer prior to starting graduate school. Having moved all the way across country, I see this time as invaluable toward helping me adapt to graduate research and living in California. I learned so much about spectroscopy and photophysics while working on the LIF project.

I appreciate of all of the collaborators I have had the fortune of working with. Thank you to Prof. Joe Patterson for taking part in both my advancement and dissertation committees, even though I did not end up doing as much work on particle and phase behavior as I originally planned. Thank you to Dr. Dmitry Fishman, who was a huge help in the experiments and analysis for the ultrafast work in Chapter 4. Thank you to Dr. Lisa Wingen for all of your help and patience for the nitroindole project, and taking the time to share so much information about aerosol mass spectrometry. Last but not least, I extend my warmest gratitude to Prof. R. Benny Gerber and Dr. Natalia Karimova for their encouragement and patience while helping me learn to do excited state quantum chemical calculations, for allowing me to use their Q-Chem license, and for providing helpful edits on our manuscript.

I must also thank the American Chemical Society and the Royal Society of Chemistry for allowing me to reproduce my published works as part of this dissertation.

I appreciate the friends and colleagues who were always down for hikes, concerts, and surfing. To friends and fellow group members Lucia and Alex, thanks for always being willing to talk science, coffee, *or* cats, and for watching Freddie and Bob when I was out of town.

To Katherine, who wears the three hats of lab mate, business partner, and best friend, thank you for always having my back and pushing me to be better. I appreciate you always lending an (at least one) ear to hear me rant about why my calculations are failing or why my rate constants make no sense. When one of us failed we failed together, and when one of us succeeded we succeeded together, to the end that we are both now here!

Finally, to all of my family, I could have never accomplished this without your unwavering support. To my grandparents, thank you for always supporting me. And Mum and Dad, I know that me moving so far away was difficult and I hope to have made you proud! Your love and support pushes me to always be my best, and myself, and I would not have made it through the wackiness of these past few years without knowing that you had my back.

VITA

Avery Bryan Dalton

EDUCATION

Doctor of Philosophy in Chemistry	2024
University of California, Irvine	*Irvine, California*
Master of Science in Chemistry	2021
University of California, Irvine	*Irvine, California*
Bachelor of Science in Chemistry	2018
University of North Florida	*Jacksonville, Florida*
Associate of Arts	2016
Eastern Florida State College	*Melbourne, Florida*

RESEARCH EXPERIENCE

Graduate Research Assistant	2019–2024
University of California, Irvine	*Irvine, California*
Analytical Research Intern	2018–2019
Bacardi-Martini Product Development	*Jacksonville, Florida*
Undergraduate Research Assistant	2017–2019
University of North Florida	*Jacksonville, Florida*

TEACHING EXPERIENCE

Teaching Assistant	2019–2024
University of California, Irvine	
Chem 1A, General Chemistry I	Fall 2019, Winter 2020, Summer 2020
Chem 1B, General Chemistry II	Spring 2020
Chem 1X, General Chemistry Extra	Fall 2020, Fall 2021, Fall 2023
Chem 1LC, General Chemistry I Laboratory	Spring 2022
Chem M2B, Majors General Chemistry II	Winter 2021, Winter 2023
Chem M3LC, Majors General Chemistry III Laboratory	Spring 2021

Supplemental Instruction Leader	2018-2019
University of North Florida	
CHEM 4410, Physical Chemistry I	Fall 2018
CHEM 4411, Physical Chemistry II	Spring 2019

VOLUNTEER EXPERIENCE

Safety Representative *July 2021 - January 2024*

University of California, Irvine

REFEREED JOURNAL PUBLICATIONS NOT INCLUDED IN THIS DISSERTATION

K. S. Hopstock, V. Perraud, A. B. Dalton, B. Barletta, S. Meinard, R. Weltman, M. Mirkanian, K. Rakosi, D. R. Blake, R. Edwards, and S. A. Nizkorodov*, Chemical Analysis of Exhaled Vape Emissions: Unraveling the Complexities of Humectant Fragmentation in Electronic Cigarette Vapor, *ACS Chemical Research in Toxicology*, 2024, 34, *1000-1010*.

CONFERENCE PRESENTATIONS

Evidence of Photoacidic Characteristics by Nitrophenols in Organic Matrices
Informal Gathering on Atmospheric Science and Photochemistry, October 2023, Los Angeles, CA
Evidence of Photoacidic Characteristics by Nitrophenols in Organic Matrices
American Association for Aerosol Research conference, October 2023, Portland, OR
Investigating the matrix effects in the photochemistry of atmospheric nitrophenols
ACS Spring Conference, March 2023, Indianapolis, IN
Photosensitized degredation of secondary organic aerosol by nitrophenols
American Association for Aerosol Research conference, October 2022, Raleigh, NC
Influence of solvent on the electronic structure and photochemistry of nitrophenols
Informal Gathering on Atmospheric Science and Photochemistry, June 2022, Irvine, CA
Photochemical candy: Use of isomalt as a proxy for glassy organic aerosol
PACIFICHEM conference, December 2021, Virtual
Photochemical candy: Use of Isomalt as a Secondary Organic Aerosol surrogate
American Association for Aerosol Research conference, October 2021, Virtual
The Effects of Antioxidants Within Dark Fruit Extracts on Fission Yeast Morphology
UNF Natural Sciences Poster Session, October 2017, Jacksonville, FL

STUDENTS MENTORED

Eleanor Miko *2023-2024*

Summer Undergraduate Research Program Award winner

Maggie Chou *2022-2023*

Undergraduate Research Opportunity Program Fellow, Michael. E. Gebel Award winner

Scott Le *2021-2022*

Contributed toward publication

AWARDS

School of Physical Sciences Faculty Endowed Fellowship 2024
University of California, Irvine

Dissertation Fellowship 2024
University of California, Irvine

Chemistry Department Travel Award 2023
University of California, Irvine

Contributions to the Chemistry Department Teaching Program 2023
University of California, Irvine

AAAR Student Travel Grant 2022
American Association for Aerosol Research

Chemistry Department Travel Award 2022
University of California, Irvine

ACS Undergraduate Award in Physical Chemistry 2017
University of North Florida

ABSTRACT OF THE DISSERTATION

Illuminating the Optical Properties and Photochemistry of Nitroaromatics in Different Atmospheric Environments

By

Avery Bryan Dalton

Doctor of Philosophy in Chemistry

University of California, Irvine, 2024

Professor Sergey Nizkorodov, Chair

Nitroaromatics are a class of organic molecules that have historically shown great utility in agricultural, pharmaceutical, and explosives industries. Though their use in pesticides has been phased out in the United States, studies of atmospheric aerosol have shown that a significant amount of these molecules still persist in the environment. A subclass of these molecules called nitrophenols have been shown to form naturally through the combustion of plant material. This process, called biomass burning, can produce individual nitrophenol concentrations that reach as high as 0.1 $\mu g/m^3$. Since these molecules are also often strong light absorbers, they often are responsible for a significant portion of visibility degradation by atmospheric aerosol. The goal of this thesis is to investigate the unique optical properties of nitroaromatics and use these results to better understand the processing of nitroaromatics in the atmosphere.

Nitrophenols can exist as a handful of isomers, but the most common forms in ambient samples are 2-nitrophenol and 4-nitrophenol. The latter, 4-nitrophenol, is heavily used in the textile industry even today, and there is a large pool of work being done to find efficient ways to remove this molecule from industrial waste waters. The second chapter of this dissertation evaluates the effects of different solvents, namely water and 2-propanol, on the photochemistry of 2-nitrophenol, 4-nitrophenol, 2,4-dinitrophenol, and 2,4,6-trinitrophenol. UV/Vis absorption is

used to track changes in nitrophenol concentrations. Electronic structure calculations provide insight into the energetics of states suspected of being involved in photochemical reaction pathways. Of all of the nitrophenols evaluated in this work, solvent has the strongest effect on the electronic properties of 2,4-dinitrophenol.

The third chapter of this dissertation expands on the role of the surrounding matrix, switching from liquid solvents toward solid organic glasses, on the photochemistry of 2,4-dinitrophenol and 4-nitrocatechol. A sugar-alcohol called isomalt is proposed as a laboratory-based surrogate for aging in secondary organic aerosol. Photochemical degradation is measured inside of the isomalt glass using a custom-built UV/Vis spectrometer setup. The efficiency of photodegradation of 2,4-dinitrophenol and 4-nitrocatechol is compared among solid and liquid matrices. The photochemical reaction rates of these compounds appear to scale with the viscosity of the encapsulating matrix but are still competitive when encapsulated in a glass.

Further inquiry into the importance of triplet states in 4-nitrocatechol photochemistry is explored in the fourth chapter of this dissertation. Ultrafast transient absorption spectroscopy is used to track which excited states are populated after excitation with a 340 nm laser pulse. Once again, the observations in water and 2-propanol are compared, revealing differences in excited state lifetimes of 4-nitrocatechol in each solvent. The roles of different excited states toward photodegradation are discussed. An excited-state proton transfer pathway appears to be the main outlet for excited 4-nitrocatechol in both solvents. In both the fourth and fifth chapters, the utility of quantum chemical calculations toward the estimation of intersystem crossing rates is also evaluated. For 4-nitrocatechol, these calculations are compared toward the described experiments. The fifth chapter shifts the focus to a simpler molecule, nitrobenzene, to try to minimize the likelihood of chemical processes interfering with interpretation of the ultrafast experimental data. Results from nitrobenzene calculations are compared to extensive work reported in the literature.

The sixth chapter of this dissertation attempts to unravel mysteries behind a strong chromophore that is observed in the secondary organic aerosol made from the reaction of indole and the nitrate

radical. Previous works suggest that it is a nitroindole, of which there exist seven possible isomers, and could not confirm which. The identity of the isomer is revealed in this work through a combination of chromatography and UV/Vis absorption spectroscopy. Further characterization is done with aerosol mass spectrometry, comparing the mass spectra of indole + NO_3 aerosol to those of aerosolized nitroindole standards. There are strong indications that nitroindole can reliably be observed with aerosol mass spectrometry, and that this molecule has previously been observed but unidentified in field samples.

This dissertation provides a detailed analysis of the photochemistry of nitrophenols and other nitroaromatic systems. Isomeric differences are evaluated for both nitrophenols and nitroindoles. The breadth of these analyses, ranging from solutions to solid organic glasses to aerosol, culminates in a deeper understanding of the atmospheric fate of this class of molecules.

Chapter 1

Introduction

1.1 Nitroaromatics in the Environment

Nitroaromatics are a class of organic molecules defined by the presence of an -NO_2 moiety on an aromatic hydrocarbon. The most well-known nitroaromatic molecule is likely trinitroluene (Fig. 1.1), usually referred to as TNT. Perhaps the most important modern source for these compounds in the atmosphere is through primary emission by the combustion of wood and other biologically derived matter, which has adopted the name "biomass burning". Various field campaigns have found nitroaromatics in the atmosphere in North America,[1–5] South America,[6,7] Africa,[8] Asia,[9–19] Australia,[20] and Europe,[21–30] usually in direct correlation to the combustion of biomass material. Highly functionalized nitro- molecules, such as 4-nitrocatechol, are some of the main products resulting from these burning processes.[3,10,14,31–34] In fact, 4-nitrocatechol is sometimes used as a tracer in ambient studies to associate the origin of a sample to a biomass burning event.[35–37]

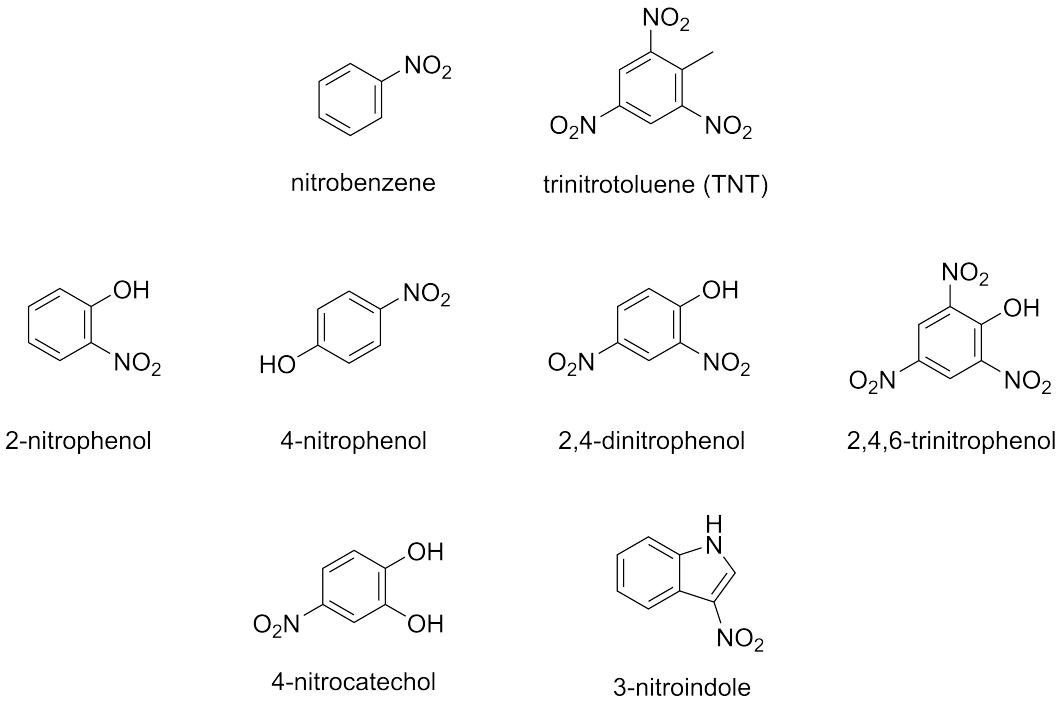

Figure 1.1: A selection of nitroaromatic molecules discussed in this dissertation.

In contrast to primary emission, these molecules can also be created in the atmosphere via chemical reactions between phenol and other benzene derivatives and nitrogen oxides (NO_x),

both of which are common components of "smog". When formed in the atmosphere, it is considered a secondary emission, as it was formed secondarily from other primary pollutants. Laboratory studies of secondary organic aerosol (SOA) generated from various single precursors have been shown to yield significant amounts of nitrophenols or nitrocatechols.[38–43]

The anthropogenic origins of these nitroaromatics in the atmosphere have decreased significantly as a result of cleaner vehicle emissions. It is worth acknowledging that this class of molecules is also utilized in agriculture, ammunition, pharmaceuticals, and even cosmetics. Given this utility, there are numerous other ways in which nitroaromatics can end up in the environment. Due to their negative toxicological effects, primary emission through agriculture has been reduced in the United States, and many of these compounds were included in the Priority Pollutant list as part of the 1977 Clean Water Act. There is still ubiquitous use (and release) of these compounds in other parts of the world, particularly with the use of nitrophenols in dyes for the textile industry. While the contamination from most of these industries is usually limited to soil and surface waters,[44,45] pesticides are susceptible to being swept into the atmosphere mechanically via the wind and overspray during application.[46]

Once in the atmosphere, these molecules are subject to the dynamic processes of atmospheric chemistry driven by physical conditions such as wind (transport), temperature, and humidity, and the presence of sunlight. In trying to understand the fate of these molecules in the atmosphere, and to extrapolate conclusions toward their effects on air quality, it is important to investigate the aging processes of these molecules under different conditions. This thesis will address the photochemical aging of nitroaromatics, with a focus on the role that the surrounding (liquid) solvent or (solid) matrix plays in their degradation pathways.

1.2 The Role of the Matrix on Molecular Photochemistry

The chemical environment, commonly known as the matrix, surrounding a molecule significantly influences its photochemical fate. From a chemical perspective, different matrices will have varying reactivities, which will affect a molecule's ability to undergo indirect photochemical reactions. The physical properties of the matrix can also play a role, by limiting processes such as diffusion or bond rotation.

The relevant chemical environments to the atmosphere are the gas phase, the aqueous phase, and the aerosol phase, although there is significant overlap between the latter two. In the gas phase molecules are dispersed, favoring unimolecular photochemical processes. Indirect photochemical processes in the gas phase are dependent upon the collisions between reactant molecules and are highly sensitive to the lifetimes of the excited states in the molecule. Conversely, molecules in the condensed phases are in constant contact, and molecular arrangements are driven by dipole interactions, which can have significant effect on possible chemistry.

For some molecules, such as nitrophenols, their optical properties in the aqueous phase are strongly dependent on pH of the matrix. Cloud water pH is notably variable, typically ranging from acidic to neutral (pH 3-7).[47,48] For instance, 2,4-dinitrophenol is likely to be deprotonated in cloud water, given its pKa of approximately 4.1.[49,50] The anions of nitrophenols have red-shifted absorption spectra (compared to their neutral counterparts),[50,51] leading to stronger absorption of visible radiation and altering their photochemical behavior.

The aerosol phase is less well-defined, as aerosol may be composed of liquids, solids, or semi-solid particles. Given that aerosol particles are predominantly organic compounds with diverse functionalities, they provide numerous pathways for indirect photochemical reactions. The molecules in the bulk organic phase are less polar than water, which could be important for the stability of reaction intermediates. Organic molecules also exhibit a wide range of viscosities, resulting in semi-solid or glassy particles,[52] particularly at the lower temperatures of the atmo-

sphere. The photochemical reaction pathways of molecules are less understood in highly viscous systems. Photolysis experiments conducted in a viscous organic material suggested that higher viscosity does indeed effectively decrease the photolysis rate of 2,4-dinitrophenol, however, the complex chemical composition of the organic material also varied from the octanol reference matrix used.[53]

Heterogeneous chemistry between all of these phases is also of interest, as studies have shown that adsorption of nitrophenols onto aerosol surfaces can show shifts in their absorption spectra akin to deprotonation in the aqueous phase.[50] It is clear that chemical environment can play a role significant role in the optical properties of nitroaromatics, although more work is necessary to characterize their photochemistry in matrices beyond the gaseous and aqueous phases.

1.3 Photochemistry

The term photochemistry refers to the interactions between molecules and electromagnetic radiation (more commonly known as light). Photochemical reactions usually involve the absorption of individual units of light, called photons, which induce some chemical change. More precisely, it is the energy of the photon, $h\nu$, that is transferred to the molecule and makes it available for chemical reactions. If the energy gained by the molecule directly results in the breakage of chemical bonds, the process is called photolysis (Reaction R1.1).

$$X + h\nu \rightarrow \text{products} \tag{R1.1}$$

Many photochemical processes do not directly result in bond breakage. Instead, the energy of the photon can be retained by the excited molecule (X*) and then later be transferred to a neighboring molecule (M). The products of this process, shown in Reaction R1.2-4, will depend on the characteristics of both X and M. In solution, neighboring M molecules are most likely to

be the solvent (as opposed to another X molecule); however, in a solid particle the identity of M will depend on the structure of the encapsulating matrix.

$$X + h\nu \rightarrow X^* \tag{R1.2}$$

$$X^* + M \rightarrow \textit{products} \tag{R1.3}$$

$$X^* + M \rightarrow X + M + \textit{heat} \tag{R1.4}$$

Whether a molecule undergoes direct photolysis (R1.1) or another indirect photochemical pathway (such as R1.2-4) depends on the energy of the photon and the electronic structure of the molecule. Most functionalized organic molecules will undergo direct photolysis at wavelengths shorter than 300 nm. At longer wavelengths, indirect photochemical pathways are more important. Crucially, not every absorbed photon will result in a reaction. Even if photolysis is possible at a given wavelength, it may not be probable. In many cases, the process in R1.4 is most likely to occur, with the excess energy in X* being transferred to the solvent in the form of heat. The probability that a molecule will undergo a photoreaction is incorporated into a unitless value called the photochemical quantum yield, ϕ.

$$\phi = \frac{\text{\# of molecules which react}}{\text{\# of molecules which absorb a photon}} \tag{1.1}$$

In the event that the molecule does not react, the absorbed energy may be transferred to the solvent in the form of heat, or a photon can be emitted via fluorescence or phosphorescence. In these cases, the original molecule remains intact, and no new products are formed. Each one of these pathways will have its own quantum yield, to the end that the quantum yields for all pathways sum to unity. Quantum yields have a non-trivial dependence on the wavelength and depend heavily on the electronic structure of the molecule, and its immediate environment. Obtaining true values for ϕ is difficult and requires the use of light-sources with very fine bandwidths. To

get around this, it is common to compute an averaged quantum yield over a range of wavelengths, which is usually denoted as $\langle\phi\rangle$. One can calculate an average quantum yield for a photochemical removal of a compound from experimentally measured first-order loss rate constants with Equation 1.2,

$$\langle\phi\rangle = \frac{k}{\int_{\lambda_1}^{\lambda_2} F(\lambda)\sigma(\lambda)\, d\lambda}\,, \tag{1.2}$$

where k is the first-order rate constant for the photochemical loss, $F(\lambda)$ is the spectral flux density which quantifies the number of incident photons per unit area and time with each wavelength λ, and $\sigma(\lambda)$ is absorption cross section for the molecule being irradiated. The limits of integration, λ_1 and λ_2, are either chosen based on the overlap between $F(\lambda)$ and $\sigma(\lambda)$ or by the wavelength range of the light source. The pitfall of using an average quantum yield is that wavelength-dependent information for ϕ is lost; however, $\langle\phi\rangle$ can be particularly useful when the objective is to estimate the lifetime (= $1/k$) of a molecule in the environment.

1.4 Quantum Chemistry and Excited States

The process in which a molecule absorbs a photon is inherently quantum mechanical in nature, and quantum chemistry provides a framework for the computational investigation of problems in photochemistry. The state of the electrons, such as their orbitals and energies, make up the electronic structure of a molecule. The study of quantum chemistry has produced many mathematical frameworks that can be used to solve problems related to the electronic structure of molecules. The basis of the field is built upon solving the Schrödinger equation, shown in Equation 1.3.

$$\hat{H}\Psi = E\Psi \tag{1.3}$$

The electronic system is described by the wave function, Ψ, and $\hat{H}$ represents a time independent Hamiltonian operator. When the Hamiltonian is operated on the wavefunction, it produces a constant E which represents the total energy of the system. The Hamiltonian is composed of individual operators for calculating the kinetic energy of each electron, the potential energy of the interactions between each electron and each atomic nucleus, and the potential energy for the interactions between each electron. Due to the interactions between electrons, analytical solutions to the Schrödinger equation are currently impossible for most problems in chemistry, meaning approximations must be made to predict the electronic properties of a molecule.

The majority of the computational work in this dissertation employs Density Functional Theory (DFT). DFT fundamentally departs from the formal approach of explicitly describing the wave functions of individual electrons. Instead, it introduces the concept of the electron density, $\mathrm{n}(r)$, as the molecular property that encapsulates the behavior of the electronic system. Despite such a grand approximation, DFT can be exceedingly accurate when characterizing the properties of small organic molecules. This accuracy, combined with computationally efficient calculations, makes DFT a common choice for providing context to experimental observations.

For problems in photochemistry, an extension beyond traditional ground state methods is required. Several excited-state methods exist, the most accurate of which is often considered to be the equation of motion coupled cluster method (EOM-CC). There is also an extension of DFT in the form of time-dependent density functional theory (TDDFT) which, like its ground state precursor, combines relatively low computational expense with fine accuracy.

The result from a TDDFT calculation is rich with information for each excited state, including both the potential energy of the state and the vertical excitation energy of the state (taking the Franck-Condon principle into account). Additional tools are commonly added to modern quantum chemical programs that allow for expanded analyses of excited states, such as computing different types of coupling and expanding visual interpretation of orbitals involved in each transition beyond the traditional HOMO-LUMO approach. As will be discussed in the dissertation, the nature of the orbitals can be used to help predict the likelihood of intersystem crossing processes.

1.5 Previous Work on Nitrophenol and Nitrocatechol Photochemistry

Of all molecules in the nitrophenol class, none have been studied as extensively as 2-nitrophenol (sometimes called o-nitrophenol). Ambient measurements of 2-nitrophenol in the gas-phase report concentrations of ranging from 1 - 350 ng/m^3, though some of the higher measurements are in correlation to pesticides whose use has since been phased out.[21,54–57] Much of the intrigue in this molecule is inspired by its intramolecular hydrogen bond.[58] It is well established that in the gas phase 2-nitrophenol undergoes direct photolysis at tropospherically relevant wavelengths to form nitrous acid (HONO), with yields as high as 40%.[59–61] Given the importance of HONO toward atmospheric chemistry, namely as a source of OH radical in the atmosphere, further investigation was done on the condensed-phase photochemistry of 2-nitrophenol. Surprisingly, HONO formation from 2-nitrophenol is almost non-existent in the aqueous phase, likely due to disruption of the intramolecular hydrogen bond by the solvent molecules.[51]

In direct contrast to 2-nitrophenol, HONO production via photolysis of 4-nitrophenol is enhanced in the aqueous phase.[51] It was initially suspected that 4-nitrophenol undergoes direct pho-

tolysis via O-H bond breakage (resulting in a nitrophenoxy radical), however, more recent works have unveiled that excited-state proton transfer may be an important outlet for photoexcited 4-nitrophenol.[62] This is particularly important in the context of 4-nitrophenol being significantly less volatile than 2-nitrophenol, and subsequently, has much higher ambient concentrations in organic particles (order of ng/m^3) and cloud/rain water (order of µg/L).[24,63–65] The quantum yield for photolysis of 4-nitrophenol, including both direct and indirect pathways, is reported to be $\sim 10^{-4}$ in the aqueous phase. The formation of nitrous acid as a product accounts for ~10-20% of the total photolysis, and the products from other pathways are not well established. A study by Vione *et al.* found that 2,4-dinitrophenol is formed upon irradiation of NO_2^- (from $NaNO_2$) with 4-nitrophenol (or 2-nitrophenol) is the minor species in solution,[66] so it is possible that nitration occurs to some degree as a secondary pathway of nitrophenol photochemistry.

The most exhaustive analyses of photochemical products have been done on 2,4-dinitrophenol. Aqueous experiments by Barsotti *et al.* revealed nitrous acid yields are around ~10-20%, like 4-nitrophenol, suggesting the NO_2 group in the *para* position is the most labile.[51] Interestingly, the by-product of nitrous acid production from 2,4-dinitrophenol photolysis would be either (or a combination of) 2- and 4-nitrophenol, although these were not tested for. Hinks *et al.* used chromatographic separation to better identify the products from 2,4-dinitophenol photolysis, although results have only been provided for photolysis conducted in the organic solvent 2-propanol, and not the aqueous phase.[53] In the organic solvent, the formation of 2- or 4-nitrophenol was minor, suggesting nitrous acid formation is significantly less efficient in the alcohol solvent. Instead, products corresponding to reduction (R-NO_2 $\rightarrow$ R-NH_2) and dimerization were observed, although quantitative information regarding yields could not reliably be obtained. In combination these works illustrate the need for studies in both aqueous and organic matrices to produce a complete hypothesis on how these molecules evolve in the atmosphere.

Although 4-nitrocatechol is usually one of the most abundant nitroaromatics in ambient samples (when they are present),[6,37] little is known about its photochemistry. Many articles ac-

knowledge its presence in ambient samples of particulate matter, ranging from small (sub-micron) to large (PM_{10}).[2,67–69] The low vapor pressure and high water-solubility of 4-nitrocatechol has resulted in its use in many studies as a model compound for "brown carbon",[70–73] which is a component of organic aerosol that produces a yellow/brown haze commonly observed in polluted air.

In the aqueous phase, studies by Hems & Abbatt determined that 4-nitrocatechol is particularly susceptible to OH oxidation, resulting in a lifetime in the atmospheric aqueous phase on the order of hours.[71] After a series of oxidation reactions, 4-nitrocatechol began to break down into smaller organic acids, effectively destroying the molecule. It is likely for this reason that 4-nitrocatechol is more abundant in atmospheric particles than cloud water. Molecules inside of particulate matter are less likely to undergo OH oxidation, since the highly reactive OH radical reacts at the surface before it can diffuse into particles.[74–76]

It is noteworthy that 4-nitrocatechol does not reciprocate this reactivity toward OH radical in the gas phase. An isomeric analysis of nitrocatechols by Roman *et al.* determined that 4-nitrocatechol has a lifetime greater than 48 hours, with respect to both OH oxidation and photolysis with 254 nm irradiation ($\mathcal{J} = 6.7 \times 10^{-5}$ s^{-1}).[77] Inefficient photolysis at such a short wavelength is surprising, given the rich photochemistry that nitroaromatic molecules tend to exhibit. These unique features inspire one of the main goals of this thesis: to better understand the dynamics and reactivity of photochemically excited 4-nitrocatechol, especially regarding the role the surrounding chemical environment plays in its relaxation/reaction pathways.

1.6 Structure of the Dissertation

This dissertation aims to shed light on the photochemical processes that nitrophenols can undergo, particularly in the context of atmospheric conditions.

The second chapter of this dissertation assesses how different solvents, specifically water and 2-propanol, affect the photochemistry of various nitrophenols. Complimentary UV/Vis absorption measurements and quantum mechanical electronic structure calculations were done to understand the degradation mechanisms of each nitrophenol. The results from this study will help identify the influence that chemical environment has on the removal of these molecules in the atmosphere. The third chapter expands the scope of the study by shifting from liquid solvents to solid organic glasses, investigating the photochemistry of 2,4-dinitrophenol and 4-nitrocatechol. A sugar-alcohol named isomalt is used as a lab surrogate to mimic aging in secondary organic aerosols, where photochemical degradation rates in solid and liquid matrices are compared using a specialized UV/Vis spectrometer setup. This work will provide a novel way of doing solid-phase photochemistry experiments and shed light on the importance of photochemistry in glassy atmospheric particles.

The fourth chapter delves deeper into the role of triplet states in the photochemistry of 4-nitrocatechol. Transient absorption spectroscopy was used to track the excited dynamics of 4-nitrocatechol, revealing solvent-dependent differences in the lifetimes of these states. The importance of various excited states in photodegradation, particularly through an excited-state proton transfer pathway, is analyzed. Given that triplet states are generally considered to be the longer-lived excited states in nitrophenols, this work provides an alternative pathway that may explain why this molecule persists in the atmosphere longer than other nitroaromatics.

Both the fourth and fifth chapters employ and discuss a framework for estimating the rate constants for the excited singlet-to-triplet conversion process, known as intersystem crossing, using parameters obtained from quantum chemical calculations. With the hopes of successfully applying the framework to support experimental findings with 4-nitrocatechol, the fourth chapter briefly introduces the concept of this framework, which ultimately fails to accurately describe the experimental observations. With the notion that this error could be due to the excited-state proton transfer that appears to occur for 4-nitrocatechol, Chapter 5 utilizes the same framework

for a simpler molecule, nitrobenzene, in which such a reaction is not possible. By comparison to experimental observations in the literature, the utility of the intersystem crossing estimation framework is discussed.

The sixth chapter of this dissertation deviates from nitrophenols and their derivatives to address an interesting phenomenon in the organic aerosol formed from the oxidation of indole by nitrate radical (NO_3). An isomeric analysis was conducted to identify which of the six possible isomers of nitroindole are the most abundant species in the particles. The identity of the isomer, which is 3-nitroindole, was confirmed via chromatographic and spectroscopic analyses. Aerosol mass spectrometry, a technique commonly used in ambient measurements, was done on an aerosolized 3-nitroindole standard to help future studies identify this molecule in real-world samples.

The goal of this dissertation is to further our knowledge on the optical properties of a handful of nitroaromatic molecules. With applications to atmospheric chemistry, the chemical environment is found to have varying levels of influence on the photochemistry of these molecules. This work ultimately shows that nitroaromatics, despite their similarities, do not all inherently undergo the same photochemical processes and must be treated on an individual basis to accurately predict their lifetimes in the atmosphere.

Chapter 2

Influence of Solvent on the Electronic Structure and the Photochemistry of Nitrophenols

Previous studies have suggested that the photochemistry of nitroaromatics in organic solvents can vary significantly from the photochemistry in aqueous solutions. This work compares the photodegradation of 2-nitrophenol (2NP), 4-nitrophenol (4NP), 2,4-dinitrophenol (24DNP), and 2,4,6-trinitrophenol (246TNP) in 2-propanol and water to better understand the photochemical loss of nitrophenols in atmospheric organic particles and aqueous droplets. Polychromatic quantum yields were determined by monitoring the loss of absorbance of each nitrophenol with UV/Vis spectroscopy in the presence of an acid (undissociated nitrophenol) or base (nitrophenolate). There was no orderly variation between loss rates in the organic and aqueous phases: 2NP and 4NP had similar yields in the two solvents. 246TNP was an outlier in these results as it dissociated in both acidified 2-propanol and water due to its exceptionally strong acidity. A notable result is that only for 24DNP was a dramatically increased reactivity found in 2-propanol compared to that in water. Time-dependent density functional theory calculations were carried out to

characterize the excited state energies and absorption spectra with a conductor-like polarizable continuum model or explicit solvation by a few solvent molecules. Explicit solvent calculations suggest the enhanced reactivity of 24DNP in 2-propanol is due to the strong interaction between a 2-propanol molecule and an $-NO_2$ group in the excited state. For the other nitrophenols, the solvent effects on electronic structure were minimal. Overall, the observations in this work suggest that solvent effects on the electronic structure and condensed-phase photochemistry of nitrophenols are minimal, with the exception of 24DNP.

2.1 Background

Nitrophenols first garnered scientific interest upon the discovery that these molecules exhibit phytotoxic characteristics and could potentially lead to forest decline.[78,79] This prompted questions about the fate of these molecules in the atmosphere, their overall lifetimes and chemical mechanisms of their atmospheric degradation.[59,66,71,80–86] Atmospheric sources of nitrophenols include both primary sources, such as automobile engines and biomass burning, and secondary sources, by reactions between phenols and NO_2 or NO_3 radicals.[10,20,31,80,87–89] The type of atmospheric loss that the molecule undergoes (i.e., reaction with an atmospheric oxidant or a photochemical reaction), as well as the phase in which the molecule is encapsulated in, have a strong effect on both the lifetime and the degradation products. While some processes change nitrophenols into phenols and catechols, the oxidation of these products in the presence of NO_x leads back to the formation of nitrophenols.[53,66,87,88]

Much of the previous study of nitrophenol photochemistry has been pinned around the production of HONO, which is itself a contributor to the oxidative potential of the atmosphere.[51,59,86] The chemistry of nitrophenols in the gas phase has been studied extensively– but considering the relatively low volatility of these species, evolution of these molecules in the condensed phases that are representative of atmospheric aerosol particles requires further investigation. While the release of HONO could have significant atmospheric implications, the importance of other photochemical pathways should not be overlooked. For instance, dimerization and functionalization have been shown to happen with these nitrophenol compounds.[40,84,90] The products of these reactions are less volatile and would be more likely to partition into, or remain trapped in, atmospheric particles.[40,91]

The importance of the chemical environment on the fate of nitrophenols and other nitroaromatics has been exhibited through experiments in both the aqueous and organic phases.[43,51,53,70,84,92] Gas phase studies have indicated that photochemistry of nitrophenols is comparable to the ag-

ing driven by hydroxyl or nitrate radicals, which is reported to have a lifetime around 330 h for 2-nitrophenol (2NP).[59,87] This resistance to gas-phase loss, in combination with the low volatility and high Henry constants of nitrophenols, grants more importance to condensed-phase processes. In the presence of organic compounds, for example, in organic aerosol particles, nitrophenols are thought to react through excited triplet states, abstracting a hydrogen atom from a neighboring solvent molecule.[93–95] The product of the H-atom abstraction will then go on to react further with nearby molecules. The influence of the chemical complexity of atmospheric organic aerosols creates a potential for numerous reactive partners and products which could have wide varieties of environmental impact.

In the condensed phase, photochemistry will also be impacted by the ionization of the molecule through acid-base processes, which causes changes in molecular extinction.[51] Barsotti et al. (2017) found that the anionic forms of a series of nitrophenols exhibited a greater yield toward photochemical loss of NO_2, in the form of NO_2^- or HONO, in the aqueous phase, accounting for 10-30% of the total photochemical yield of these molecules.[51] Importantly, this result also supports other photochemical studies of 4-nitrophenol (4NP) and 2,4-dinitrophenol (24DNP), in which multiple photodegradation pathways were observed.[66,83]

In laboratory experiments, photochemical degradation via hydrogen abstraction is generally slower in water than in an organic matrix, prompting a need for a better understanding of photoreactivity in the organic phase.[84] In contrast, in the aqueous phase photochemistry of nitrophenols the excited-state nitrophenol is expected to undergo a hydrolysis reaction with a neighboring water molecule, which is a major step in the production of HONO. These differing reactive pathways make predicting the reactivity of a nitrophenol in realistic atmospheric particles difficult.[43] Further, nitrophenols have relatively poor solubility in water, potentially amplifying the effects of photochemical loss in the organic phase of atmospheric particles. This work aims to investigate the photochemistry of a series of nitrophenols in an organic solvent under

simulated sunlight conditions, combining experimental results with ab initio calculations to give perspective to the relative reactivities of each nitrophenol.

2.2 Methods and Systems

2.2.1 Experimental Methods

The photochemistry experiments with 2-nitrophenol (2NP, TCI, 98%), 4-nitrophenol (4NP, Chem-Impex, 99.6%), 2,4-dinitrophenol (24DNP, Aldrich, 98%) and 2,4,6-trinitrophenol (246TNP, commonly referred to as Picric Acid, Sigma Aldrich, 98%) were performed without further purification of the stock chemicals. The solvents used in these experiments included 2-propanol (also known as isopropanol, Fisher, HPLC Grade) and water (Milli-Q Ultrapure). Although 2-propanol is a small molecule with only a single hydroxyl group, previous studies have shown that nitroaromatics have comparable rates of photodegradation in simple alcohols and in more complex secondary organic aerosol material.[53] While the rate of photodegradation is suppressed by the high viscosity of the secondary organic aerosol matrix, this suppression is counteracted by the higher diversity of reactive functional groups in secondary organic aerosol compounds.

To better understand the difference in photochemistry between undissociated nitrophenols and nitrophenolates, the experiments were carried out under acidic and basic conditions. In changing the pH of samples, small amounts of 1 N hydrochloric acid (Fisher) and 1 N potassium hydroxide (Fisher) were used. In the case of 246TNP, which has a pK_a of 0.4, an additional solution was made with 37% hydrochloric acid (Fisher) to reach [HCl] = 5 M to record the absorption spectrum of the undissociated form.

Photochemistry was carried out using radiation from a Xenon arc lamp, which was filtered and then directed onto the sample via a liquid light guide. The optical filters included a 280-400

nm dichroic mirror, followed by Schott BG1 (UV bandpass) and WG295 (295 nm longpass) filters. The overall power of the radiation reaching the sample ranged from 28-30 mW. With this setup, the near-UV spectrum of the radiation reaching the sample extended to lower wavelength (down to 280 nm) that of the ambient solar radiation (the lamp's spectral flux density is compared to that of solar radiation reaching the Earth surface in Figure 2.3). Liquid phase photochemistry experiments were conducted directly inside a Shimadzu UV-vis spectrophotometer, irradiating the sample vertically through the square opening in the top of a standard 10 mm UV/Vis cuvette (Starna Cells, 21-Q-10-MS). The cuvettes were filled to ∼80% of their volume, and the samples were not sealed and exposed to air permitting oxygen to dissolve in the solution. The oxygen concentration was not explicitly measured. The light guide was removed during each UV-vis scan to eliminate the interference scattering by the solution in the cuvette. In the case of 2NP, the sample was irradiated without the light guide since the degradation was much slower, subjecting the sample to ∼140 mW from the side of the cuvette.

Rate constants, *k*, for total photochemical degradation were obtained from fitting the loss in normalized absorbance to the fit shown in Eq. 2.1.[90]

$$A(t)/A(t=0) = C + (1-C)\,\exp\left(-kt\right) \tag{2.1}$$

This equation accounts for the formation of a single absorbing product, though it is possible multiple absorbing products could be formed. The absorption properties of the product are accounted for in the value C, which is a fraction of the extinction by the product to the extinction by the starting compound, $\varepsilon_{NP}/\varepsilon_{product}$.

2.2.2 Models and Computational Methods

All quantum chemical calculations were carried out using Q-Chem quantum chemistry package with the goal of giving context to the absorptivity and reactivity of the different nitrophe-

nols.[96] All geometry optimizations were performed at the B3LYP/6-31+G* level of theory. Time-dependent density functional theory (TDDFT) calculations were done to generate simulated excitation spectra using combinations of the B3LYP or PBE0 hybrid-exchange functionals,[97,98] which have both been shown to work well in other nitroaromatic systems.[99,100] With the variation of chemical features within this series of nitrophenols, each of the 6-311+G(d) and 6-311++G(d,p), aug-cc-pVDZ and aug-cc-pVTZ, and def2-TZVPD and def2-TZVPPD basis sets were evaluated. The Tamm–Dancoff approximation (TDA),[101] which has been shown to produce good results in similar aromatic systems,[102] was employed for all results reported in this work. Excitation energies were calculated in the gas-phase, as well as in water and 2-propanol using the conductor-like polarizable continuum model (C-PCM),[103,104] employing the dielectric constants for each solvent at 25°C. Simulated excitation spectra were produced by a convolution of Lorentzian functions calculated from the oscillator strengths at each excitation wavelength. A half-width at half-maximum of 20 nm was used in all the presented data. Natural transition orbitals (NTOs) were calculated for the triplet states in 24DNP to evaluate the differences in electronic character between 2-propanol and water.[105,106]

A combination of C-PCM and an explicit solvation model was required to obtain more accurate spectra for 24DNP in 2-propanol. Explicit solvation by one and three 2-propanol molecules was tested. The initial geometries were set up with the solvent molecules relatively far away to try to mimic the liquid-like solution, however the geometry optimization inevitably brought these solvent molecules closer. The 2-propanol molecules were placed next to the functional groups to allow for hydrogen bonding to occur. In the case of solvation by one molecule, two scenarios were tested: one with the 2-propanol acting as a hydrogen-bond acceptor for the alcohol group and one with the 2-propanol acting as a hydrogen-bond donor to the *para* -NO_2 group. No change in the excitation spectrum was observed in the latter case, and those results are not reported. For solvation by three 2-propanol molecules, the previous two models were combined, and the third 2-propanol molecule was oriented with the alcoholic hydrogen near the *ortho* -NO_2 group. This same scheme was employed with water as the solvent.

2.3 Results and Discussion

2.3.1 Experimental Absorption Spectra

The shape of the absorption spectra changed drastically for each of the nitrophenols in 2-propanol solutions with added KOH (Figure 2.1). The absorption spectra of nitrophenols are known to depend on a variety of experimental conditions,[50,107] especially by changes in pH.[51] The pK_a values of 7.23 (2NP), 7.14 (4NP), 4.09 (24DNP), and 0.42 (246TNP) make it possible for undissociated nitrophenols and nitrophenolates to co-exist in atmospheric particles. The nitrophenolates examined in this work all exhibit a significant redshift in absorption upon the addition of a base, as anticipated based on other studies.[51,62,108,109] Even though the autoprotolysis constant for 2-propanol is several orders of magnitude lower than that for water,[110] all of the nitrophenols studied in this work ionized significantly in 2-propanol with the added base. As shown in Figure 2.1(d), it was difficult to prevent 246TNP from ionizing due to its strong acidity. The predominant species of 246TNP in 2-propanol solutions was the anion, even after acidifying with HCl at 10^{-3} M and 10^{-1} M concentrations. However, in a sample with HCl at a concentration of 5 M, the spectrum did shift significantly toward the UV.

These spectral differences between nitrophenol and nitrophenolates could be an important factor towards photodegradation since there is more actinic flux at these longer wavelengths, potentially amplifying the importance of the degradation of these species relative to the neutral counterparts. The solar flux between 400-500 nm is nearly two times stronger than the flux in the near-UV (300-400 nm), making nitrophenolates potentially more photolyzable. However, their photochemical quantum yields in the aqueous phase are lower than for the undissociated nitrophenols.[51] While most aerosol particles in the atmosphere are acidic, they do show a wide range of acidities,[111] and given the relatively high acidities of these molecules, it is reasonable to expect the nitrophenolate form to be present in some environmental conditions. Moreover, these nitrophenolates can potentially undergo a different photochemical pathway.[107]

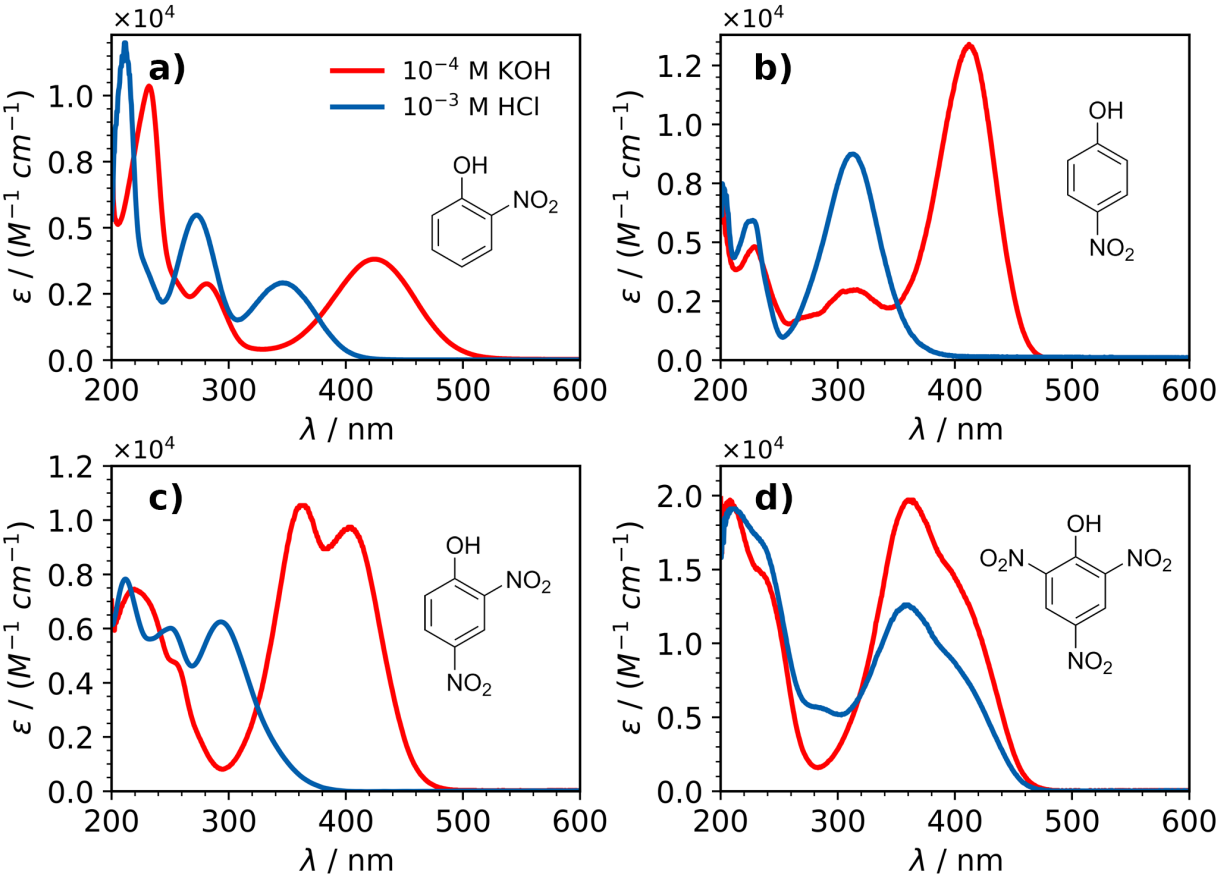

Figure 2.1: Spectrally resolved molar absorption coefficients of a) 2NP, b) 4NP, c) 24DNP, and d) 246TNP in a solution of 2-propanol with either co-dissolved KOH or co-dissolved HCl present, as indicated by color.

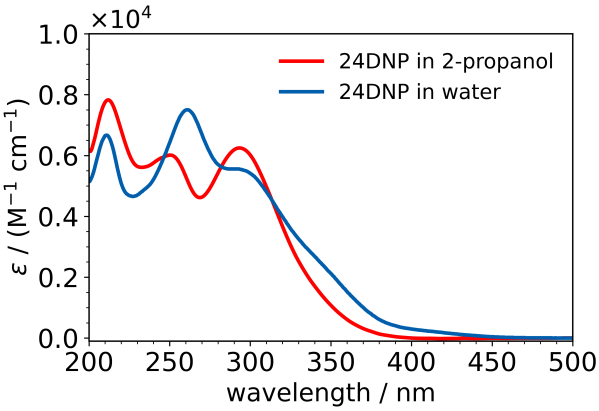

Figure 2.2: Molar absorption coefficients of 24DNP in acidified water (blue trace) and acidified 2-propanol (red trace) solutions.

Each of the undissociated nitrophenols exhibited absorption in the 200-400 nm range and showed no remarkable differences between the absorption spectra in acidified water and acidified 2-propanol, except for 24DNP. The absorption spectra 24DNP in these two solvents are shown in Figure 2.2, with the most notable difference being that the 260 nm peak in water is less intense and blue-shifted to 250 nm in 2-propanol. This difference can be explained by solute-solvent interactions, as discussed in more detail in Section 3.3.3 on calculated absorption spectra.

2.3.2 Photochemical Quantum Yields and Estimated Atmospheric Lifetimes

Photochemical quantum yields, $\langle\phi\rangle$, were calculated from the absorption-based rate constant and averaged over a 100 nm window, the approximate width of the main absorption bands. The absorption of each nitrophenol was monitored via UV/Vis for 3-5 h, depending on the reactivity of the nitrophenol. To account for the effect of light-absorbing products, rate constants were determined at the minimum of the normalized absorbance. This rate, k $[s^{-1}]$, can then be used

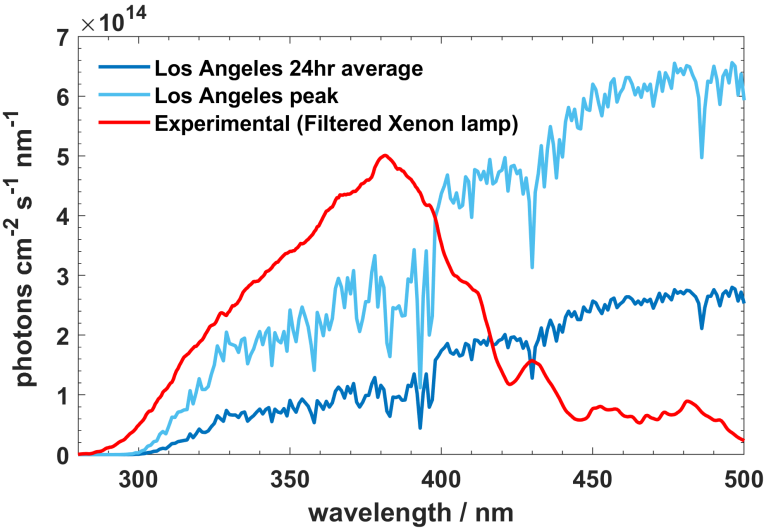

Figure 2.3: Spectral flux density of the irradiation source used to initiate photochemistry in these experiments is displayed in red. The dark blue trace shows the 24-h averaged flux for Los Angeles (1 July 2022) simulated with the National Center for Atmospheric Research (NCAR) Tropospheric Ultraviolet and Visible (TUV) calculator, used to estimate atmospheric lifetimes. The pale blue trace shows the maximum flux within the 24 h window. We used the 24-h average flux for the results reported in this paper, which is appropriate for molecules that have lifetimes exceeding 1 day. We note that for molecules with lifetimes <1 day, their actual ambient lifetime will be shorter during the peak of the solar irradiation.

in Equation 2.2 to determine the average quantum yield,

$$\langle \phi \rangle = \frac{k}{\int_{\lambda_1}^{\lambda_2} F(\lambda)\sigma(\lambda)\, d\lambda} \tag{2.2}$$

In this equation, $F(\lambda)$ is the experimental irradiation source shown in Figure 2.3, and $\sigma(\lambda)$ is the absorption cross-section of the molecule. The bounds of the integration, λ_1 and λ_2, correspond to the wavelengths +50 nm and -50 nm from the point of greatest decay. For example, for 4NP the most decay in normalized absorbance occurred at 319 nm, so the integration window was λ_1 = 269 nm and λ_2 = 369 nm. The only exception to this was 24DNP, which showed the most change at 235 nm, and the integration center-point was set to 290 nm, the approximate location of the main absorption peak. To determine estimated atmospheric lifetimes, Equation 2.2 was rearranged to solve for *k*, as was done in Eq. 3.2, using the experimental $\langle \phi \rangle$ and the 24-h average Los Angeles flux as $F(\lambda)$, and then taking the inverse of the rate constant to be the lifetime. A

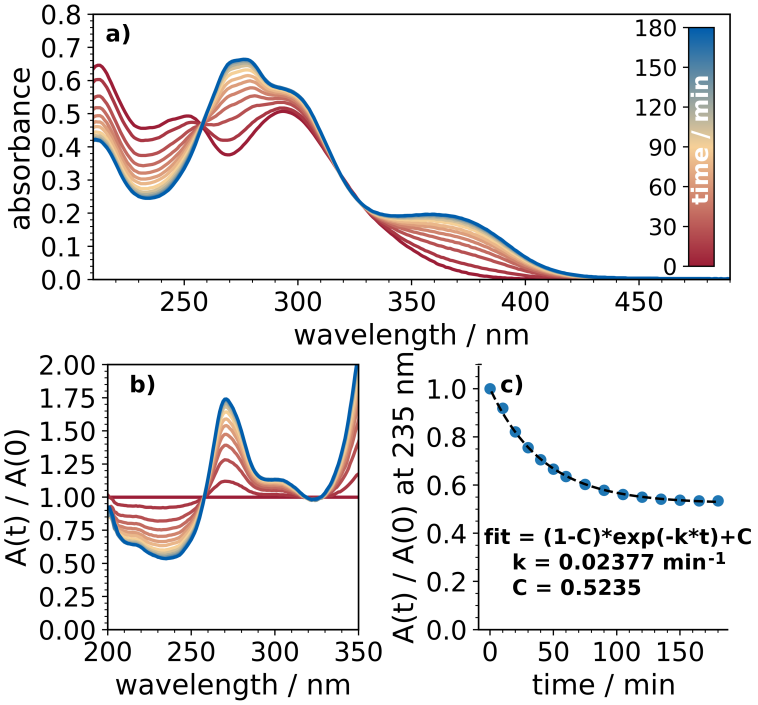

Figure 2.4: (a) The absorption of 24DNP collected over three hours of UV exposure, (b) the absorption of 24DNP normalized to the absorption spectrum obtained before photolysis began, and (c) the decrease in absorption at 235 nm, indicating loss of 24DNP, fit to Equation 2.1

comparison between the photon flux used in experiment to the simulated Los Angeles photon flux is shown in Figure 2.3.

The reactivity of these nitrophenols in acidified 2-propanol was typically greater than in basic conditions. Quantum yields and estimated atmospheric lifetimes for all of the nitrophenols are presented in Table 2.1. These averaged quantum yields were determined from the experimental rate constants with Equation 2.2. In acidic conditions, 24DNP was by far the most reactive, with a polychromatic quantum yield greater than 10^{-3}, and comparable to previous reports in octanol. The absorption spectra collected over 3 h of irradiation, along with the normalized absorbance and its decay are shown in Figure 2.4. Similar treatment for each of the other nitrophenols and nitrophenolates was used in determining each of the rate constants. In the discussion below, references are made to various values for aqueous photochemical yields from the literature which have been aggregated in Table 2.2.

Table 2.1: Total photochemical quantum yields in 2-propanol and approximate organic-phase atmospheric lifetimes for each nitrophenol (NP) in acidic and basic conditions.

Molecule	Average quantum yield	Atmospheric lifetime [h]
acidic conditions		
2NP	$(4.7 \pm 0.2) \times 10^{-6}$	1000
4NP	$(1.04 \pm 0.02) \times 10^{-4}$	37
24DNP	$(2.50 \pm 0.06) \times 10^{-3}$	3.8
246TNP	$(8.5 \pm 0.6) \times 10^{-5}$	3
basic conditions		
2NP	$(1.6 \pm 0.8) \times 10^{-6}$	3000
4NP	$(1.2 \pm 0.0) \times 10^{-4}$	4
24DNP	$(2.65 \pm 0.05) \times 10^{-5}$	19
246TNP	$(2.5 \pm 0.4) \times 10^{-5}$	3

Table 2.2: Referenced photochemical yields of undissociated nitrophenols in **aqueous** solutions.

Molecule	$\langle\phi\rangle$	Reference	Conditions
2NP	$(6.8 \pm 0.3) \times 10^{-6}$	This work	[HCl] = 10^{-3} M, broadband
	1×10^{-4}	Barsotti *et al.*, 2017	pH = 3, broadband
	4.7×10^{-6}	Alif *et al.*, 1991	pH = 2.2, monochromatic (365 nm)
4NP	$(9.9 \pm 0.1) \times 10^{-5}$	This work	[HCl] = 10^{-3} M, broadband
	(3.3 to 21) $\times 10^{-5}$	Lemair *et al.*, 1985	pH = 2, broadband
	4.3×10^{-4}	Einschlag *et al.*, 2002	pH = 2.5, broadband
	$(7.3 \pm 0.5) \times 10^{-4}$	Barsotti *et al.*, 2017	pH = 3, broadband
	$(1.4 \pm 0.1) \times 10^{-4}$	Braman *et al.*, 2020	pH = 3.5, broadband
24NP	1.3×10^{-4}	Einschlag *et al.*, 2002	pH = 2.5, broadband
	$(8.1 \pm 0.4) \times 10^{-5}$	Albinet *et al.*, 2010	pH = 2.5, broadband
	(3.6 to 4.4) $\times 10^{-6}$	Lignell *et al.*, 2014	Broadband
	$(2.1 \pm 0.1) \times 10^{-4}$	Barsotti *et al.*, 2017	pH = 3, broadband

In the condensed phase, both aqueous and organic, 2NP appears to be the least reactive nitrophenol. Our result of very low quantum yield in acidified 2-propanol greatly differs from a reported aqueous quantum yield of 1×10^{-4} in acidified solution with a very similar radiation source.[51] We conducted a similar aqueous experiment with [HCl] = 10^{-3} M and found the averaged quantum yield to be $(6.8 \pm 0.3) \times 10^{-6}$. These results are in closer agreement with those reported by Alif *et al.* (1991), who reported a monochromatic quantum yield of 4.7×10^{-6} at 365 nm.[112]

The quantum yield for 4NP in 2-propanol is in better agreement with the range of values previously reported under aqueous conditions. Again, the reactivity in the organic matrix is not much different than in aqueous solution. In an aqueous experiment we obtained a quantum yield of $(9.9 \pm 0.1) \times 10^{-5}$, which is within a factor of ∼5-8 from values reported in other works.[51,113–115] To put into perspective the results in the organic phase, the lifetime of 4NP in an aqueous solution containing co-dissolved a-pinene ozonolysis SOA compounds was ∼11 h.[113] Our result of ∼37 h in pure 2-propanol is reasonable given that 2-propanol is a less reactive partner compared to the molecules found in SOA.

No trends were observed for the anions of each NP. In the experiment for the 2NP anion there was a rapid shift in the spectrum during the first 45 min that appears to be caused by some re-formation of neutral 2NP. To account for this, the fit was applied only to the data after the first 45 min. Similar types of double fitting have been employed for other systems when it is apparent that there is a fast process and some other slower process.[43] This resulted in a more reasonable quantum yield of $(1.6 \pm 0.8) \times 10^{-6}$, which should be regarded as a lower limit due to the difficulty in decoupling photodegradation from acid/base equilibrium. For 2NP and 24DNP dissolved in 2-propanol, the yields were lower for the anions, which agrees with their photochemistry in aqueous solutions.[51,116] 4NP reacted more under basic conditions but the difference was negligible. Since 246TNP remained in the ionized form both in the presence of acid and base, no comparison can be made regarding its reactivity relative to that of the undissociated molecule.

The reactivity of the anion of 246TNP did change depending on the acidity of the solution. The effective quantum yield for 246TNP loss under acidic conditions is ∼3 times larger than that under basic conditions, however, the estimated ambient lifetime is about the same, largely due to the impact that the presence of HCl had on decreasing the amount of absorption at wavelengths greater than 300 nm.

It should be recognized that if multiple absorbing products are formed then Equation 2.1 will likely underestimate the loss rate constant, so the quantum yields listed in Table 2.1 likely represent lower limits. The presence of isosbestic points in these normalized spectra indicates minimal secondary photochemical processes occurred throughout the timescales of the experiments. Normally this would also indicate that only one product is formed, however, previous studies have observed multiple products from the photolysis of 24DNP and a similar molecule, 4-nitrocatechol, even with distinct isosbestic points in the absorption spectra.[84,90] Product analysis was outside the scope of this work and the quantum yields reported here represent total photochemical quantum yields of NP + hν $\rightarrow$ products.

The relatively low reaction rates indicate that the photochemistry has not gone to completion, except for 24DNP, within the short time scales of these experiments. This was anticipated, as experiments with 4NP in the aqueous phase reported by Braman *et al.* (2020) did not reach completion until around 10 h of irradiation.[113] The exception to this was 24DNP, which is the only NP where the loss appeared to have plateaued within the timescale of the experiment. 24DNP also provided the most notable difference between organic and aqueous phase photochemistry. Under acidic conditions, reported values for aqueous polychromatic quantum yields range from 10^{-6} to 10^{-4}.[51,84,115,116] The value of (2.50 ± 0.06) × 10^{-3} reported in this work strengthens the position that organic-phase photochemistry is significantly faster for 24DNP. This yield is slightly higher than the previously reported value (1.7 × 10^{-3}) in an octanol film, potentially due to the lower viscosity of 2- propanol.[84]

2.3.3 Simulated Absorption Spectra

Each of the nitrophenols exhibited absorption bands in the 200–400 nm range (Fig. 2.1). In the following discussion, the experimentally observed absorption bands will be referred to as 'A', 'B', 'C', etc. in the order of increasing excitation energy. Table 2.3 shows the calculated excitation energies for each nitrophenol, which bands they fall into, and their respective oscillator strengths.

All results shown in Table 2.3 account for solvent effects by using the C-PCM for 2-propanol. Generally, the simulated spectra in 2-propanol are in good agreement with the experimental data. The effect of the chosen basis set on the accuracy of each excitation spectrum was minimal in comparison to the effect of the exchange functional used. For the sake of consistency, all results reported in this work come from 6-311++G(d,p). The shapes of the respective spectra are similar between B3LYP and PBE0, but in every case, B3LYP produced lower excitation energies than PBE0. Previous studies with similar objectives of predicting absorption spectra have benchmarked these TDDFT methods against higher-level methods such as the Algebraic Diagrammatic Construction (ADC(n)) with good success.[117–120] The use of TDDFT/TDA worked relatively well for all of the systems in this work, so due to computational expense higher-level methods were not applied for these systems.

The excitation spectrum of 4NP was reproduced well with B3LYP, however, the excitation energies of 2NP and 24DNP were better served using PBE0. It is noteworthy that 2NP and 24DNP both have an intramolecular hydrogen bond while 4NP does not. The discrepancy between the methods may be due to the ability of PBE0 to yield more accurate energy values for hydrogen bonded systems.[121] This, and the fact that 4NP also exhibits significantly different properties (such as with respect to solubility and vapor pressure) from the others are the reasons for treating 2NP and 24DNP differently from 4NP in this work.

With 246TNP being an anion under all experimental conditions, the results for simulated spectra of the undissociated acid and the anion are presented only for the sake of completeness.

Table 2.3: Comparison between experimental and best-simulated absorption spectra for each nitrophenol.

System/Method	Band (λ_{exp} [nm])	λ_{sim} [nm]	Oscillator Strength (f)	$\Delta\lambda$ [nm]
2-Nitrophenol				
PBE0/6-311++G(d,p)	A (346)	352	0.099	+6
	B (272)	271	0.388	-1
	C (210)	215	0.016	+5
4-Nitrophenol				
B3LYP/6-311++G(d,p)	A (312)	311	0.502	-1
	B (225)	227	0.067	+2
2,4-Dinitrophenol				
PBE0/6-311++G(d,p)	A (350)	329	0.097	-21
without explicit solvation	B (293)	287	0.332	-6
	C (250)	261	0.376	+11
		254	0.172	+4
	D (212)	204	0.010	-8
		190	0.160	-22
PBE0/6-311++G(d,p)	A (350)	335	0.086	-15
with explicit solvation		333	0.027	-17
	B (293)	296	0.206	+3
		294	0.192	+1
	C (250)	264	0.263	+12
		256	0.304	+6
	D (212)	207	0.011	-5
		204	0.034	-8
2,4,6-Trinitrophenol				
PBE0/6-311++G(d,p)	A (342)	325	0.130	-17
		312	0.025	-30
	B (285)	280	0.124	-5
		278	0.055	-7
		273	0.025	-12
		269	0.120	-16
	C (245)	258	0.248	+13
		249	0.113	+4
		236	0.067	-9
		232	0.077	-13
		228	0.071	-17

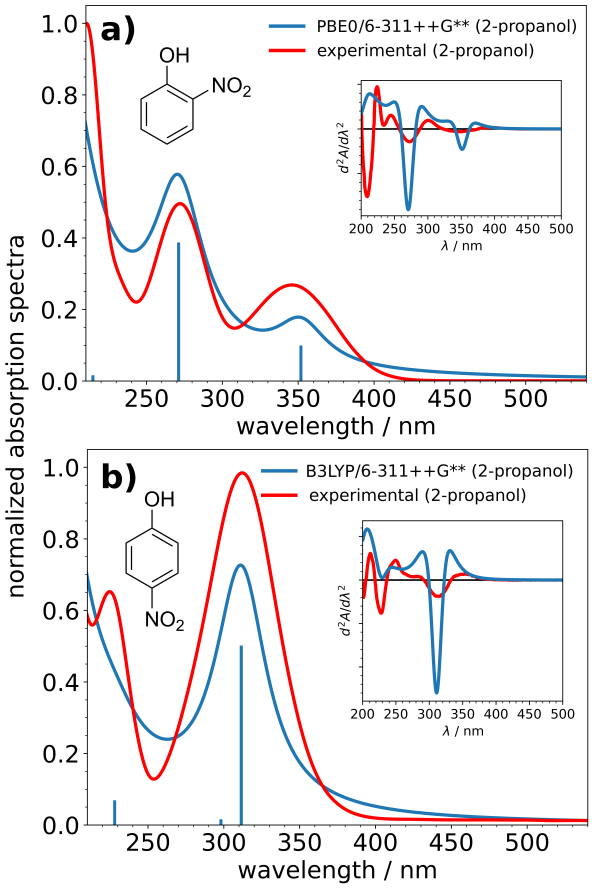

Figure 2.5: Simulated (blue) and experimental (red) absorption spectra of 2-nitrophenol (a) and 4-nitrophenol (b). The insets show the second derivative of the spectra to help identify the energy and breadth of each band. All spectra are normalized to the most intense band.

We do not report calculations for the other NP anions as it would require a different computational approach. Some theoretical calculations have been done with the nitrophenolates of 2NP, 3-nitrophenol, and 4NP with the CC2 coupled cluster model, providing varying levels of accuracy between each isomer.[107,122] It would be important, especially for the easily ionizable 246TNP, to expand on this work in follow-up studies. In the following sections the specific computation results for each molecule are discussed individually.

2-Nitrophenol and 4-Nitrophenol

Fig. 2.5a shows the excitation spectrum of 2NP simulated at the PBE0/6-311++G(d,p) level of theory. The experimental spectrum contains three distinct absorption bands, with a small shoulder apparent in the highest energy band. The theory comes close to reproducing the bands at 346 nm and 272 nm but overpredicts the energy of the highest energy band with an excitation at 189 nm. Fig. 2.5b shows the excitation spectra for 4NP. The B3LYP simulated spectrum has the best agreement with the experimental spectrum, unlike the other nitrophenols in this work which had the best agreement with PBE0. Both excitation bands in the UV region are within 2 nm agreement between theory and experiment. Again, the intensity of the short-wavelength band has been underestimated and the absorption in that range is dominated by a sub-200 nm excitation.

2,4-Dinitrophenol

We found that the C-PCM solvation method, which worked reasonably well for 2NP and 4NP, produced inferior results for 24DNP. This deviation is likely due to a combination of an increase in complexity of the aromatic system and, more simply, there being more atoms in the molecule.[123] The main shortcoming of C-PCM was underpredicting the energy of band C, which is comprised of two excitations, one at 261 nm (major) and one at 254 nm (minor). We carried out additional calculations with explicit solvation of 24DNP with up to three 2-propanol molecules to produce simulated spectra, and they were in better agreement with the experimental spectrum. The spectra produced from these calculations are presented in Fig 2.6. Upon adding explicit solvent molecules, the intensity of these two excitations flips, causing the shorter-wavelength excitation to become the most intense in the band, shifting band C to give better agreement with the experimental spectrum.

Ultimately, the spectral differences between 24DNP in aqueous and alcohol solutions could not be completely recreated by the theory used in this work. While the errors in relative inten-

sities could be due to the use of the Tamm-Dancoff approximation, the values for the excitation energies themselves should be more accurate.[124] It would be of interest to try more accurate methods to try to characterize the major blueshift in the C band that is observed when 24DNP is in an alcohol matrix. With regard to the atmospheric chemistry applications, where band A is the most critical transition to describe correctly, the results from these methods are sufficiently accurate. This excitation is poorly resolved in experimental spectra and has been roughly assigned to 350 nm in this work. Explicit solvation slightly red-shifted this excitation to give better agreement with experimental spectra.

2,4,6-Trinitrophenol

The simulated spectra for 246TNP and its anion are presented in Fig. 2.7. These spectra are comprised of numerous excitations within the UV region with relatively high oscillator strengths. In keeping with the convention used in this work, the undissociated form is presented with the PBE0 level of theory because the optimized ground state structure contains an intramolecular hydrogen bond. This structure is also shown in Fig. 2.7, with the notable feature of one of the NO_2 groups having rotated out from the mostly planar structure. The overall shape of the spectra is well matched, but the bands are composed of numerous excitations with various intensities. PBE0 was particularly better at predicting the excitations within the higher energy bands of 246TNP (B and C in Table 2.3), with B3LYP having significantly over-predicted them. As was seen with 24DNP, the main shortfall of the theory is under-predicting the separation of the two maxima of the experimental spectra, with $\sim$30% error in the separation between bands A and C.

2.3.4 Simulated Triplet States

Ultimately, theoretical calculations were done to better understand the role of excited triplet states in the photochemistry of these nitrophenols in organic matrices. It has generally been assumed

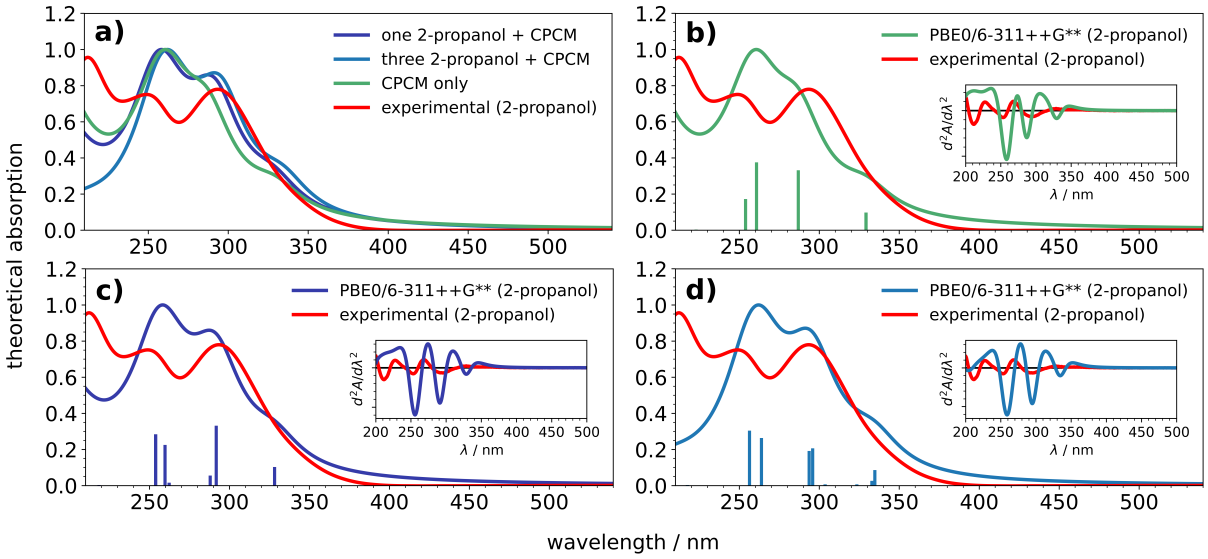

Figure 2.6: The experimental and theoretical spectra of 24DNP in 2-propanol as solvent. Panel (a) shows the spectra overlaid on each other, and panels (b), (c), and (d) show the individual spectra and oscillator strengths from simulations with C-PCM only, and one and three explicit 2-propanol solvent molecules, respectively.

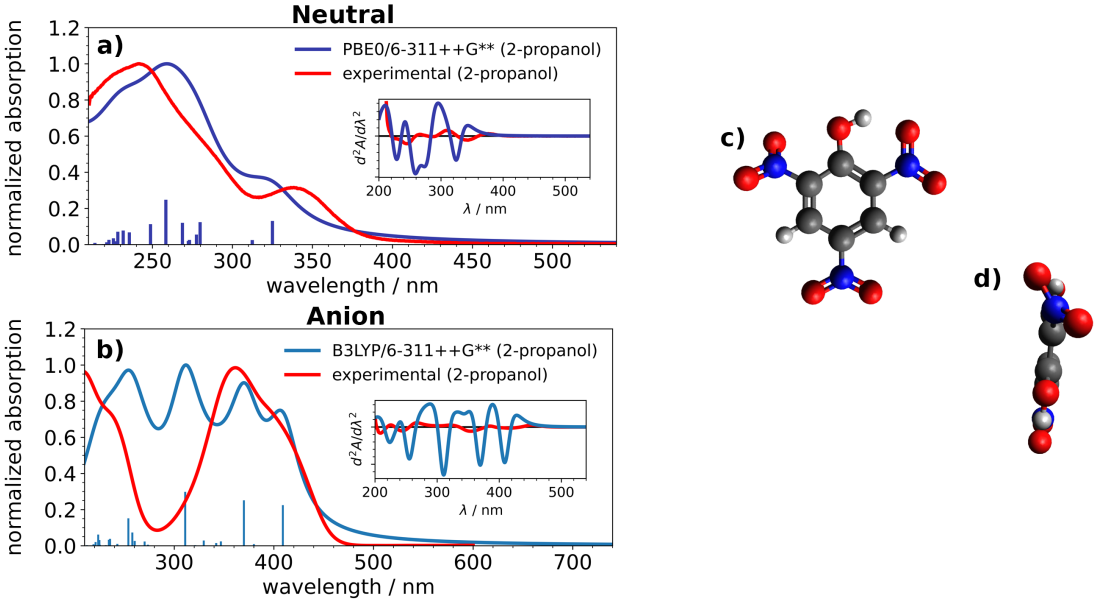

Figure 2.7: The experimental and theoretical absorption spectra of 246TNP as a neutral (a) and anionic (b) species in 2-propanol. The insets of these plots show the second derivatives of the absorption spectra. The optimized structures of the neutral form of 246TNP are shown in (c) and (d), with the latter having been rotated to show the rotation of the non-planar -NO_2 group.

that the photochemistry of nitrophenols goes through a triplet state, given that relaxation processes from excited singlet states are very fast in the condensed phase, as previously shown for nitrobenzene.[93,94] Triplet state lifetimes of nitrophenols are short and difficult to measure experimentally.[125] Previous studies found that 2NP is likely to undergo intersystem crossing via S_1 to T_3 followed by rapid (less than 0.1 ps) internal conversion to T_1.[126] Takezaki *et al.* found that the T_1 lifetimes (in benzene solvent) of 2NP and 4NP were 900 and 500 ps, respectively.[125] These ultrashort excited-state lifetimes are a common characteristic of these nitroaromatic type molecules, and it is surprising that they have enough time to react before returning to the ground state via a nonreactive and nonradiative relaxation pathway.[85,95,127–130] While there is no information about the photophysics of 24DNP, it is reasonable to expect the excited state lifetimes would be comparable to those of 2NP and 4NP. Given that 24DNP has the most efficient photochemistry, it would be of interest to directly study the photophysics of 24DNP with time resolved laser spectroscopy.

The calculated vertical excitation triplet state energies, E_{T_1}, for 2NP, 4NP, and 24DNP are presented in Table 2.4. The energies for 2NP and 4NP agree with those reported from calculations with the CAS-SCF method.[125] Though it is likely for these NPs to each enter the triplet manifold via an $S_1 \rightarrow T_{n>1}$ ISC process, the T_1 state should still be the longest lived and most likely to react photochemically.[126,131] The role of the triplet state in hydrogen abstraction by nitrophenols is not clear, though it is noteworthy that the energies of T_1 and the average quantum yields both increase in the order of 2NP $<$ 4NP $<$ 24DNP. The values of these energies are comparable to those found from chromophore dissolved organic matter, where the "high-energy" triplets were shown to be 2.6–3.1 eV.[132] The differences in energy, ΔE_{ST}, between T_1 and S_1 are also shown, to aid in providing insight into the stability of the T_1 states.

The reactivity of the triplet state in nitroaromatics was reported early on for nitrobenzene, and the reactive part of the molecule was proposed to be the $-NO_2$ group.[93,94] Theoretical studies of nitrobenzene and nitrophenols have observed similar importance of the $-NO_2$ group toward photochemistry.[85,131,133] Though it has been difficult experimentally to trap the reaction in this

Table 2.4: TDDFT energies for the first excited triplet and singlet states of each nitrophenol

Molecule	E_{T_1} **[eV]**		ΔE_{ST} **[eV] (T_1−S_1)**	
C-PCM	2-propanol	water	2-propanol	water
2NP	2.721	2.708	-0.804	-0.808
4NP	2.839	2.812	-1.141	-1.163
24DNP	3.077	3.071	-0.689	-0.690
24DNP (with explicit solvent)	3.035	3.018	-0.669	-0.692
246TNP	3.194	3.191	-0.622	-0.624

state, studies have found photoreduction products after irradiation.[84,134,135] Figure 2.8 displays the highest-strength natural transition orbital (NTO) pairs for the T_1 state of 24DNP. In these $\pi\pi^*$ transitions, most of the electron density gets shifted to the -NO_2 groups upon excitation, particularly in the orbitals for pair #2, supporting the suggestion that this is where the H-atom abstraction likely occurs. The same transition in water (as compared to 2-propanol) results in less electron density being shifted into the –NO_2 group, with the hydroxyl group retaining some electron density. In addition to the fact that 2-propanol has less strongly bound hydrogen atoms than water, this shift in electronic structure of the T_1 state of 24DNP could be playing a role in its enhanced reactivity towards alcohols.

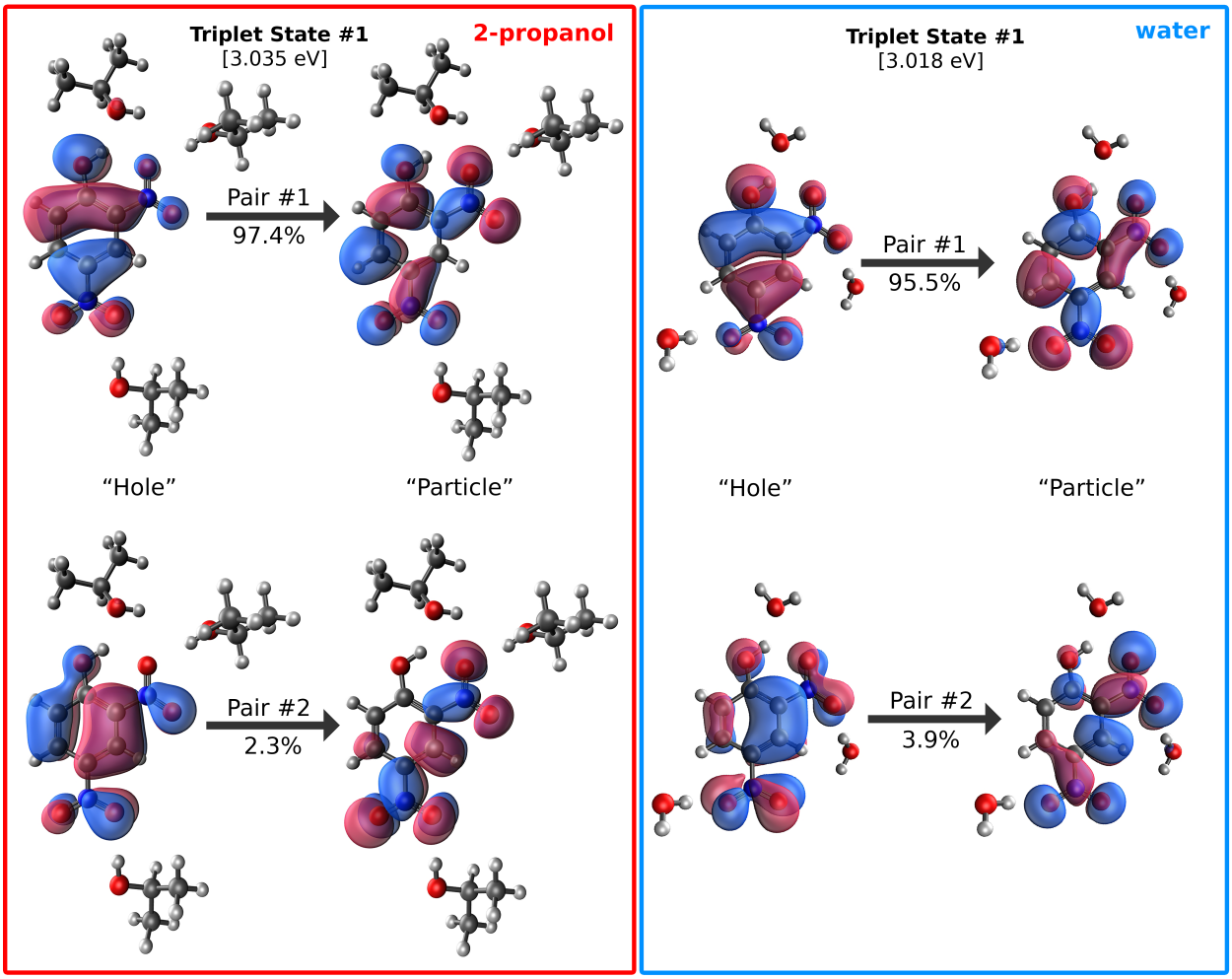

Figure 2.8: Natural transition orbitals for the first excited triplet state of 2,4-dinitrophenol calculated at the PBE0/6-311++G(d,p) level of theory and depicted with an isovalue of 0.05. A combination of explicit solvation (shown) and C-PCM was used to simulate a 2-propanol (red box) or water (blue box) solution.

2.4 Conclusions

This work has compared the photochemistry of nitrophenols in 2-propanol to that in water to better understand their photochemical transformations in atmospheric organic particles. Experimental measurements of the quantum yields for polychromatic photodegradation showed nitrophenols do not follow a well-defined trend with the number of nitro groups in the molecule. Of

the molecules studied, 24DNP with two nitro groups turned out to be far more photolabile than nitrophenols with one or three nitro groups. Theoretical calculations were performed to characterize the excited states of these nitrophenols, and how they vary between aqueous and organic solutions. Theoretical absorption spectra were in good agreement with experimental spectra, with the predicted excitation energies typically falling within 5 nm from the experimentally observed absorption bands. The relative energies of each nitrophenol's T_1 state did not show a strong dependence on solvent.

While 2NP and 4NP showed little difference in reactivity in water versus 2-propanol, 24DNP showed a significant (factor of 100 to 1000) increase in photochemical quantum yield in 2- propanol, in agreement with previous studies of 24DNP photochemistry. Therefore, 24DNP should be the most reactive nitrophenol among the primary and secondary atmospheric organic aerosol particles.

The undissociated nitrophenols generally had higher quantum yields than their deprotonated counterparts (as measured by comparing photochemistry in the presence of acid and base), with the exception of 4NP which had effectively the same quantum yield in acidic and basic solutions. In light of this, it is fair to say that the condensed-phase photochemical loss of 2NP, 4NP, and 246TNP is not highly dependent on the chemical environment: 2NP degrades minimally in either case, 4NP shows minimal change between water and 2-propanol, and 246TNP is always in the anion form in solution. The most drastic solvation difference is observed in 24DNP, resulting in a significant change to its absorption spectrum and reducing its ambient lifetime to just a few hours.

In summary, organic-phase photochemistry deviates the most from that in the aqueous phase for 24DNP, which appears to be a special case in the nitrophenol family. Analysis of the natural transition orbitals suggests that, at least for the lowest triplet state of 24DNP, the presence of alcohol solvent molecules results in more electron density on the $-NO_2$ groups, potentially accounting for its enhanced reactivity. It would be of interest to investigate these solvent effects

further, perhaps with more viscous solvent systems where the $-NO_2$ groups have less of an ability to reorganize after the excitation.

Chapter 3

Photochemical Degradation of 4-Nitrocatechol and 2,4-Dinitrophenol in a Sugar-Glass Secondary Organic Aerosol Surrogate

The roles that chemical environment and viscosity play in the photochemical fate of molecules trapped in atmospheric particles are poorly understood. The goal of this work was to characterize the photolysis of 4-nitrocatechol (4NC) and 2,4-dinitrophenol (24DNP) in semi-solid isomalt as a new type of surrogate for glassy organic aerosol, and compare it to photolysis in liquid water, isopropanol, and octanol. UV/Vis spectroscopy was used to monitor the absorbance decay to determine the rates of photochemical loss of 4NC and 24DNP. The quantum yield of 4NC photolysis was found to be smaller in an isomalt glass (2.6×10^{-6}) than in liquid isopropanol (1.1×10^{-5}). Both 4NC and 24DNP had much lower photolysis rates in water than in organic matrices suggesting that they would photolyze more efficiently in organic aerosol particles than in cloud or fog droplets. Liquid chromatography in tandem with mass spectrometry was used to examine photol-

ysis products of 4NC. In isopropanol solution, most products appeared to result from oxidation of 4NC, in stark contrast to photoreduction and dimerization products which were observed in solid isomalt. Therefore, the photochemical fate of 4NC, and presumably of other nitrophenols, should depend on whether they undergo photodegradation in a liquid or semi-solid organic particle.

3.1 Background

Secondary organic aerosol (SOA) is a complex mixture of different organic molecules, which can have a wide range of properties depending on formation mechanisms and environmental conditions. While SOA includes both gaseous and condensed-phase compounds, the term SOA is frequently used to refer only to the condensed phase, and we will follow the same convention in this paper. Models predict that the viscosity of SOA spans several orders of magnitude over a relatively small temperature range.[136] Both field measurements and laboratory studies have suggested that SOA exists as a viscous semi-solid or an amorphous glassy solid under low relative humidity and/or low temperature conditions, raising important questions about the effects of viscosity on atmospheric chemistry.[52,137–140] Viscosity has been shown to influence processes such as gas-particle partitioning, particle growth, the dynamics of coalescence of particles, and diffusion of molecules through SOA particles.[141–150] Since condensed-phase photochemical processes often include diffusion and secondary reactions of the photochemical reaction intermediates, the rate of photochemical processes in particles may also depend on viscosity. Though there have been recent studies investigating the effects of SOA viscosity on the photochemistry of select organic molecules, detailed characterization of photodegradation pathways of organic molecules in SOA has remained difficult due to the complex nature of the SOA material.[53,84]

The first goal of this work is to investigate the photochemistry of 4-nitrocatechol (4NC) under conditions representative of glassy SOA, to determine the rate of photochemical loss and propose products from photolysis. For comparison purposes, we also revisit the photochemistry of 2,4-dinitrophenol (24DNP) that was previously examined in water and in organic solvents.[53,84,116] 4NC is an important component in light-absorbing brown carbon.[7,12,34,35,67] Both primary and secondary biomass burning organic aerosol (BBOA) have been found to contain 4NC, with a strong winter-time correlation to levoglucosan.[151] Secondary sources are thought to be more prevalent in the summer, formed via reactions of lignin pyrolysis products with NO_2.[151] Field studies have shown that 4NC is especially prevalent in BBOA, mostly close to the com-

bustion source.[10,12,20,31,33,37,152] 24DNP is also commonly observed in ambient particles, alongside 4NC.[58] Laboratory studies have also shown that 4NC, 24DNP, and related nitrophenols and nitrocatechols represent an important component in SOA generated through oxidation of aromatic compounds by NO_3 radicals or by OH in the presence of NO_x.[38,153]

Previous studies of 4NC photochemistry focused on its behavior in gaseous phase and in aqueous solutions. Work by Zhao *et al.* (2015) looked at the pH dependence of 4NC aqueous phase photolysis by simulated sunlight and found the rate of photolysis to be quicker in a more acidic environment.[70] The photolysis rate was measured by quantifying the rate of photoenhancement at 420 nm. These experiments also looked at the effects of adding an OH scavenger, with results supporting the notion that photochemical loss of 4NC happens through photolysis. Hems & Abbatt investigated the aqueous photooxidation of 4NC and other nitrophenols by OH, produced by photolysis of hydrogen peroxide.[71] In presence of OH, an initial increase in light-absorption by the solution was observed, with bleaching occurring over longer periods of time. This eventual decrease in color was not observed by photolysis alone (i.e., without the source of OH). These results have been attributed to an initial functionalization of 4NC by addition of OH followed by ring-opening and fragmentation, with the latter leading to the decrease in visible absorbance. While these authors concluded that direct photolysis is slower than OH oxidation under aqueous conditions, this conclusion cannot be generalized to conditions found in a highly viscous organic particle, where OH reactivity is expected to be limited to the surface.[74]

Photolysis of 24DNP was previously examined, and found to be much slower in water (polychromatic quantum yield of 8.1×10^{-5}) compared to organic solvents (polychromatic quantum yield of 2×10^{-3} in octanol).[84,116] The photolysis rate of 24DNP was found to be suppressed by increasing the viscosity of the organic matrix.[84] In contrast to 24DNP, the viscosity effects on photochemistry of 4NC have not been examined yet, which represents an important gap in knowledge considering that the atmospheric abundance of 4NC is higher than that of 24DNP.

When 4NC (or 24DNP) is trapped in an SOA particle, we expect the photoexcited 4NC to react predominantly with neighboring organic compounds via hydrogen abstraction. These reactions of nitrophenols can be classified as "indirect photolysis" since secondary reactions of the excited states generate the final products. In this paper we use a more general term "photodegradation" to encompass both direct and indirect photochemical processes occurring in the system. The hypothesized mechanism is shown in Reactions 3.1-4, where 4NC* represents a triplet excited state of 4NC (the short-lived singlet excited state is omitted for simplicity).

$$4NC + h\nu \rightarrow 4NC^* \qquad \text{Reaction 3.1}$$

$$4NC^* \rightarrow 4NC + \text{heat} \qquad \text{Reaction 3.2}$$

$$4NC^* + R\text{-}H \rightarrow 4NC\text{-}H + R \qquad \text{Reaction 3.3}$$

$$4NC\text{-}H \rightarrow \text{photoproducts} \qquad \text{Reaction 3.4}$$

Matrix viscosity is expected to play a role in Reaction 3.3 by limiting the diffusion of 4NC* to a reaction partner, an organic molecule with easily-abstractable hydrogen atoms. Examples include aldehydic hydrogen atoms, or hydrogen atoms attached to alpha-carbon atoms in alcohols, which can be stabilized in the carbon-centered radical (CCR) from of the hydrogen atom donor. We also expect that the R radical produced in Reaction 3.3 will go on to react and form various biproducts, making SOA composition even more complex. The lifetime of 4NC* has not been reported in the literature, but the triplet state lifetimes in similar compounds like nitrophenols were observed to be less than one nanosecond.[125] On this short time scale, a highly viscous matrix could lead to a significant decrease in photoreactivity by hindering the ability of 4NC* to reorient itself for an optimal reaction with a suitable hydrogen atom donor. Viscosity could also play a role in the excited state dynamics leading to the formation of 4NC* by impacting the intersystem crossing efficiency from the excited singlet state to the triplet state.[154] Lignell *et al.* (2014) measured the effects of viscosity on the photochemistry of 24DNP, finding that a more viscous α-pinene SOA material led to stronger temperature and humidity dependence of the 24DNP photodegradation rate compared to less viscous octanol.[84] These were rather difficult experiments because of the

small amount of SOA material – it is challenging to produce more than a few hundred micrograms of SOA with common aerosol science approaches.

In view of the experimental challenges of working with SOA material, the second goal of this work is to provide a convenient way to overcome the difficulty of photochemical experiments in viscous organic matrices by using a proxy organic material that resembles the physical and chemical properties of SOA. For this, we seek a semi-solid or glass organic matrix in which we can easily deposit a photolabile organic molecule of interest. Previous studies have considered octanol, citric acid, and sucrose as suitable candidates for organic aerosol mimics.[51,53,155–157] The use of sucrose as an SOA surrogate was motivated by findings that reported presence of carbohydrate-like molecules in ambient particles.[158,159] This work shows that isomaltitol (the structure of this sugar alcohol is shown in Fig. 3.1) can be used as an SOA surrogate that is in many ways superior to sucrose. Isomaltitol, commonly referred to as just isomalt, is predominately used as a sugar substitute in candies, baked goods, and pharmaceuticals.[160] Like sucrose, the functionality of isomalt is limited to hydroxyl groups, which is only one of the many types of functional groups present in SOA (such as carboxylic acids or aldehydes). However, this compound is exceedingly easy to work with since it has relatively low glass transition and melting temperatures, 59°C and 142°C respectively,[161] and forms optically transparent glasses. Further, isomalt is thermally stable and does not decompose upon melting, unlike most other carbohydrates.[161] Isomalt is made up of an equimolar mixture of the diastereomers α-D-glucopyranosido-1,6-sorbitol and α-D-glucopyranosido-1,6-mannitol, a structure that has many abstractable hydrogen atoms resulting in stabilized CCR. These properties, combined with the expectation that isomalt will be photochemically inactive on its own, make isomalt a very convenient surrogate for experimental studies of photochemistry in glassy SOA.

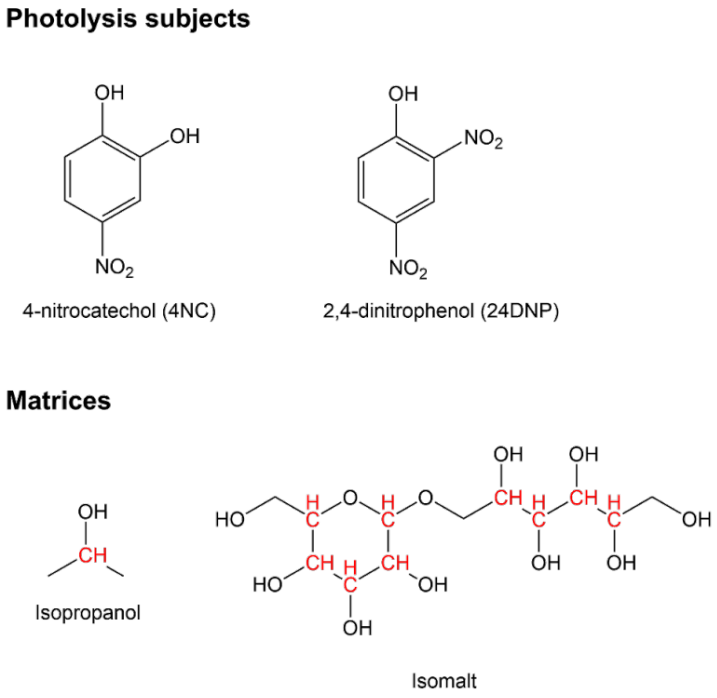

Figure 3.1: The chemicals used in this work. Photolysis was conducted on 4-nitrocatechol (4NC) and 2,4-dinitrophenol (24DNP). These molecules were photolyzed in four different solvents, namely water (not displayed), octanol (not displayed), isopropanol, and isomalt (also known as isomaltitol). The structures of the materials used for the solvents have red highlights indicating the locations of the most easily abstractable hydrogen atoms, due to the relative stability of the resulting carbon-centered radical products.

3.2 Methods

3.2.1 Glass Preparation

Isomalt glass was prepared by melting isomalt (food-grade, CK Products). In a beaker, $\sim$7 g of isomalt were heated slowly on a hot plate. Initial experiments included a thermometer to monitor the temperature, but this was cumbersome due to the stickiness of the isomalt. It appeared to melt around 115°C. These initial experiments proved that keeping the hot plate set to low-medium heat was sufficient to keep the isomalt from burning. With these settings, the isomalt powder melted within 3-4 min. Isomalt that was overheated ($>$120°C) for long periods of time, approximately 5 min, would begin to turn yellow, and would eventually begin turning brown/black if burned.

The mass of isomalt was measured each time so that a sample volume could be estimated using the density of the glass. A measurement of the isomalt density was done by melting 2.50 grams of isomalt in a graduated cylinder, producing a volume of 1.54 mL upon solidification, giving a density of 1.62 g/cm^3. This is similar to the density of sucrose (1.6 g/cm^3), so in all calculations a density of 1.6 g/cm^3 was used.

A 210 µL aliquot of a 40 mM 4NC aqueous solution was added to the molten isomalt and was then swirled until the yellow color of 4NC was evenly distributed. The resulting concentration of 4NC in the glass was approximately 2 mM (millimoles of isomalt per 1000 cm^3 of glass). The 2 mM concentration was chosen to produce an absorbance of the order of one (transmittance of 0.1) at near-UV wavelengths. Given that typical glasses had a thickness around 1 mm, we aimed at a 4NC concentration that was ten times greater than an analogous experiment in a 1 cm cuvette would require.

The glass could only be formed reliably if the amount of water added to isomalt was $<$ 500 µL. The formation of a glass seemed to be hindered by the addition of too much water, resulting in an isomalt slurry that failed to fully solidify. For example, the addition of 1-2 mL of water

created glasses that would harden but retained air bubbles and appeared cloudy. The use of highly concentrated aqueous stock solutions allowed for spike volumes less than 500 μL which was a good threshold for maintaining an optically transparent glass. The spike volumes of 100-500 μL added to 9 g of isomalt worked well for glass preparation purposes (in all kinetics experiments 210 μL of 40 mM stock solution was used for consistency).

We also tried to add solid 4NC to isomalt before melting, thus eliminating water altogether, but this method was inferior compared to adding a solution of 4NC to molten isomalt as described above. When 4NC was added directly as a dry powder a low-viscosity yellow oil would form and would fail to homogeneously mix with the isomalt. There were minimal apparent issues with this kind of phase separation with adequately small additions of the stock solutions.

A drop of the molten isomalt/4NC mixture was poured onto a round fused silica window (Edmund Optics, 25 mm diameter, 2.3 mm thickness) and then immediately covered with a second window. The second window was held on the edges and pressed firmly by hand onto the molten glass, resulting in the glass cooling rapidly and solidifying. When being pressed, the isomalt glass would often form small fractures. To alleviate this issue, the sandwiched samples were heated directly on a hot plate until the fractures had fused together. This heating step also served to even out the thickness of the isomalt/4NC glass sample. The reheating was done for as short of a time as possible, less than a minute, to avoid overheating the isomalt. If left on the heat source for too long, the sample would begin to bubble between the windows and also pour off the sides. A reference for the UV/Vis was prepared by pouring pure molten isomalt without added 4NC onto a window and following the same procedure.

The same procedure outlined above was used to prepare 24DNP/isomalt samples, using a 350 μL aliquot of a 15 mM 24DNP (99.4%, Sigma Aldrich) aqueous solution to add to the molten isomalt.

3.2.2 Safety Considerations

Preparation of isomalt glass requires the handling of hot glassware, the pouring of molten isomalt, and dealing with sharp isomalt glass. Heat-resistant gloves should be worn when handling glassware containing molten isomalt. Care should be taken when pouring or mixing the molten isomalt, as contact with the skin can cause severe burns. Rapid cooling of isomalt can result in the formation of sharp edges and needle-like pieces. For this reason, avoid washing glassware containing isomalt glass by hand. We have found it simple to dispose of isomalt samples by carefully transferring the molten glass to a suitable heat-proof waste container.

3.2.3 Photochemistry Setup

Experiments in the solid state were carried out using a custom apparatus (Fig. 3.2). The decay of 4NC in an UV-irradiated isomalt/4NC glass was monitored from the change in the UV/Vis absorption spectrum, recorded using an Ocean Optics DH-2000-DUV light source (the source has both D_2 and W lamps but only D_2 lamp was used), optical fibers and an Ocean Optics USB4000 spectrometer. Ocean Optics SpectraSuite was used to operate the spectrometer in "scope" mode. Measured intensities were averaged from 5 scans and the integration time was set in the range of 40-90 ms, depending on the thickness of the sample. Exported data was then averaged with a $\sim$1 nm boxcar filter using MATLAB.

Photolysis was also conducted in octanol in order to validate previously reported results for 24DNP.[84] These samples were prepared by dispensing a 10 µL drop of either 20 mM 4NC or 24 mM 24DNP in octanol onto a SiO_2 window and gently laying another window on top. The resulting film between the windows had an estimated thickness of 25 µm. The solid state UV/Vis setup was used to analyze these samples.

Photolysis experiments in bulk solutions were carried out to compare to solid-state photolysis. These experiments were done directly inside a Shimadzu UV-2450 UV/Vis spectrophotometer operated with Shimadzu UV Probe 2.34 software. 4NC was dissolved in water or isopropanol to get a concentration of 40 μM. The solution was placed in a standard 10 mm cuvette and remained inside the spectrophotometer for the duration of the experiment while being irradiated from above. A pure solvent was used as a reference.

For both solid-state and liquid phase experiments, photolysis was done by irradiating each sample with light from a 150 W Xe arc lamp (Newport 66902 lamp housing). The radiation reaching the sample was filtered by reflecting the output of the Xe lamp off a 280-400 nm dichroic mirror and directing it through a Schott WG295 long-pass filter and a Schott BG1 UV band-pass filter. The remaining radiation in the 290-450 nm range was directed through a liquid light guide (Edmunds #53-691) onto the solid sample at a 15 degree angle (Fig. 3.2). The use of the liquid light guide reduced the filtered lamp power by 75% but permitted easy switching between solid and liquid state setups. The photon flux density of the light exiting the light guide and reaching the sample can be found in Figure 3.3.

3.2.4 Product Analysis

Following photolysis, the sandwiched windows were placed in a beaker with around 15 mL of deionized water to cover the top of the stack. The windows were kept in the water for up to a couple of hours to allow the isomalt to fully dissolve. The resulting solution was light-yellow in color. Once the windows were removed, the sample solutions were placed in a rotary evaporator and the volume was reduced to about 1 mL. Samples were then transferred into 300 μL glass vials. Product analysis was conducted with a Thermo Scientific Vanquish Horizon ultra performance liquid chromatograph (UPLC) in line with a Vanquish Horizon photodiode array (PDA) spectrometer and a Q Exactive Plus high resolution mass spectrometer (HRMS). A heated

electrospray ionization (HESI) source was used to generate ions for HRMS and was used solely in negative ion mode. The HESI capillary temperature was set to 300°C and a spray voltage of 2.5 kV. The scan range was 50-750 m/z units. The PDA was set to measure absorbance between 190-682 nm.

HRMS data was processed using the Thermo Scientific software Freestyle 1.6. For each run, a sample was collected and analyzed before and after photolysis, allowing for detection of photolysis products. Each photolysis sample analyzed in the UPLC/HRMS had a "photolysis blank" which was the remaining 4NC/glass mixture after sample preparation. Virtually no other peaks were observed other than 4NC in these non-photolyzed glass samples, suggesting thermal degradation was not a major issue. Molecular formula assignments by Freestyle were confirmed with the MIDAS Formula Calculator version 1.2.3 and were within 2 ppm mass tolerance. Since Freestyle places no restrictions on the number of C, H, N, or O atoms, the advantage of the Formula Calculator was that it helped enforce the correct valence rules and avoid unphysical formulas. All other elements were excluded from formula assignments since neither 4NC nor its solvent contained them.

3.3 Results and Discussion

3.3.1 Molar Extinction Coefficient Measurements

The molar absorptivity of 4NC has been reported in aqueous solution at various pH values.[162] Though the absorption spectrum of 4NC in solid isomalt had a similar shape to the spectrum in an acidic aqueous solution, experiments were conducted to determine the molar absorptivity, ε, of 4NC in isomalt. Previous studies with nitrophenols observed broadening and red shifting of nitrophenols absorption bands when bound (adsorbed) to aerosol particles.[50] Since the path length of the sample could be easily measured using digital calipers, the absorbance of 4NC in

isomalt of a fixed concentration was measured at various sample thicknesses (b). Equation 2.1 was used to determine ε from measured absorbance, $A(b)$, for a fixed concentration C = 2.07 mM (Fig. 3.4).

$$A(b) = \varepsilon\, b\, C \tag{3.1}$$

The molar absorptivity at the peak of the 350 nm absorption band was found to be (7.5 $\pm$ 0.6) $\times$ 10^3 M^{-1} cm^{-1}, which is comparable to the previous reported value of 6800 M^{-1} cm^{-1} at 347 nm for 4NC in a pH = 2.0 aqueous solution.[162] A comparison to an acidified solution is relevant since the acid suppresses ionization of 4NC anion, which has a different absorption spectrum.

The wavelength-dependent molar extinction coefficients are shown in Figure 3.4. These spectra were produced by dividing the measured absorbance spectra by the concentration and path length of their respective samples. For 4NC in isomalt, the molar extinction coefficients were calculated from an average of five samples of varying thicknesses. Shading represents a 95% confidence interval from these samples. The low values for 4NC in isomalt below 250 nm are likely due to instrumental limitations in UV transmission in the solid UV/Vis setup. The molar extinction spectrum shown for 4NC in isopropanol was produced from an absorption spectrum of a 172 μM solution. We note that absorption spectra of 4NC in isopropanol at much lower concentrations had a visible secondary peak at 430 nm as a result of partial ionization of 4NC (for example, Fig. 3.9). The shape of the absorption spectra are similar but the spectrum in isomalt displays a bathochromic shift of the order of 5 nm from 345 nm in liquid isopropanol to 350 nm in solid isomalt.

3.3.2 Photochemical Kinetics

The rate of photochemical loss of 4NC and 24DNP was monitored by following the decay in absorbance of the glass or solution. An example of the absorption spectra recorded throughout photolysis of 4NC in isomalt is presented in Fig. 3.5, and spectra of 4NC during photolysis in isopropanol are shown in Fig. 3.9. Figure 3.5b shows the same spectra in Fig. 3.5a normalized to the initial absorbance at $t = 0$, and the decay of this normalized absorbance at 370 nm shown in Fig. 3.5c. Results from 4NC in octanol are provided at the end of this chapter in the same manner in Fig. 3.13, and results from 24DNP in octanol and isomalt are provided in Fig. 3.10 and Fig. 3.11.

3.3.3 Photochemical Quantum Yields

For optically thin samples, the first-order photolysis rate constant k can be related to the photolyzing radiation parameters as follows:

$$k = \int \phi(\lambda)\sigma(\lambda)F(\lambda)d\lambda \tag{3.2}$$

The normalized absorbance can be modeled by Equation 3.3.

$$A(t)/A(t=0) = C + (1-C)\exp(-kt) \tag{3.3}$$

which assumes that 4NC has a first-order decay forming a single product with a different absorption spectrum and no secondary photochemistry. The presence of the isosbestic point (near 340 nm in isomalt) in the data supports the assumption that only one product contributed to absorption in addition to 4NC (but does not exclude formation of additional weakly-absorbing products). The fitting parameter C represents the ratio of the molar extinction coefficient of the photolysis product to that of 4NC at the monitored wavelength and k is the first-order rate constant. Ideally, C should be zero at the observation wavelength but it is not achievable in practice. The wave-

lengths used for fitting the decay in the normalized absorbance were selected at point within the 4NC absorption peak that had the greatest decrease from the initial absorbance, where C should have the smallest value. The chosen wavelengths varied between different matrices, with the largest decreases in absorbance occurring around 350 nm in isopropanol (Fig. 3.9) and octanol (Fig. 3.10) and around 370 nm in isomalt (Fig. 3.5b). For 24DNP (Fig. 3.11 & Fig. 3.12), the largest change was at 290 nm in octanol and 260 nm in isomalt.

On the timescale used in these experiments (3 to 5 h), we observed significant loss of 24DNP absorbance but absorbance of 4NC reduced by less than 30% (Fig. 3.5). Due to this, there was increased correlation between k and C, resulting in large uncertainties for k measured for 4NC. Experiments were not conducted at longer timescales to avoid any secondary photochemistry of primary photolysis products. For short time scales, Equation 3.3 simplifies to Equation 3.4.

$$A(t)/A(t=0) = 1 - k(1-C)t \tag{3.4}$$

While the linear fit is more robust, it does not make it possible to determine k and C independently, and as such we report the product $k(1-C)$ in Table 3.1. The rate constants k from the exponential fit and $k(1-C)$ from the linear fit listed in Table 3.1 were similar in magnitude, hinting that C at the selected wavelengths was relatively small. In cases where C could be reliably obtained from the fit, the average fitted value of C at 350 nm obtained from three trials of 4NC in isomalt was 0.014, whereas the fits in octanol and isopropanol yielded values of C around 10^{-6}. Therefore, in all cases, quantum yields were calculated from the more precise linear fit rate constants, assuming $C \approx 0$.

The incident photons are represented by the spectral flux, $F(\lambda)$, shown in Fig. 3.3, and the wavelength-dependent molecular absorption cross section is $\sigma(\lambda)$. Since photolysis was done with a broadband light source, represented by the spectral flux density $F(\lambda)$, it is impossible to extract the wavelength dependence of the quantum yield from these data. An effective (polychro-

matic) quantum yield, $\langle\phi\rangle$ was determined by factoring it from the integral and integrating the remaining over a small wavelength range. In this work, the interval of integration was limited to 300-400 nm for 4NC, approximately 50 nm on either side of the main 350 nm peak in absorbance. Using the same logic for 24DNP, the interval 240-340 nm was used in octanol and isomalt. These intervals were used to encompass the main absorption bands of these molecules. Under this assumption, the effective quantum yield averaged over the wavelength integration range can be determined by the following equation.

$$\langle\phi\rangle = \frac{k}{\int_{\lambda_1}^{\lambda_2} F(\lambda)\sigma(\lambda)\, d\lambda} \tag{3.5}$$

The polychromatic quantum yields are listed in Table 3.1. Results from triplicate experiments of 4NC photolysis in isomalt are shown in Table 3.2. The isomalt matrix appears to have good reproducibility in the photolysis experiments, which is an important factor for using as a surrogate for SOA photochemical studies.

Table 3.1: Rate constants and quantum yields from photolysis of 4NC and 24DNP in various matrices

Molecule	**Matrix**	k **[s^{-1}] / 10^{-5}**	$k(1-C)$ **[s^{-1}] / 10^{-5}**	$\langle\phi\rangle$ **/ 10^{-5}**	**Lifetime**[a]
4NC	isomalt (solid)	5 ± 3	1.8 ± 0.1	0.26 ± 0.02	24 days
	octanol (film)	3.2 ± 0.2	2.7 ± 0.1	0.40 ± 0.01	16 days
	isopropanol (sol'n)	5.4 ± 0.3	4.1 ± 0.2	1.07 ± 0.07	5.8 days
	water (sol'n)	0.09 ± 0.02	0.11 ± 0.03	0.013 ± 0.003	1 year
24DNP	isomalt (solid)	2.9 ± 0.7		36 ± 8	4 h
	octanol (film)	44 ± 3		180 ± 10	1.2 h
		20.4(1)[b]		200[b]	
	SOM[c] (film)	47.3(8)[b]		not reported[b]	
	water (sol'n)	-		0.4	
				8.1 ± 0.4[c]	

[a]Estimated atmospheric lifetime. [b]Referenced from Lignell *et al.* with a different lamp power.[84] [c]Secondary organic material. [c] Referenced from Albinet *et al.*[116] Errors in this work represent the error from the fitted equation.

Table 3.2: Rate constants and quantum yields from triplicate experiments with 4-nitrocatechol in isomalt glass

Experiment #	k **[s^{-1}] / 10^{-5}**	$k(1-C)$**[s^{-1}] / 10^{-5}**	$\langle\phi\rangle$ **/ 10^{-5}**
Trial 1	1 ± 7	1.5 ± 0.1	-[b]
Trial 2	1 ± 4	1.2 ± 0.1	2 ± 8
Trial 3	5 ± 3	1.4 ± 0.2	8 ± 5

[a]Polychromatic quantum yield calculated from k values. [b]Quantum yield could not be calculated due to large uncertainty in Trial #1.

3.3.4 Matrix effects on the 4NC and 24DNP photodegradation

Table 3.1 shows that rate constants varied depending on the local environment. For photolysis of 4NC, the reaction was the slowest in an aqueous environment $\langle\phi\rangle = 1.3 \times 10^{-7}$ and proceeded faster in solid isomalt (2.6×10^{-6}) and even faster in liquid octanol (4×10^{-6}) and isopropanol (1.1×10^{-5}). With the drastic difference between organic matrices and water, it is possible that while also being less reactive, water is more effective at quenching excited 4NC* (Reaction 2). Although the photochemical degradation in the organic solvents was slower in the isomalt glass than in liquid alcohols, it was still significantly quicker than in water. Despite the glassy nature of isomalt, photochemistry was not fully suppressed inside the isomalt matrix.

To put these results in perspective, we compare the measured quantum yields to a previous study by Lignell et. al (2014), who conducted experiments with 24DNP in both octanol and α-pinene secondary organic material (SOM).[84] Within experimental uncertainties, we obtained the same polychromatic quantum yield in octanol (1.8×10^{-3}) as Lignell *et al.* (2×10^{-3}). Our quantum yield of 24DNP in isomalt (3.6×10^{-4}) was lower than that in octanol. Although quantum yields were not reported for 24DNP in SOM by Lignell *et al.*, their photolysis rate in SOM was twice of the rate in octanol. Since our observed quantum yields in isomalt and octanol followed the opposite trend, we predict that the glassy isomalt matrix is less reactive than α-pinene SOM in terms of reactivity with the triplet state of 24DNP.

Using the experimentally determined quantum yields, we estimated photochemical lifetimes of 4NC and 24DNP in the Los Angeles atmosphere from the reciprocal of the calculated rate constants from Equation 2.2. The 24-hour average spectral flux density, $F(\lambda)$, for Los Angeles, California (34° N, 118° W) on 20 June 2017 was simulated using the National Center for Atmospheric Research (NCAR) Tropospheric Ultraviolet and Visible (TUV) calculator. The photolysis lifetimes for 4NC in octanol and isomalt were found to be 16 and 24 days, respectively. These fall within the range of the lifetimes of the overall brown carbon (BrC) absorption coefficient of BBOA, reported as 10-41 days by Fleming *et al.* (2020).[34] However, in their work, they found the photochemical lifetime of 4NC in chamise fire BBOA to be $\sim$12 hours, which they regarded as a lower limit. The slower photolysis of 4NC in octanol and isomalt glass suggest that organic molecules found in BBOA are even more efficient in reacting with triplet state 4NC than alcohols are.

The lifetimes of 4NC with respect to OH oxidation have been evaluated by Hems & Abbatt.[71] In the aqueous phase the lifetime was measured to be 4.7 h, assuming [OH] = 1×10^{-14} M, and in the gaseous phase it was estimated to be 88 h (3.7 days), assuming [OH] = 1×10^{6} cm^{-3}. With the slow photolysis rate of 4NC in water, photolysis is not competitive with OH oxidation in the aqueous phase. However, photolysis in the organic phase occurs at a more comparable rate to gaseous OH oxidation. Therefore, the loss of 4NC could be controlled by photolysis when it is trapped in a highly viscous organic particle. The photolysis lifetimes for 24DNP are considerably shorter, 1.2 hours in octanol and 4 hours in isomalt under Los Angeles summer conditions. Considering that 24DNP is less volatile than 4NC, and therefore more likely to partition in particles, the photolysis of 24DNP in organic particles should be an important, and possibly the dominant loss mechanism for this molecule.

3.3.5 Photoproduct Analysis

Total ion current (TIC) chromatograms produced from samples from before and after photolysis in both the isopropanol and the isomalt samples are shown in Figure 3.6. Figures 3.13 and 3.14 (at the end of the chapter) show select PDA absorption spectra of the products for photolysis in isopropanol and isomalt, respectively.

A summary of the observed photoproducts suggested by UPLC-PDA-HRMS analysis of 4NC photolysis samples is presented in Figure 3.7. We have observed different sets of products in the liquid and solid matrices. In solution, the primary photoproducts observed appear to correspond to an addition of -OH to 4NC ($C_6H_5O_4N \rightarrow C_6H_5O_5N$). It is important to note that experiments in isopropanol were open to the air, making it impossible to definitively tell if the -OH addition was from the isopropanol solvent. Exposure to oxygen could have influenced formation of these oxidation products, through singlet oxygen formation or HO_x generated by the 4NC-H.[163,164] 4NC has three distinct hydrogen atoms in the aromatic ring but both isopropanol/aqueous and isomalt/aqueous solutions had only two peaks for $C_6H_5O_5N$, suggesting two of three possible isomers are formed from this reaction. Due to a lack of analytical standards of these compounds, the preferred isomers could not be confirmed. The UV/Vis absorption spectra corresponding to these $C_6H_5O_5N$ products are shown in Figure 3.4. The earlier eluted peak for this mass has a peak absorbance at 345 nm, while the spectrum of the later peak shows two maxima, one at 325 nm and one at 400 nm. It is possible that all three isomers of the -OH addition to 4NC are being formed but is impossible to confirm with a lack of published absorption spectra for two of the three isomers.

In contrast to experiments in solution, 4NC embedded in isomalt appears to have formed some dimers of 4NC. Although the melted isomalt/4NC mixture appeared as one phase, it is possible that 4NC were forming complexes together in the matrix promoted by π-π stacking interactions (this would be consistent with the observed small bathochromic shift in isomalt, Fig.

3.4). The proximity between two 4NC molecules would promote 4NC*+4NC reaction instead of 4NC*+isomalt reaction, as the H atoms on the hydroxyl groups in catechols are also easily abstractable. Signal for 4NC dimers in the non-photolyzed candy was very low, so it is unlikely that heating caused excessive dimerization. It has been reported that inside of a viscous organic particle, diffusion of oxygen into the particle is minimal, giving rise to persistent radicals and allowing for radical recombination between neighboring 4NC-H.[155]

The isomalt matrix appears to have also yielded the oxygen loss product ($C_6H_5O_4N \rightarrow C_6H_5O_3N$), which could be the replacement of -OH with -H or the loss of an -O from the -NO_2 group. The PDA UV/Vis spectrum had a pronounced peak at 322 nm shown in Fig. 3.14). A peak at this absorbance is not characteristic 2-nitrophenol in aqueous solution.[51,83] A study of aqueous 4-nitrophenol photolysis showed an absorbance maximum at 325 nm, which is relatively close.[83,113] However, we only observed a single isomer of $C_6H_5O_3N$ in single ion chromatograms, which is an argument against assigning this product to 4-nitrophenol. Absorption spectra of 4-nitrosocatechol could not be found in the literature. The absorption spectrum for 4-nitrosophenol has been reported with a maximum around 300 nm.[165] If the additional OH group causes the same red-shift in absorption between 4-nitrosophenol and 4-nitrosocatechol as it shows between phenol and catechol, it is likely that 4-nitrosocatechol is being observed.[166,167] Furthermore, the fragmentation spectrum of the ion corresponding to $C_6H_5O_3N$ (Fig. 3.8) contained a peak corresponding to the loss of NO, but no peak corresponding to the loss of -NO_2. Therefore, we assigned the photoproduct observed here to 4-nitrosocatechol, as indicated in Figure 3.8. Nitroso compounds are highly reactive, so 4-nitrosocatechol is likely to proceed to secondary products, but may have stuck around due to being restricted in the glassy matrix.

24DNP was also observed as a product unique to photolysis of 4NC in isomalt ($C_6H_5O_4N \rightarrow C_6H_4O_5N_2$). A single peak was eluted for $C_6H_4O_5N_2$ with a corresponding PDA UV/Vis spectrum that peaks at 260 and 290 nm (Fig 3.14g). This product is somewhat unexpected, as it would require a direct swap of -OH for -NO_2. If this replacement happened in two steps, we would expect to

also observe products corresponding to loss of -OH. As previously discussed, loss of -OH was not evident. Further, for 24DNP to be the product the -OH loss intermediate would have needed to be 2-nitrophenol, which was ruled out based on the UV/Vis spectrum. If 24DNP is being formed as a product of 4NC photolysis, it seems most likely that it is occurring in a direct 4NC*+4NC reaction.

Finally, the chromatogram contained peaks that could not reasonably come from 4NC, for example, peaks corresponding to neutral formulas $C_6H_{10}O_4$, $C_8H_{14}O_4$, $C_9H_{16}O_4$, and $C_{12}H_{14}O_4$. Hydrolysis of isomalt would yield glucose, mannitol, and sorbitol (all $C_6H_{12}O_6$), which none of the observed formulas correspond to. Dehydration of the glucose, mannitol, or sorbitol components of isomalt does not explain observation of $C_6H_{10}O_4$. The $C_6H_{12}O_6 \rightarrow C_6H_{10}O_4$ transformation would require loss of H_2O_2. This implies that the photoreduction of 4NC could lead to peroxide formation in the isomalt matrix, similar to how irradiation of nitro-polycyclic aromatic hydrocarbons has been shown to lead to peroxide formation in methyl lineolate.[168] Oxygen could have potentially entered the matrix as air bubbles during sample preparation. Although oxygen is expected to be depleted quickly by free radicals, a small portion would have been available for reaction.[169] The mechanistic details of this process will be explored in future studies.

3.4 Implications

This work uses isomalt as a proxy for a glassy SOA matrix. The use of isomalt provides a simple preparation of a photolysis medium that, by itself, is optically transparent and photochemically stable. Our experiments on photochemistry of 4NC and 24DNP show that candy-like isomalt is a convenient matrix for reproducible photochemical experiments and product analysis. This simple method opens new avenues for atmospheric condensed-phase photochemical experiments, not only on nitrophenols, but on other photochemically active organic compounds.

We observe that photodegradation rates of 4NC and 24DNP in solid isomalt are comparable to those in liquid octanol and isopropanol. This is an important result demonstrating that photochemistry of nitrophenols can occur even when they are trapped in a highly viscous organic particles. The estimated photochemical lifetimes of 4NC in the organic phase are comparable to those of OH oxidation in the gas phase. For 24DNP, the major loss mechanism will be dependent on the viscosity of the organic particle it is trapped in.

The different types of products for 4NC photolysis in isopropanol and isomalt represent another important result of this work. In isopropanol, only products corresponding to the addition of -OH groups are observed. In contrast, photolysis in isomalt glass results in 4NC dimerization, and formation of products corresponding to an addition of -NO_2, or loss of -OH from 4NC. There is evidence of photoreduction of 4NC, which is an uncommon process for the highly oxidizing atmospheric environment, and produces highly-reactive nitroso compounds. Varying photoproducts between the solid and liquid environment have implications for understanding the environmental fates of nitrophenols, with products being dependent on the specific environment nitrophenols are exposed to during their atmospheric transport.

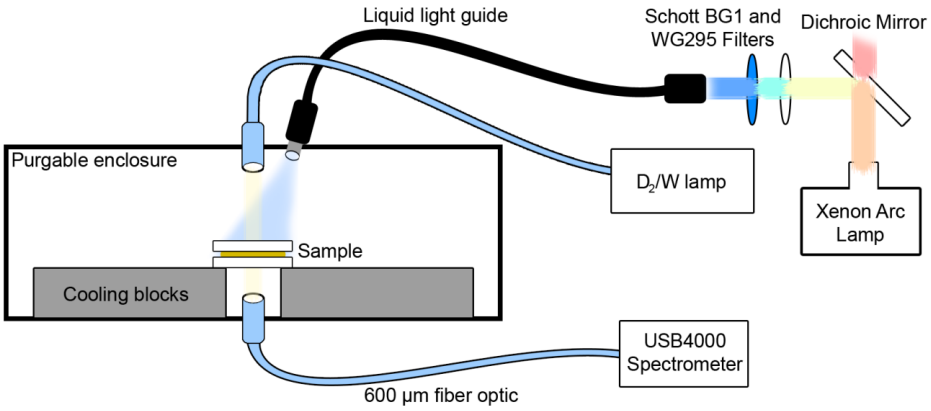

Figure 3.2: Apparatus used for solid state photolysis. The broadband probe radiation coming from the D_2/W source had a significantly smaller power output than the Xenon lamp used for photolysis and did not contribute to photolysis.

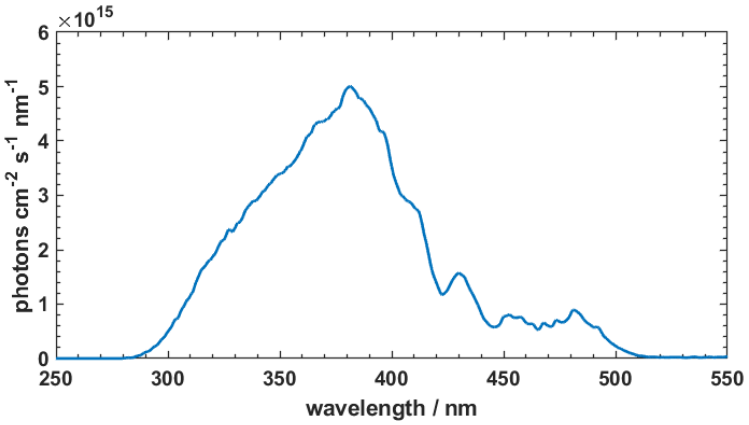

Figure 3.3: Photon flux density $F(\lambda)$ (photons cm^{-2} s^{-1} nm^{-1}) of the filtered Xenon arc lamp used for photolysis. Spectrum was calculated from the spectral irradiance measured with a StellarNet BLACK-Comet spectrometer. The measurement was taken after the light guide, with the same setup used for photolysis.

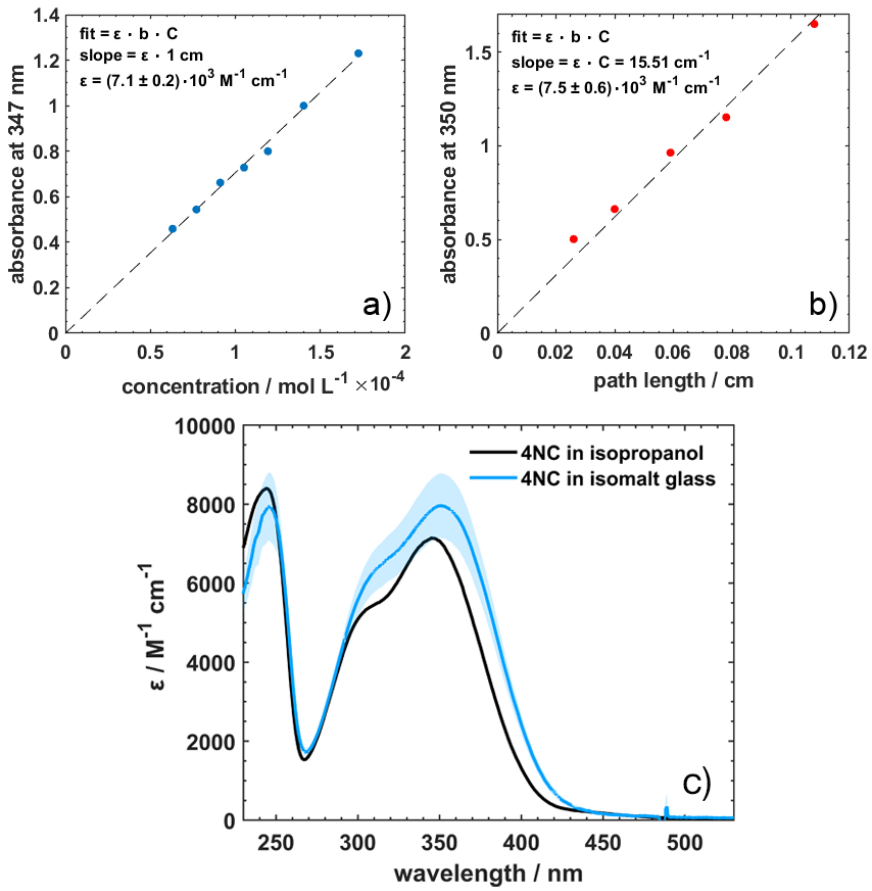

Figure 3.4: Beer's law plots for 4NC in (a) isopropanol solution and (b) isomalt glass at the peak of the absorption spectrum (347 nm for 4NC in isopropanol and 350 nm for 4NC in solid isomalt). The concentration was fixed in the isomalt experiments at 2.07 mM and each data point corresponds to a new preparation of glass. The intercept for both fits was fixed to the origin. (c) Molar extinction coefficient as a function of wavelength for 4-nitrocatechol in (black) isopropanol and (blue) isomalt glass. Shading around the isomalt trace represents a 95% confidence interval from five measurements.

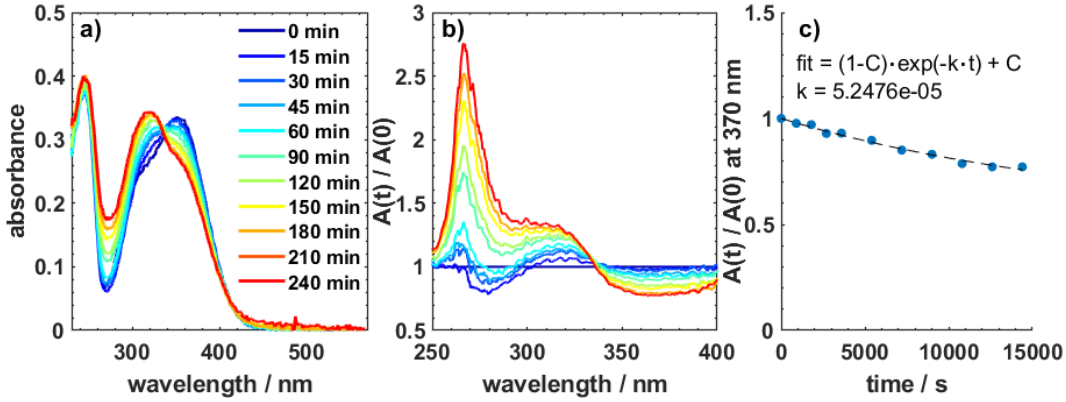

Figure 3.5: Plot of the absorption spectra of 4NC in isomalt glass obtained at different times during photolysis (a), the same absorbance spectra normalized to the absorbance at t = 0 (b), and the decay in normalized absorbance at 370 nm (c). Notable features of this dataset are the growth of absorbance at wavelengths below 340 nm and above 400 nm, as well as the decay around the 350 nm band of 4NC.

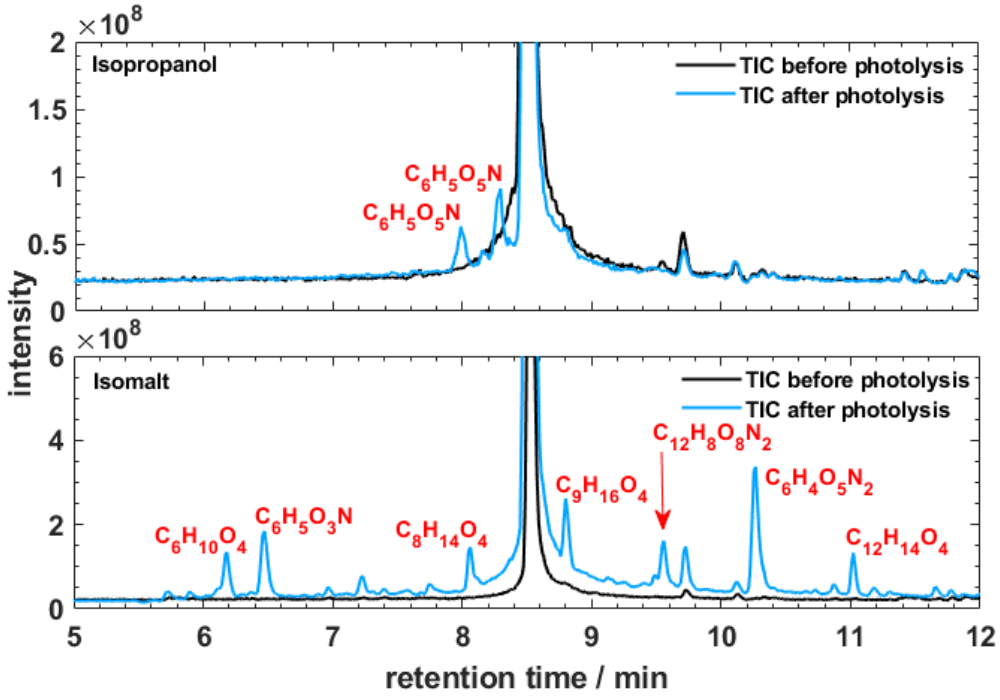

Figure 3.6: Total ion current chromatograms from UPLC-HRMS analysis 4-nitrocatechol/isomalt glass samples before and after photolysis. Molecular formula assignments are provisional and represent the molecular species eluted at that peak retention time.

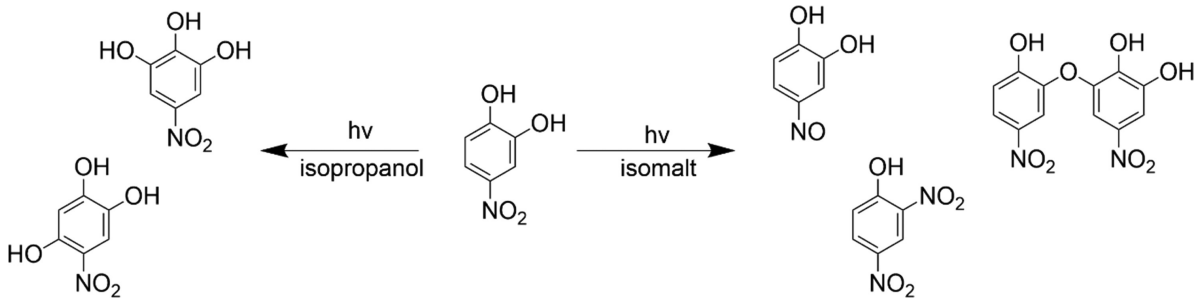

Figure 3.7: Products formed during photolysis of 4-nitrocatechol in an isopropanol solution (left) and an amorphous isomalt glass (right). The structural assignments presented should be considered provisional.

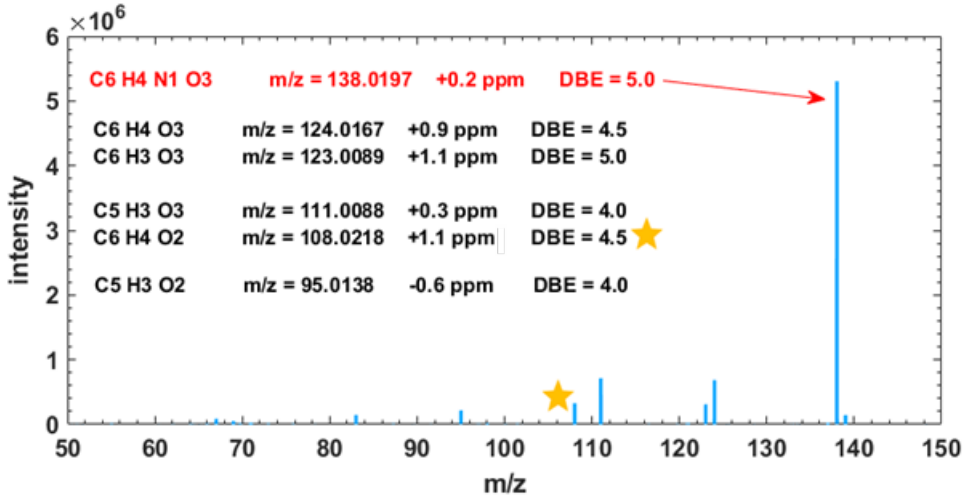

Figure 3.8: MS/MS spectrum for m/z = 138.02 with outputs from the molecular calculator overlayed for the major peaks in the mass spectrum. The parent ion corresponds to $C_6H_4O_3N^-$, which could be either nitrophenol or 4-nitrosocatechol. The peak labeled with a gold star corresponds to loss of -NO from the parent, suggesting the 4-nitrosocatechol structure. A peak corresponding to the loss of -NO_2 would be at m/z = 92, but it was not observed. More complex fragmentation processes are also taking place corresponding to the loss of N, NH, HCN, and HCNO.

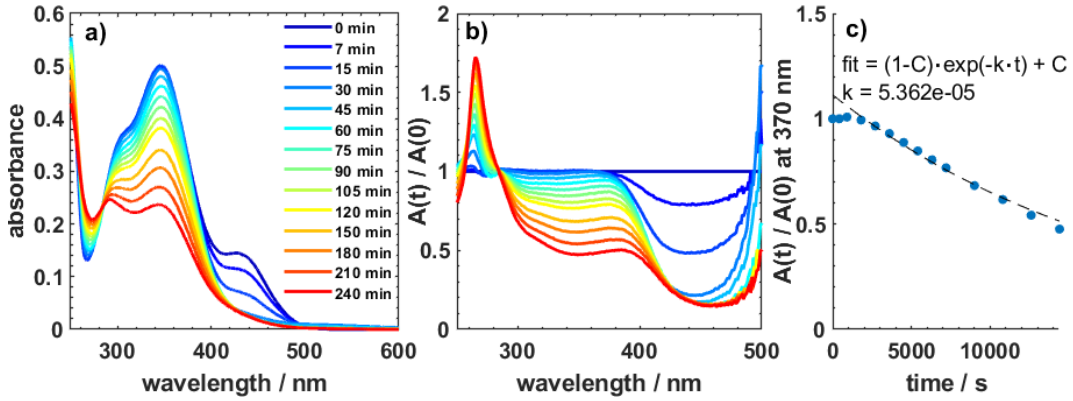

Figure 3.9: Absorption spectra recorded during photolysis of a 40 mM solution of 4NC in isopropanol (a), absorption spectra from (a) normalized to the absorbance at t=0 (b), and the decay in normalized absorbance at 370 nm with an exponential fit (c). The fit in (c) was done relative to the 30 min mark when the absorbance first started to decrease. We note that in this example 4NC solution in isopropanol is not acidified, and some ionization of 4NC occurs producing the 4NC anion band at 420 nm. The anion's band disappears faster, and we start our fit in (c) after this band is gone. We have not explored the effect of acid-base equilibrium on photolysis in this work as the focus was on photolysis in isomalt, where such anion formation did not occur.

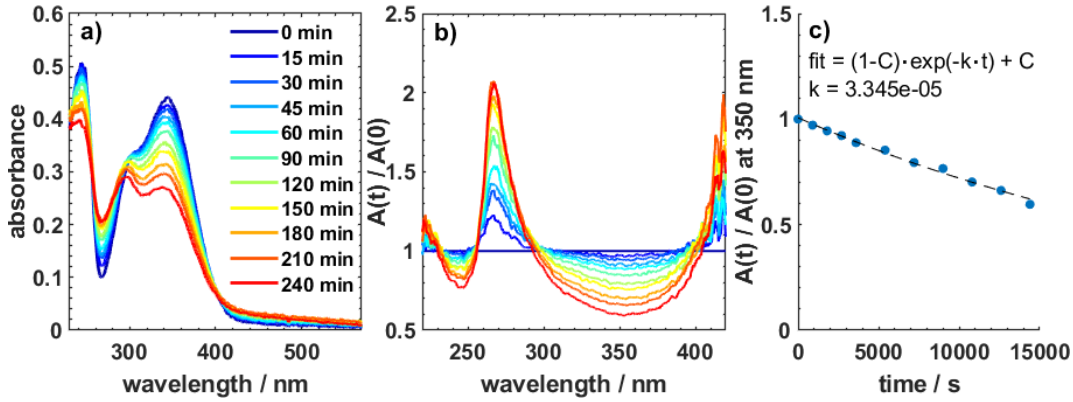

Figure 3.10: Plot of the absorption spectra of 21 mM 4NC in an octanol film obtained at different times during photolysis (a), the same absorbance spectra normalized to the absorbance at t = 0 (b), and the decay in normalized absorbance at 350 nm (c). Strong growth in absorbance was observed between 250-300 nm, as well as above 400 nm. Low absorbance values at 400+ nm cause noise in the normalized absorbance (an artifact of normalization that can be disregarded).

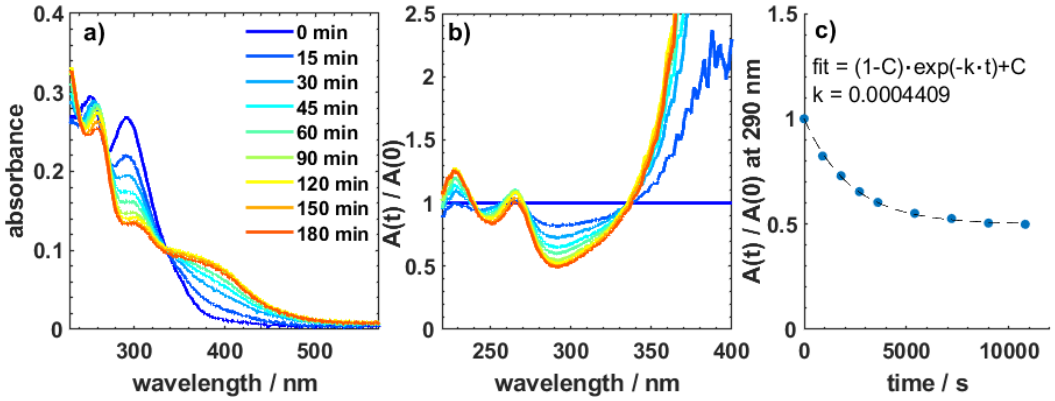

Figure 3.11: Plot of the absorption spectra of 24 mM 24DNP in an octanol film obtained at different times during photolysis (a), the same absorbance spectra normalized to the absorbance at t = 0 (b), and the decay in normalized absorbance at 290 nm (c).

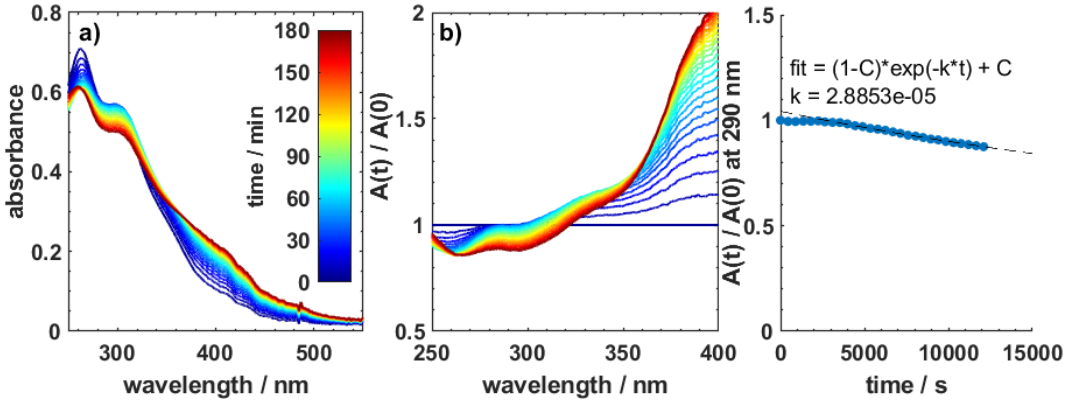

Figure 3.12: Plot of the absorption spectra of 24DNP in isomalt glass obtained at different times during photolysis (a), the same absorbance spectra normalized to the absorbance at t = 0 (b), and the decay in normalized absorbance at 290 nm (c). Measurements were taken every 7.5 minutes due to expectations of quick reactivity based on findings in octanol. The fit in (c) was applied only after 30 minutes into photolysis due to a lack of decay during that time.

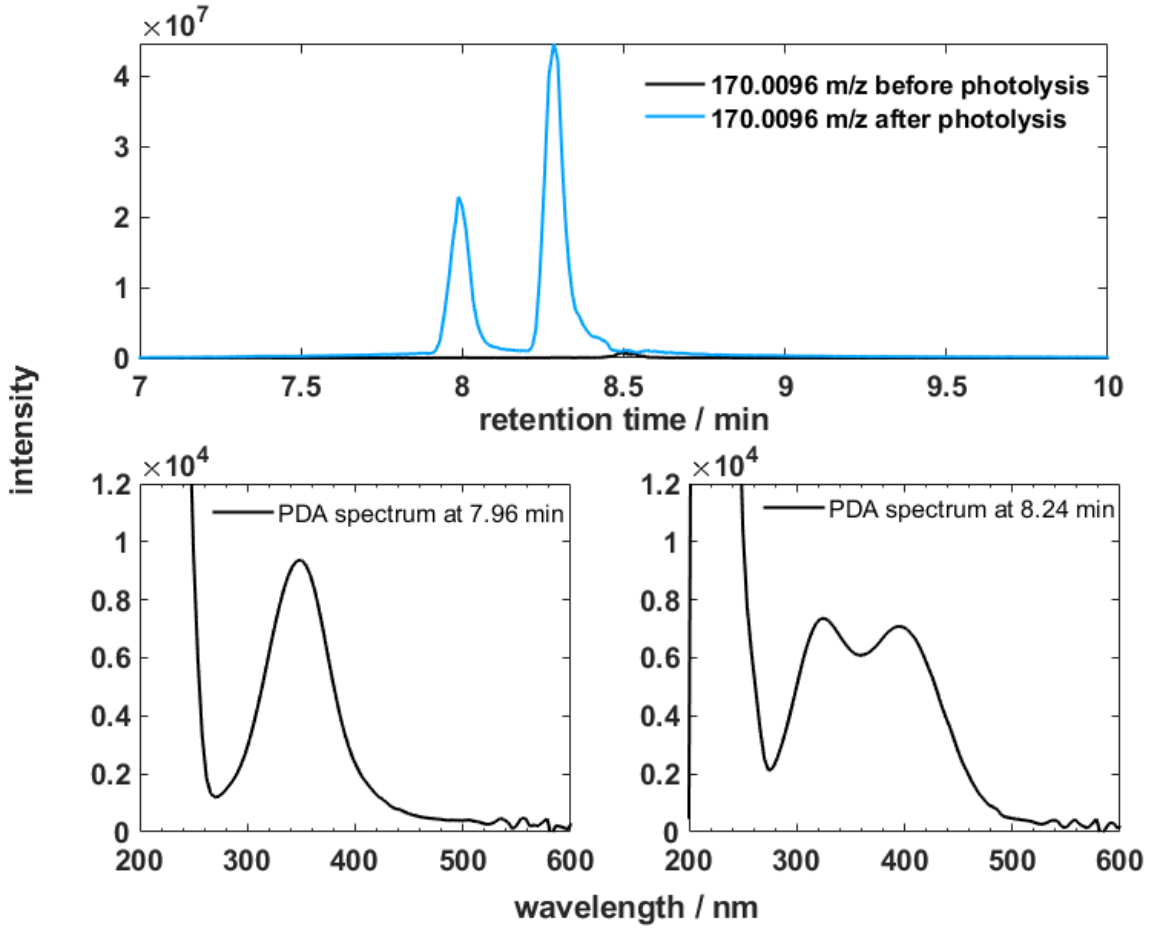

Figure 3.13: Selected ion current chromatogram for the m/z 170.0096 photolysis products (top) of 4NC in isopropanol and associated UV/Vis PDA spectra with the product retention times (bottom). The product eluted around 7.96 min has a distinct peak at 330 nm. The product around 8.24 min has a broad absorption band with a peaks at 325 nm and 400 nm.

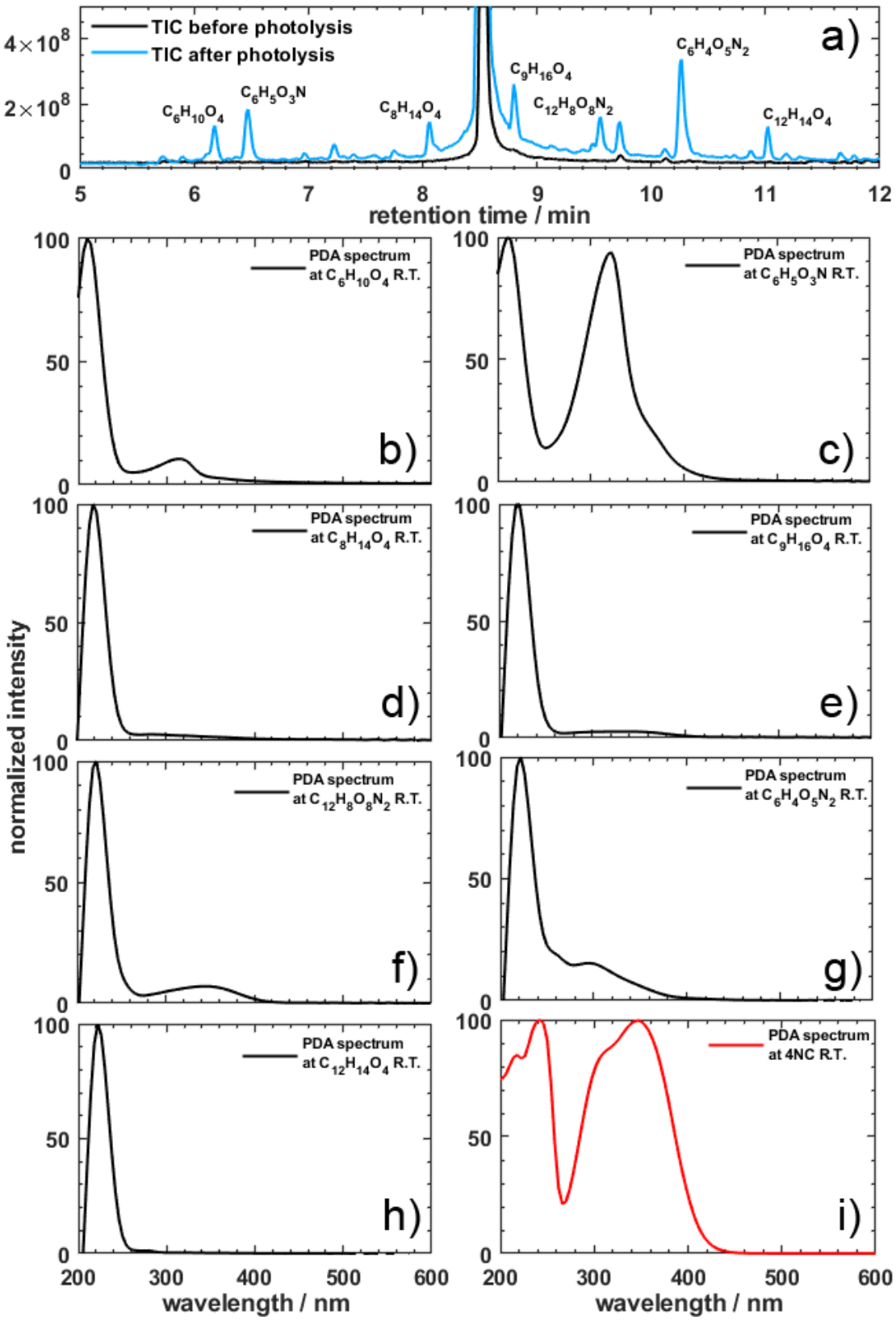

Figure 3.14: UV/Vis PDA spectra of products formed from photolysis of 4NC in isomalt glass. Each PDA spectrum was recorded approximately 0.07 min before the MS retention time. Formula assignments are calculated from the largest m/z value at each peak retention time.

Chapter 4

Ultrafast Excited-State Proton Transfer in 4-Nitrocatechol: Implications for the Photochemistry of Nitrophenols

Nitrophenols are a class of environmental contaminants that exhibit strong absorption at atmospherically relevant wavelengths, prompting many studies into their photochemical degradation rates and mechanisms. Despite the importance of photochemical reactions of nitrophenols in the environment, the ultrafast processes in electronically excited nitrophenols are not well understood. Here, we present an experimental study of ultrafast electron dynamics in 4-nitrocatechol (4NC), a common product of biomass burning and fossil fuel combustion. The experiments are accompanied by time-dependent quantum mechanical calculations to help assign the observed transitions in static and transient absorption spectra, and to estimate the rates of singlet-to-triplet intersystem crossing. Our results suggest that electronic triplet states are not efficiently populated upon 340 nm excitation as efficient proton transfer occurs in the excited state on a time scale of a few ps in water and tens of ps in 2-propanol. The following suggests that triplet states do not play a significant role in the photochemical reactions of 4NC in the environment and, by

extension, nitrophenols in general. Instead, consideration should be given to the idea that this class of molecules may serve as strong photoacids.

4.1 Background

Nitrophenols and their derivatives, especially 4-nitrocatechol (4NC), have been identified as some of the strongest chromophores within various types of light-absorbing organic aerosols in the atmosphere (also known as "brown carbon").[2,5,7,12,20,31,33,35,38,41,70,153,170] In atmospheric samples, the reported mass concentrations for 4NC may exceed those of other nitrophenols by factors from ten to one hundred.[28,30] Laboratory studies of organic aerosol produced from common anthropogenic molecules such as benzene and toluene have also been shown to yield significant amounts of 4NC.[43,171] With the environmental prevalence of 4NC, and its versatile solubility, it has become a popular model of brown carbon for laboratory studies.[70–72] Although the photochemistry of 4NC has been studied before, the mechanisms behind the excited-state dynamics that take place in photochemical reactions of para- nitrophenols, such as 4NC, are not as fully explored as their ortho- nitrophenol counterparts.[85,86,92,133,172,173]

Photochemistry of nitrophenols and other nitroaromatics is commonly assumed to proceed through the excited triplet state manifold,[126,173,174] based on the notion that they would exhibit similar photochemical characteristics to nitrobenzene.[125] The earliest studies of nitrobenzene identified photoreduction products from photochemistry conducted in alcohol solutions, namely 2-propanol, with evidence of hydrogen abstraction from 2-propanol as the likely reaction pathway.[93,127,175] Similar conclusions have been extrapolated to many other nitrobenzene derivatives.[53,135,176] No studies, however, have been able to definitively prove that the degradation of 4NC occurs via a direct reaction of its triplet state, leaving a possibility that photodegradation could occur through some other pathway such as charge or proton transfer in the excited singlet state manifold.[177]

Though the ultrafast dynamics have not been studied in 4NC specifically, relevant experiments have been done with nitrophenol isomers, predominately 2-nitrophenol. Takezaki *et. al.* used a transient grating approach to observe sub-ns transient signals in 2-nitrophenol, assigned to

its triplet state, and finding quantum yields for singlet-to-triplet intersystem crossing (isc) ≥ 0.86 for 2-, 3-, and 4-nitrophenol in a nonpolar solvent.[125] A study by Ersnt *et. al.* using time-resolved photoelectron spectroscopy on 2-nitrophenol supported previous observations by Takezaki *et. al.* and determined triplet state lifetimes of 0.1 ns and 0.5 ns in 2-propanol and in n-hexane, respectively.[85] Leier *et. al.* studied electron dynamics of 4-nitrophenol in aqueous solutions using conventional ultrafast transient absorption spectroscopy and found that the excitation to the lowest-energy band of 4-nitrophenol results in deprotonation at sub-nanosecond timescales, even under acidic (pH = 3-5) conditions.[62] Given that the most acidic proton in 4NC is the one in the para position from the nitro group,[99] the occurrence of similar ultrafast deprotonation in 4NC could have implications for the photochemical degradation of this molecule in the environment.

The main goals of this work are to examine the initial steps in 4NC photochemistry and study the effect of solvent on these processes. To this end, we have studied 4NC in both water and 2-propanol by means of ultrafast transient absorption spectroscopy over a broad spectral range. Experiments are accompanied by quantum chemical calculations using time-dependent density function theory (TDDFT) to determine and confirm the origins of the observed transients. We show that the excited 4NC undergoes a rapid proton transfer in both water and in 2-propanol, with only a small fraction of photoexcited 4NC relaxing in the triplet state. As a result, photoexcited 4NC is not expected to react through the triplet state and instead may behave as a photoacid on picosecond timescales.

4.2 Materials and Methods

4.2.1 Experimental Methods

Transient absorption spectroscopy experiments were conducted with 0.6 mM solutions of 4-nitrocatechol (4NC, Acros Organics, 97%) in aqueous (Milli-Q ultrapure) and 2-propanol (Fisher,

HPLC grade, 99.9%) solutions in a 2 mm quartz cell (Starna Cells, Spectrosil). The experiments were performed in standard non-collinear pump–probe fashion. The fundamental pulse at 800 nm (100 mW, 1 kHz) was partially focused on a CaF_2 plate to generate a white-light continuum for use as the probe pulse. Output of the femtosecond amplified system (Spitfire Ace, Spectra-Physics, MKS Instruments) was coupled to an optical parametric generator/amplifier to produce a 680 nm pulse, converted by a BBO crystal to 340 nm (0.5 mW) that was utilized as the pump beam. The time delay between pulses was scanned by a delay line (Newport, MKS Instruments), and the transient signal at each spectral component was recorded with a CCD-equipped spectrometer (Oriel, Newport, MKS Instruments). Excitation conditions generated transient signals that were confirmed to be in a linear regime for the detector response. The data indicate a probe pulse chirp of 500 fs mainly affecting wavelengths below 500 nm due to third-order nonlinear dispersion in CaF_2 crystal. This limits the possibility of quantitative analysis of the initial sub-ps dynamics, i.e., rise and build up of the transient signals, but does not affect interpretation of processes occurring on a picosecond timescale. The data presented in this work are from solutions which were air saturated and analyzed without any alteration of the intrinsic pH. Although the presence of dissolved oxygen could reduce the observed triplet state yields, the effects of energy-transfer to oxygen is expected to be minimal for short-lived triplets.[93] We confirmed, there are no appreciable indicators of signal arising from reactions with dissolved oxygen from a trial after purging with N_2. Static absorption spectra of the same solutions were collected using a Shimadzu UV-2450 spectrophotometer.

4.2.2 Computational Methods

The Q-Chem 5 quantum chemistry package was used in for the theoretical calculations in this work.[96] Geometry optimizations and TDDFT calculations were performed using the PBE0 hybrid exchange functional and the Pople 6-311+G(d) basis set.[98,178] Other functionals were tried, such as CAM-B3LYP, X3LYP, and M06-2X, however PBE0 produced vertical excitation energies

which had excellent agreement with the experimental spectra. The initial geometric configuration chosen to optimize was chosen based on the most stable conformer from Cornard *et. al.*[99] The conductor-like polarized continuum model (C-PCM) was used to account for solvation, with the default specifications used in Q-Chem. Simulated excitation spectra were produced using Gaussian distributions for each spectral line with FWHM = 43 nm. Orbital analysis was done with the generation of Natural Transition Orbitals (NTOs) in Q-Chem. The Alpha NTOs calculated within random-phase approximation were visualized in IQmol at a contour value of 0.05 $Å^{-3}$. From the character of the orbitals in these orbital images, inferences were made toward the most probable isc partners. The rates of isc, k^n_{isc}, between the first excited singlet state, S_1, and the lower energy triplet states T_n (n=1-3) can be expressed using Fermi's golden rule.[179]

$$k^n_{isc} = \frac{2\pi}{\hbar} |\langle \Psi_{(S_1)} | \hat{H}_{SO} | \langle \Psi_{(T_n)} \rangle|^2 \, \rho(\Delta E, \lambda, T) \tag{4.1}$$

A similar method was previously employed for 2- and 4-nitrophenol.[180] The bracketed term is the square of the spin-orbit coupling (SOC) matrix elements, which can be calculated directly in Q-Chem. $\rho(\Delta E,\lambda,\text{T})$ is the Franck-Condon (FC) weighted density-of-states,

$$\rho(\Delta E,\, \lambda,\, T) = \frac{1}{\sqrt{4\pi\lambda k_B T}} \, \exp\left(\frac{-(\Delta E + \lambda)^2}{4\lambda k_B T}\right) \tag{4.2}$$

where ΔE represents the energy difference between S_1 and T_n at their respective nuclear coordinates, and λ (often referred to as the reorganization energy) is the relative energy of the T_n state at the nuclear coordinates of the S_1 state. All calculations were performed at T = 300 K. Values for ΔE and λ were obtained by geometry optimization of the TDDFT excited states, in which the Tamm-Dancoff Approximation (TDA) needed to be used to overcome issues with imaginary roots in full TDDFT optimizations. Though TDDFT has been shown to work well with small molecules, it is recognized that the accuracy of TDDFT in determining the geometries of excited states is less accurate than coupled-cluster singles and doubles (CCSD).[181,182] It is also

recognized that full TDDFT often underestimates the stability of charge-transfer states, which are present in nitroaromatics,[128,174,183] though use of TDA may help in this regard.[184,185] If charge-transfer states are present in 4NC, the incurred errors will be directly dependent on the amount of charge-transfer character for each state.[186]

4.3 Results and Discussion

4.3.1 Indications from theoretical calculations

Figure 4.1 shows the measured static absorption spectrum of 4NC overlaid with the result from the ground-state TDDFT simulation. The experimental and modeled absorption spectra are in good agreement in terms of both the peak positions and overall shape, as demonstrated in the Figure 4.1 inset using the second derivatives of the spectral data. The best match to experimental observations has been achieved using PBE0/6-311+G(d) for modeling. The peaks at 347, 299, and 230 nm are assigned to excitations into S_1, S_3 and S_5 states, respectively. Excitations into S_2 and S_4 are not visible due to their negligibly small oscillator strengths predicted by the calculations. The extended data set of the molecule's energy structure and the oscillator strengths for transitions from S_0 into states up to S_5/T_5 are presented in Table 4.1 (with 2-propanol C-PCM) and 4.2 (with water C-PCM).

The potential energy diagram in Figure 4.3 (Fig. 4.4 for water) was used to identify starting coordinates for excited-state geometry optimizations, keeping in mind the -NO_2 group in excited-state nitroaromatics often exhibits a twisted form.[125,129,183,187] The minimized geometries for the planar S_0 and twisted S_1 are shown in Figure 4.2. Accordingly, Figure 4.3A shows that S_1 energy is reduced by twisting the -NO_2 group, which is especially noticeable at torsion angles greater than 50°. The S_1 state energy is minimized further by the pyramidalization of the -NO_2 group as shown in Figure 4.3B. The obtained angles at the minimum for each state were used for the initial step

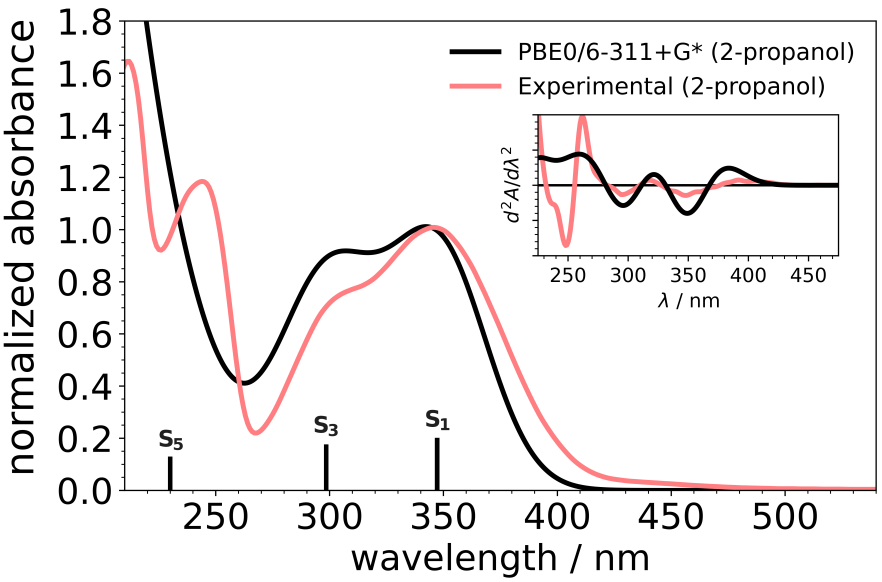

Figure 4.1: Simulated absorption spectrum for 4-nitrocatechol at the TD-PBE0/6-311+G(d) level of theory (black trace) compared to the experimental absorption spectrum (red trace). The experimental spectrum was collected in 2-propanol, and the simulated spectrum employed C-PCM to mimic such conditions. The spectra are normalized to the peak value of the lowest-energy band at 347 nm.

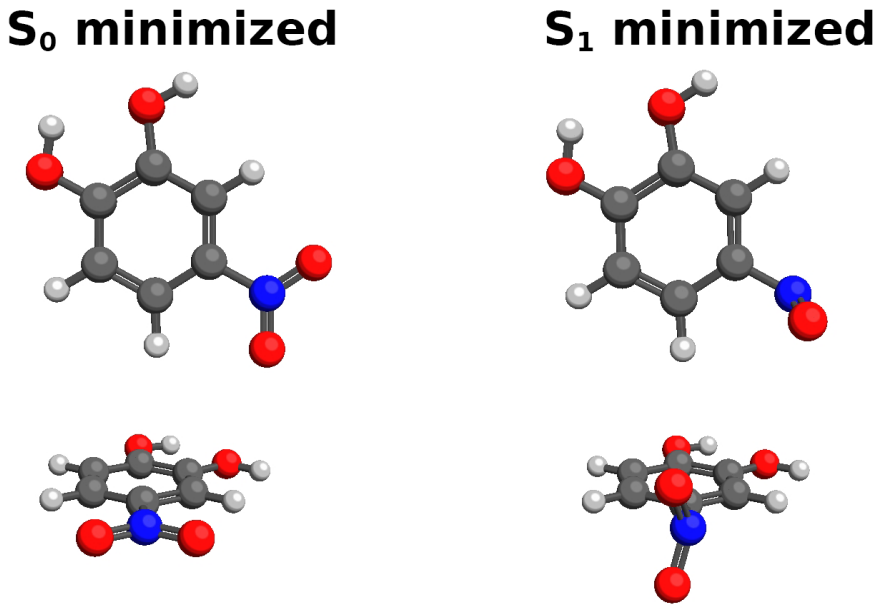

Figure 4.2: Minimized geometries of the ground state and first excited state in 4NC.

Table 4.1: Vertical excitation energies (VEEs) from time-dependent density functional theory calculations for the ground state of 4NC at the TD-PBE0/6-311+G(d) level of theory with a C-PCM for 2-propanol.

State	Total energy [au]	VEE [eV]	VEE [nm]	Oscillator Strength (f)
S_1	-586.5985057	3.5706	347.2	2.017×10^{-1}
S_2	-586.5832187	3.9866	311.0	1.733×10^{-7}
S_3	-586.5770892	4.1534	298.5	1.764×10^{-1}
S_4	-586.5589382	4.6473	266.8	4.039×10^{-4}
S_5	-586.5316219	5.3906	230.0	1.296×10^{-1}
T_1	-586.6355414	2.5628	483.8	0
T_2	-586.6166768	3.0761	403.0	0
T_3	-586.6033993	3.4374	360.7	0
T_4	-586.6021297	3.4720	357.1	0
T_5	-586.5809496	4.0483	306.3	0

Table 4.2: Vertical excitation energies (VEEs) from time-dependent density functional theory calculations for the ground state of 4NC at the TD-PBE0/6-311+G(d) level of theory with a C-PCM for water.

State	Total energy [au]	VEE [eV]	VEE [nm]	Oscillator Strength (f)
S_1	-586.6002712	3.5514	349.1	1.930×10^{-1}
S_2	-586.5842646	3.9870	311.0	3.437×10^{-7}
S_3	-586.5787231	4.1378	299.6	1.806×10^{-1}
S_4	-586.5596949	4.6556	266.3	4.449×10^{-4}
S_5	-586.5325425	5.3944	229.8	1.275×10^{-1}
T_1	-586.6374488	2.5398	488.1	0
T_2	-586.6175373	3.0816	402.3	0
T_3	-586.6043871	3.4394	360.5	0
T_4	-586.6038340	3.4545	358.9	0
T_5	-586.5821313	4.0450	306.5	0

of TDDFT/TDA excited-state geometry optimizations. SOC constants between S_1 and (T_1-T_5) are shown as a function of torsion and pyramidalization in Figure 4.3C and 4.3D. It is important to note that in Q-Chem the labels of each state do not account for energetic crossings and may reset to the ordering of states at each TDDFT/TDA calculation. Energetic rearrangement of states may be the cause of large variations in SOC constants in 4.3D. The optimized geometries of each state are provided in Appendix C.

The SOC constants and the corresponding k_{isc}^{n} values estimated using Eq. 4.1 are provided in Table 4.3. The strongest coupling is obtained for S_1-T_3 states, but only for the initial geometry. This follows nicely with El-Sayed's rules,[188] as analysis of the natural transition orbitals (NTOs, Fig. 4.5) predicts $\pi\pi^*$ and $n\pi^*$ characters for S_1 and T_3, respectively. The rate constant for S_1-T_1 isc is effectively zero, which is common for states with large energy differences when using a Gaussian distribution in $\rho(\Delta E,\lambda,T)$.[189] While the S_1-T_3 isc transition is expected to be the fastest, the estimated isc rate constant for S_1-T_3 too low resulting in a long lifetime ($\tau \approx 22$ ns) that far exceeds a timescale observable with the ultrafast methods in this work. It is important to note that the use of Eq. 4.1 relies on the Condon approximation, which assumes that there is a negligible change in the electronic coupling with geometric reconfiguration between initial and final states.[190] It is clear from Figure 4.3C that the Condon approximation alone is not enough to estimate electronic coupling. This is also evident from smaller than expected k_{isc}^{n} values in Table 4.3, especially for T_1 and T_2. Further computational studies could evaluate the inclusion of second-order spin-orbit coupling elements toward achieving more accurate isc rate estimates for this system.[191,192]

Although not evident in the FC excitations, a deeper analysis of the NTOs in Fig. 4.6 reveals the development of twisted intramolecular charge transfer (TICT) character as 4NC assumes the S_1 geometry. Despite working well for the electronic structure from the ground state, PBE0 could ultimately fail to estimate the stability of the charge-transfer states. The Coulomb-attenuated functional CAM-B3LYP has been shown to yield significant improvements toward predicting

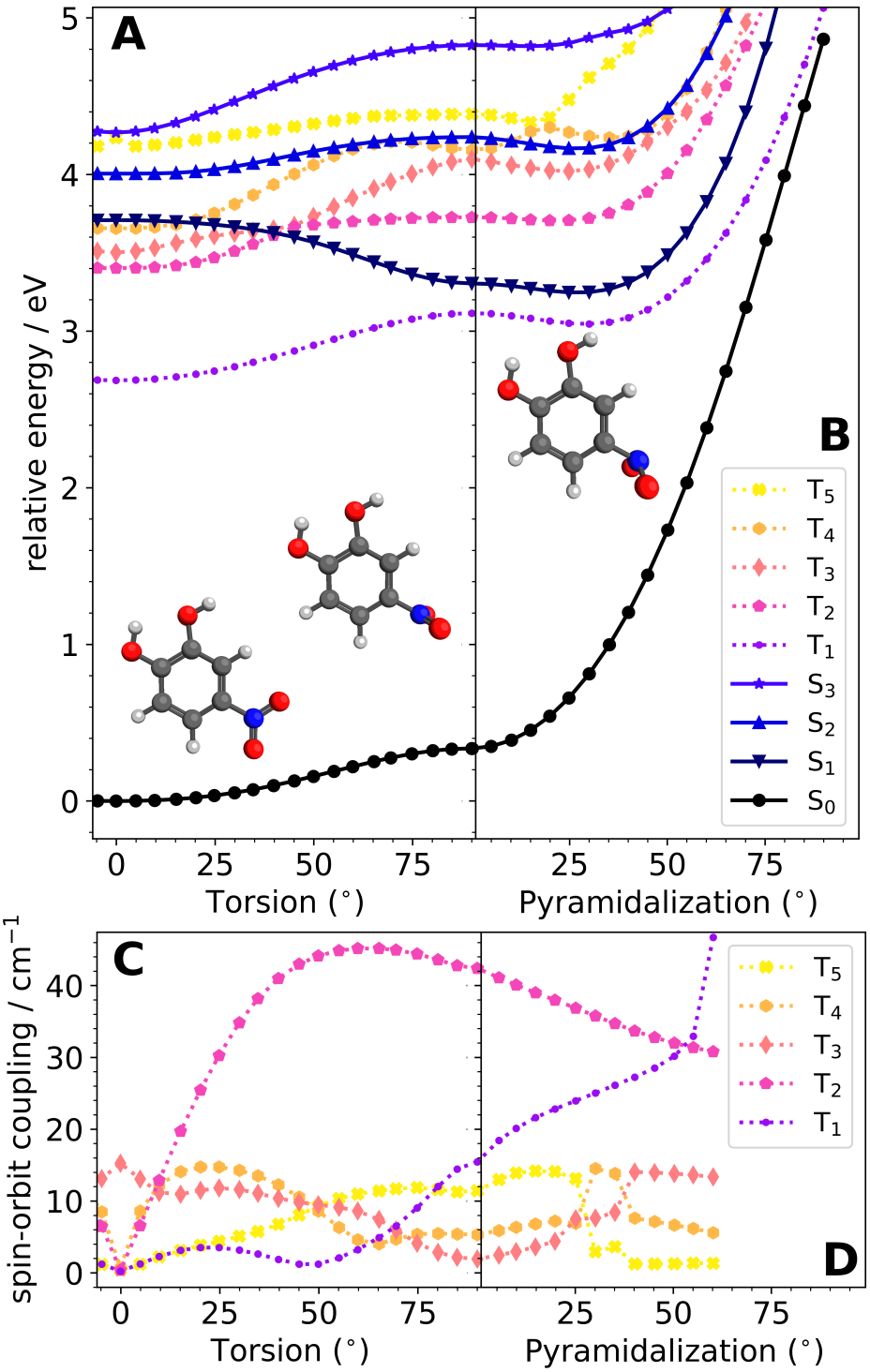

Figure 4.3: The effects of torsion and pyramidalization of the -NO_2 group in 4-nitrocatechol, starting from the ground-state geometry. The total energy for each state (S_0-S_3 and T_1-T_5) are shown in panels A and B and the spin-orbit coupling constants for S_1-(T_1-T_5) are shown in panels C and D, as calculated at the TD/TDA-PBE0/6-311+G(d) level with a C-PCM for 2-propanol.

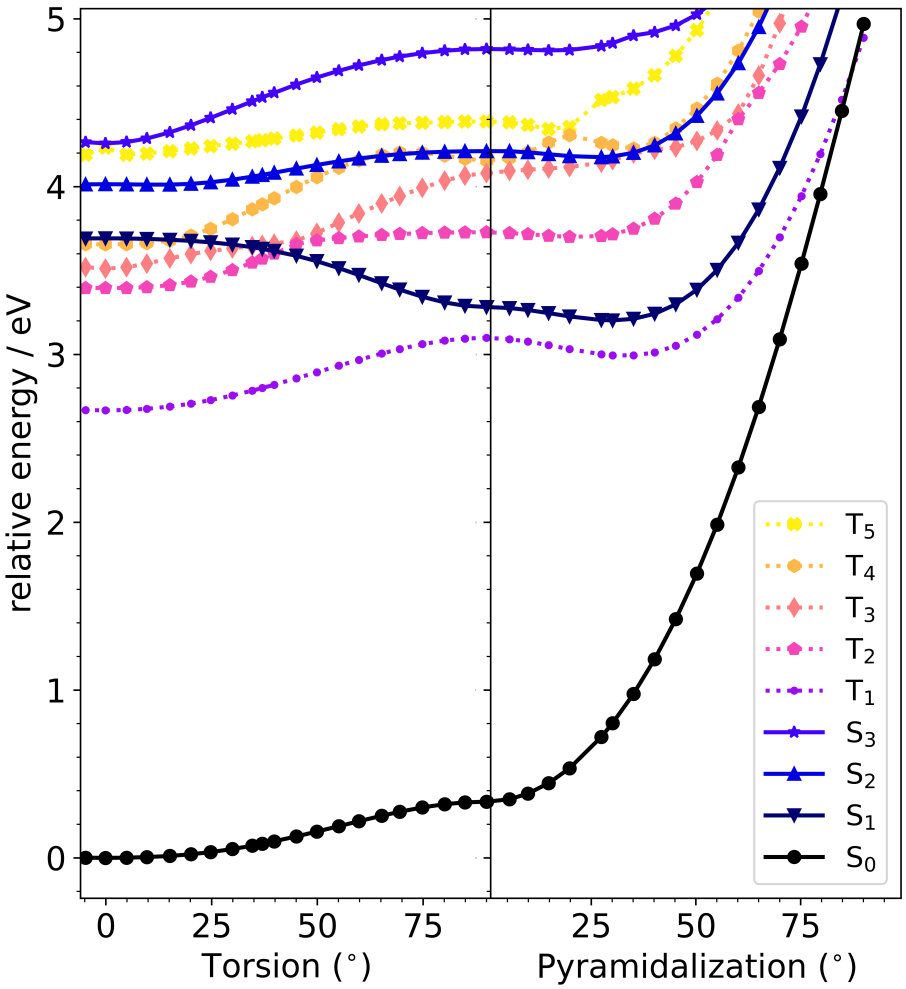

Figure 4.4: The effects of torsion and pyramidalization of the -NO_2 group in 4NC, starting from the ground-state geometry. The total energy for each state (S_0-S_3 and T_1-T_5) are shown in panels A and B, as calculated at the TD/TDA-PBE0/6-311+G(d) level with a C-PCM for water.

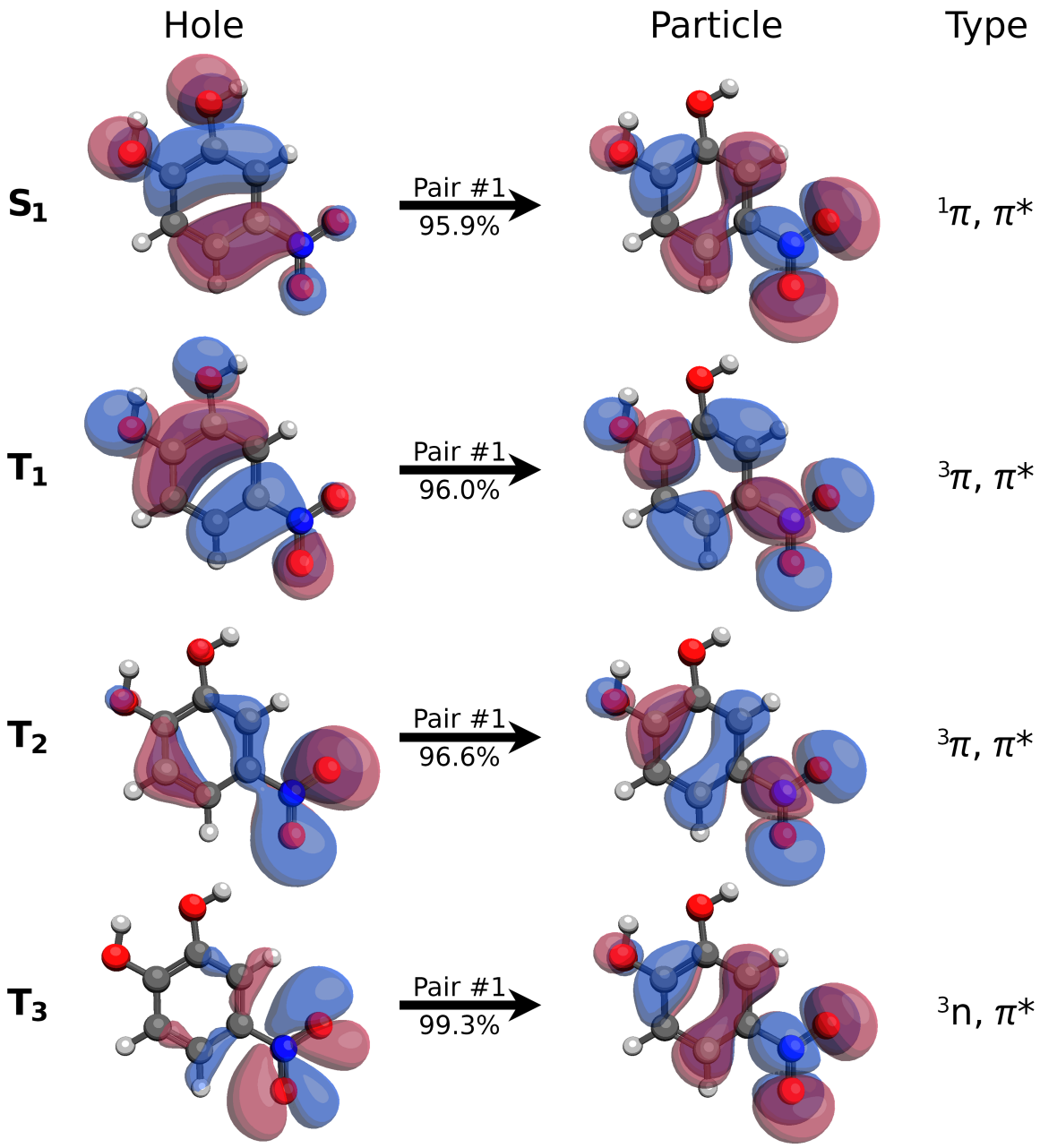

Figure 4.5: Natural transition orbital (NTO) pairs calculated at the TD-PBE0/6-311+G(d) level of theory. The transitions for S_1, T_1, and T_2 are all of $\pi\pi^*$ nature, while T_3 is the only one to exhibit $n\pi^*$. As discussed in the main text, this has positive implications toward the probability of isc from S_1 to T_3.

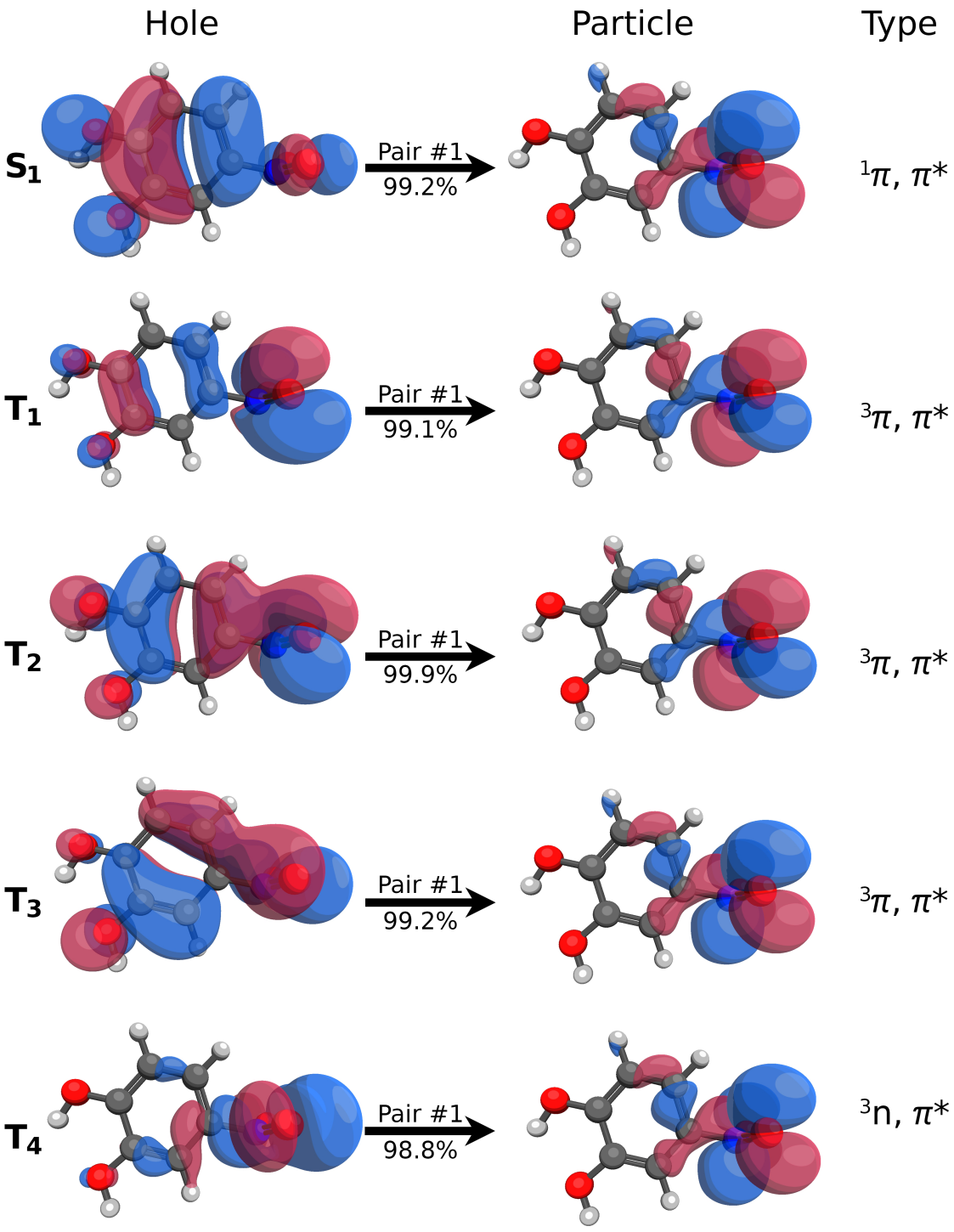

Figure 4.6: NTO pairs calculated at the TD-PBE0/6-311+G(d) level of theory at the **minimum geometry of the S_1** state, the twisted conformer of 4NC. T_4 is included because it appears that it is the T_3 nπ^* transition in the Franck-Condon conformer, and that the Franck-Condon T_4 moves lower than the Franck-Condon T_3 at S_1 geometry.

Table 4.3: Spin-orbit coupling constants (TD-PBE0/6-311+G(d)) and estimated rate constants for intersystem crossing for S_1 to T_n transitions of 4-nitrocatechol in 2-propanol

Transition (S_1-T_n)	**Spin-orbit coupling constant [cm^{-1}]**	k_{isc}^{n} **(S_1-T_n) [s^{-1}]**
with PBE0/6-311+G(d)		
T_1	0.235	1.84×10^{-1}
T_2	0.346	1.36×10^{2}
T_3	15.3	4.53×10^{7}
with CAM-B3LYP/6-311+G(d)		
T_1	0.298	3.25×10^{-7}
T_2	0.309	2.88×10^{3}
T_3	0.810	5.95×10^{4}

the properties of charge-transfer type molecules.[193–195] With this in mind the aforementioned calculations with PBE0 were also done with CAM-B3LYP and the analogous results are shown in Fig. 4.7 within the TDA. Interestingly, the FC excitation of $S_0 \rightarrow S_1$ is blue-shifted nearly 40 nm compared to experimental observations and what is predicted by PBE0. Optimization of S_1 with CAM-B3LYP does also favor the TICT form, which is again higher in energy relative to the ground state compared to PBE0. Rough estimates of k_{isc}^{n} from the triplet-state minima in Fig. 4.7 yield isc rate constants even lower than those PBE0 (Table 4.3). In summary, it seems the choice of the functional does not result in significant changes in the isc rate constant estimation.

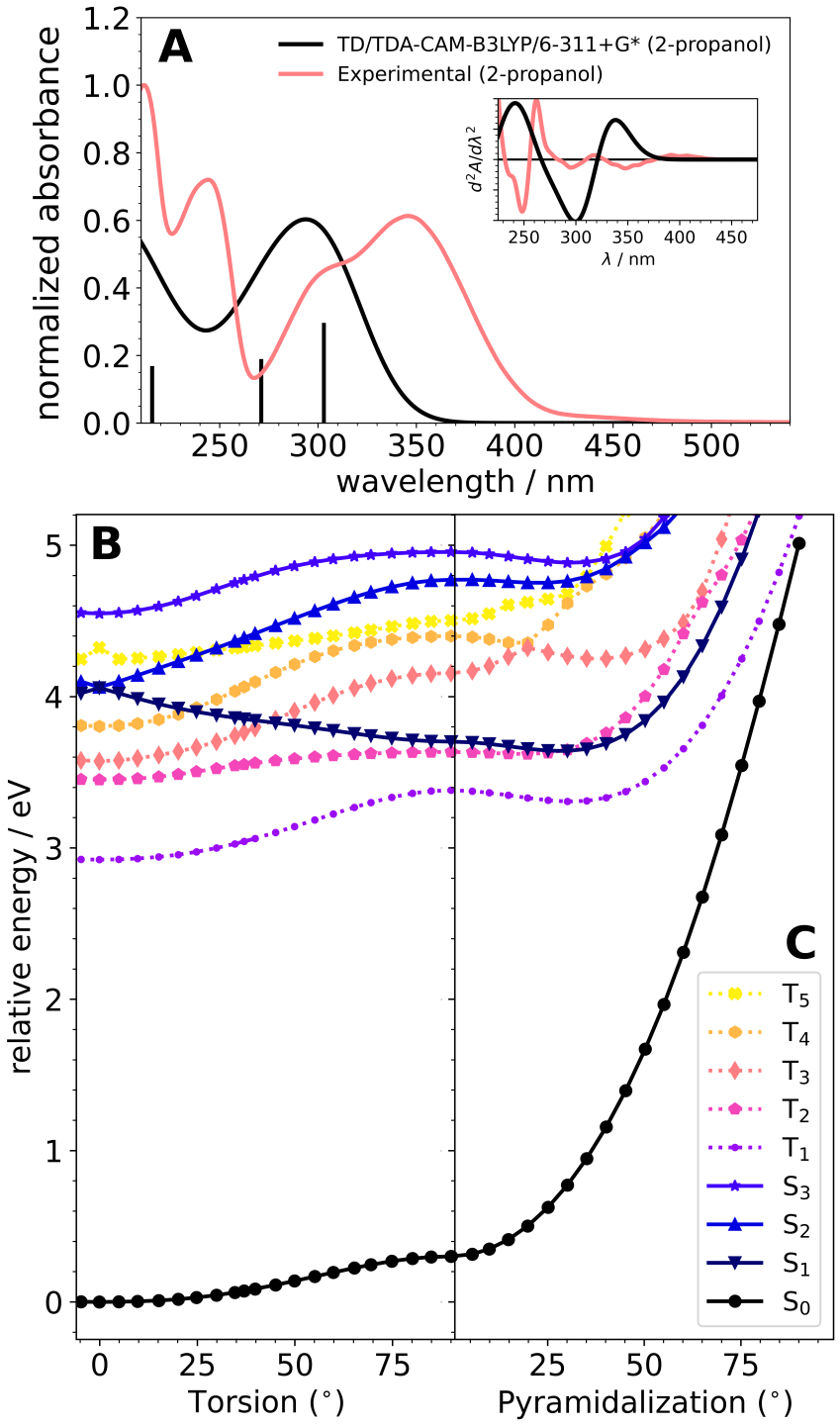

Figure 4.7: Vertical excitation spectra (A) from the minimized ground state of 4NC and the effect of torsion angle and pyramidalization angle of the -NO_2 on the potential energies of excited singlets and triplets in 4NC with a C-PCM for water at TD/TDA-CAM-B3LYP/6-311+G(d) level of theory.

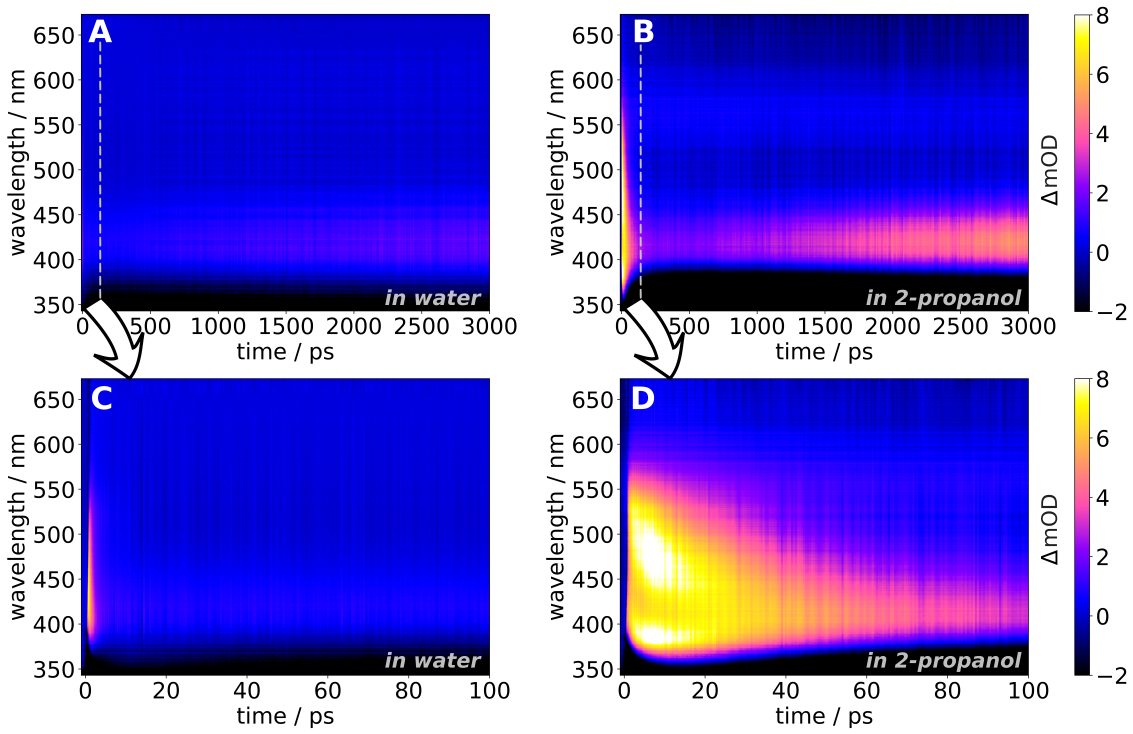

Figure 4.8: Transient absorption contour plots of 4-nitrocatechol pumped at 340 nm. Panels A and B show the full experimental time trace collected over 3000 ps, illustrating the rise of signal between 400 and 450 nm. Panels C and D are zoomed in on the first 100 ps of the ultrafast signal.

4.3.2 Identification of transient signals

The transient absorption spectra obtained from 4NC in water and 2-propanol are shown as a false color map in Figure 4.8. Figures 4.8A and 4.8B show transient absorption (ΔOD) for the full 3000 ps measured after the excitation, while Figures 4.8C and 4.8D are focused on the initial 100 ps time dynamics. There is a striking difference between the transient signals in 2-propanol and water – the transients in water are shorter-lived than in 2-propanol.

Figures 4.9A-C shows dynamics for 4NC in water. The transient signal build-up occurs in under 1 ps at 440 nm. The absorption features at these timescales are likely the result of twisted intramolecular charge transfer (TICT), which indeed should occur at sub-ps timescales in other nitroaromatics.[187] The presence of an isosbestic point at 510 nm in Figure 4.9A (blue/violet traces) is indicative that the sub-ps state converts into a new state manifesting itself as a broad absorption

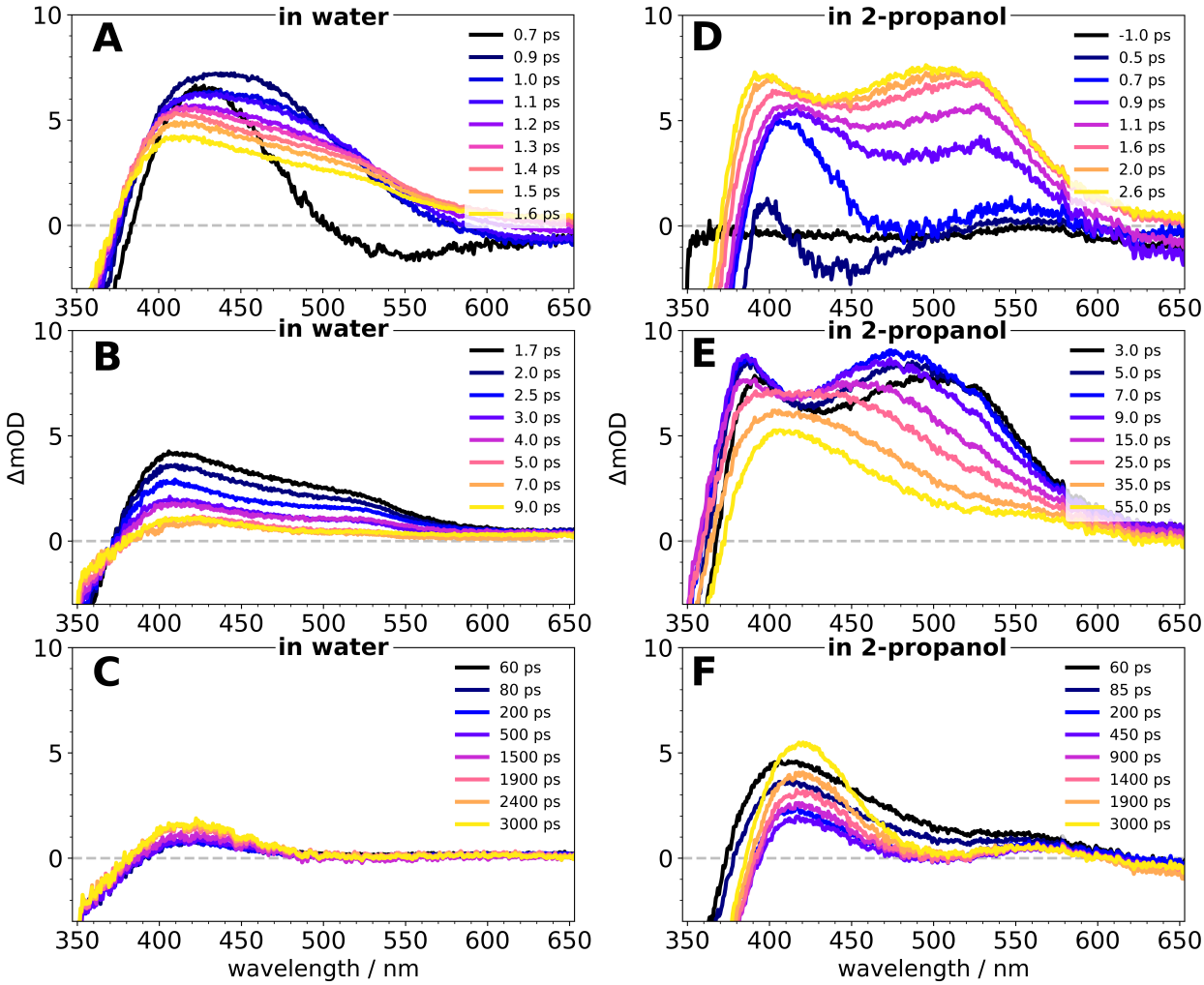

Figure 4.9: Individual transients observed at various times during the ∼3 ns experiment. The time intervals for each subpanel were chosen in an attempt to highlight the unique spectra which appear at different times. Panels A, B, and C are data from aqueous experiments, and panels D, E, and F are data from 2-propanol experiments. The delay times are indicated in each panel by trace color.

band from 400 nm to 600 nm. This absorption feature dissipates within the next 10 ps reaching a steady plateau (Figure 4.9C). The sustained signal has a resemblance to the observations for 4-nitrophenol, a structurally similar molecule to 4NC, by Leier *et. al.*, where a similar absorption spectrum at longer time scales has been assigned to the anion of 4-nitrophenol.[62] Hence, we hypothesize that this new state could be a result of intermolecular excited-state proton transfer (ESPT) from 4NC to the solvent. This is of particular interest, as these signals appear not only in water but also in less polar 2-propanol.

The spectral evolution for 4NC in 2-propanol is shown in Figures 4.9D-F. Again, the TICT appears to be present at early delay times. In contrast to the spectral dynamics in aqueous solution, a new excited-state absorption band (yellow curve in Fig. 4.9D) is formed in a few ps, which is likely the result of rapid S_1-T_n isc after the reorientation of the -NO_2 group. This underlines an important difference between the aqueous and organic solvents, as isc did not seem to occur in the former. The theoretical calculations suggest that the isc destination is either T_1 or T_2, though this is difficult to confirm experimentally. Following isc, the excited-state absorption within the triplet manifold (Fig. 4.9E) evolves toward an absorption band similar to the one that appeared between in water (Fig. 4.9B). This absorption feature decays with $\tau \approx 58$ ps in 2-propanol and $\tau \approx 2$ ps in water. This further confirms the notion that signals at longer times (420 nm, 3 ns) appear to be associated with similar chemical species in both solvents. Most likely it corresponds to excited-state absorption by a higher excited state in the anion, which we will denote as X^-_* in Figure 4.10.

To support our conclusions about facile ESPT in 4NC, Figure 4.11 shows transient spectra at 3000 ps in both solvents overlayed with the static absorption spectra of singly- and doubly-deprotonated 4NC recorded in water. The static spectra were measured by titrating aqueous 4NC with potassium hydroxide, and the spectrum pH dependence is shown in Figure 4.12. The mono-deprotonated anion of 4NC, or $4NC^-$, has a maximum in the same region at 425 nm. Assuming $4NC^-$ is being formed in both solutions, the slower-evolving transient signal being observed in

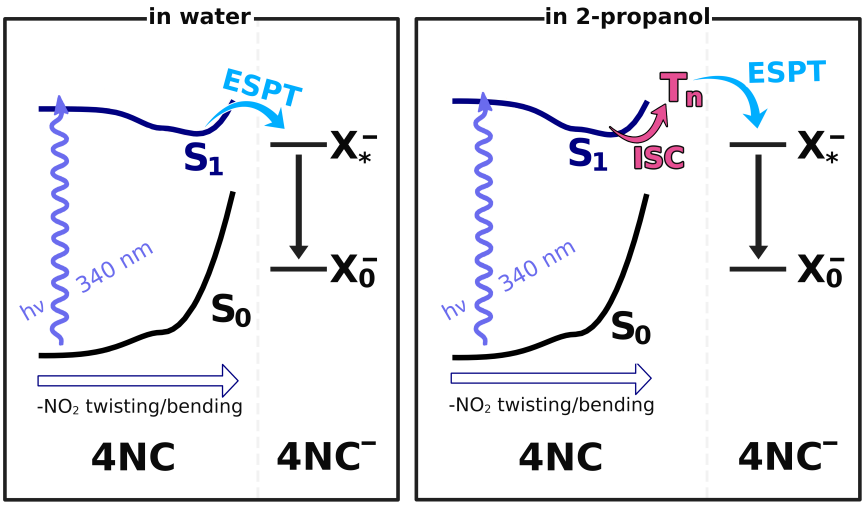

Figure 4.10: Schematic diagram representing the solvent-dependent excited state dynamics observed with 4NC. The left shows 4NC undergoing ESPT while still in a singlet state in water, and the right shows 4NC first going through isc prior to ESPT.

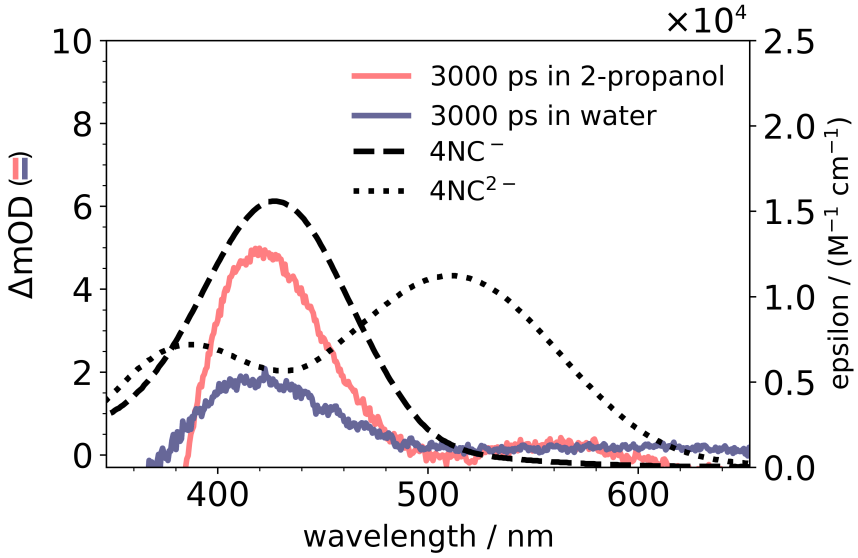

Figure 4.11: Overlayed spectra of the long-lived transient absorption signal in 2-propanol (salmon) and water (violet) on the left axis with the extinction spectra of the mono- (dashed) and doubly- (dotted) deprotonated forms of 4NC on the right axis.

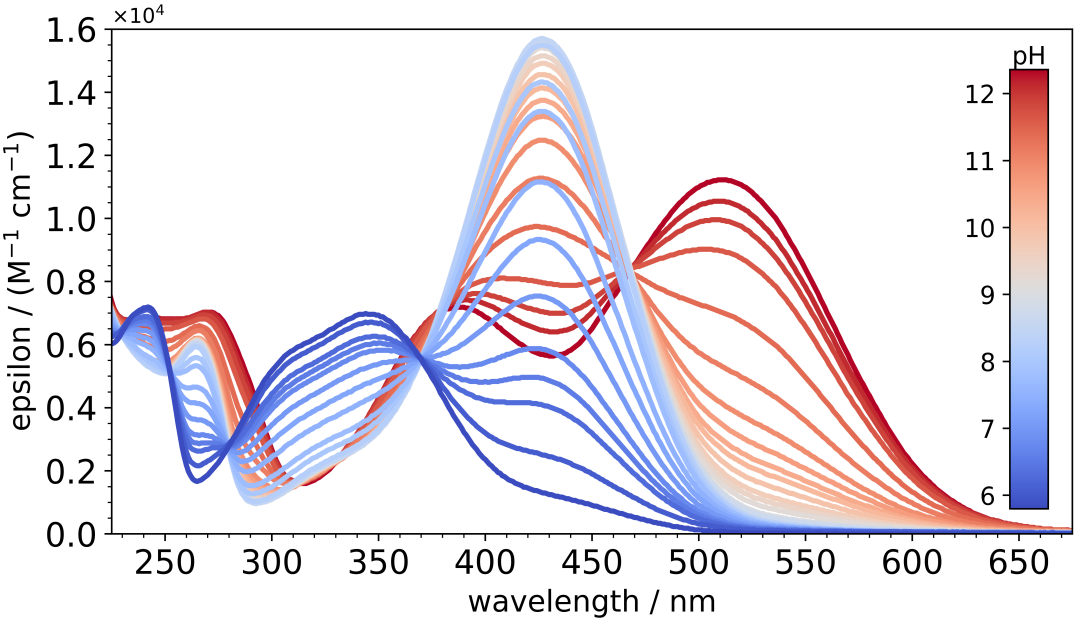

Figure 4.12: UV/vis absorption spectra of 4NC at a range of pH values, from the 'native' pH of 4NC in water to 12.4 adjusted by KOH. Two deprotonations are observed, first from the #1 C atom to form $4NC^-$ and subsequently from the #2 C atom (per IUPAC convention).

2-propanol is not surprising. Water is a much more efficient acceptor for excited-state intermolecular proton transfer than alcohols, leading to a significantly faster transfer.[196]

4.3.3 Ultrafast rates of isc and ESPT

Figure 4.13 compares the time dynamics for 4NC in 2-propanol and water, at the probe wavelengths roughly corresponding to the appearance and subsequent disappearance of excited-state absorption. The data have been fitted using single exponential functions with time constants being reported in Table 2. We note, it is not possible to precisely determine time constants for each transformation due to the strong overlap of their broad spectral lines. With absorption by X_*^- overlapping (yellow trace in Fig. 4.9E) with the signal by T_n (475 nm, black/blue traces in Fig. 4.9E), the decay lifetime reported for T_n would be an upper limit for the transition from T_n to X_*^-. At 525 nm, the signal decays with a time constant $\tau \approx 24$ ps, perhaps a better estimate for the timescale of ESPT in 2-propanol. The only transient signal that can be quantitively an-

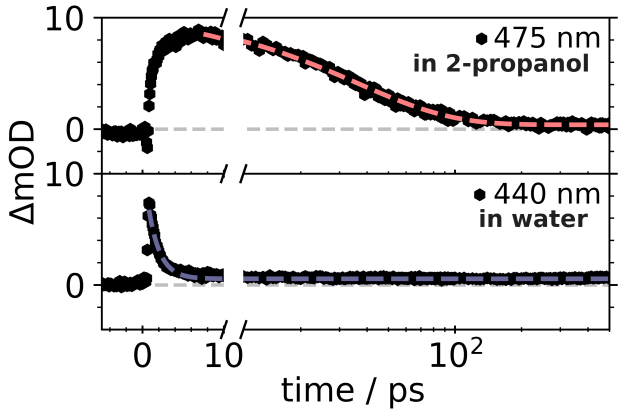

Figure 4.13: Transient absorption traces the longest-lived triplet signals by 4NC in 2-propanol (top) and water (bottom). The broken x-axis is used to illustrate the rapid decay of the triplet state. The left x-axes show the initial rise of signal within 10 ps. The overlayed dashed lines are the results of fitting the signal

Table 4.4: Wavelengths of maximum change in absorbance and effective lifetimes of transient processes in 4-nitrocatechol

Species	Description	Maximum $\triangle$OD Wavelength	τ_{decay} [ps]
2-propanol			
TICT S_1	Neutral excited state	405 nm	n.d.[a]
T_n	Neutral excited state	475 nm	6 ± 1
X_*^-	Anion excited state	405 nm	58 ± 2
water			
TICT S_1	Neutral excited state	440 nm	n.d.
X_*^-	Anion excited state	405 nm	1.7 ± 0.1

[a]These lifetimes were not determined due to the overlapping of absorption signals or too rapid change. The uncertainty provided is a 95% confidence interval from the fit.

alyzed for 4NC in water is associated with X_*^- decay within 1.7 ps, which effectively represents the overall transient response. As such times are exceedingly short for spin forbidden transitions, we hypothesize, ESPT is a primary mechanism of decay and occur in both solvents on ultrafast timescales.

The striking contrast in time scales of the ESPT process in aqueous and 2-propanol solutions (Figure 4.13) is clear. Due to the complexity of transient spectrum and significant overlap of the broad absorption bands, the ESPT rates cannot be precisely determined from the current

experimental data. However, a rough estimate can be made based on decay times at 405 nm ($\sim$2 ps), putting the ESPT rate constant at $\sim 5 \times 10^{11}$ s^{-1}. This ultrafast rate approaches what is believed to be the upper limit of ESPT rates at $\sim 10^{13}$ s^{-1} reported previously.[197–199] Since water is a much more effective base than 2-propanol, it allows for ESPT to occur almost immediately after the TICT. In contrast, the lag in ESPT in 2-propanol allows for isc to the triplet manifold to take place, after which the ESPT occurs from a triplet state.

The transient absorption signals at 550-600 nm range do not fully vanish within 3 ns, suggesting a small population remains in a triplet state. In previous work on broadband photochemical degradation of 4NC in 2-propanol,[90] it was believed triplet 4NC would decay by abstracting a hydrogen atom from 2-propanol. The observed effective photochemical degradation yield was found to be $\sim 10^{-5}$ for the loss of 4NC in 2-propanol. This suggests that either the triplet state has a low quantum yield, or it is not reactive with the solvent. The energies of the T_1 (2.6 eV), T_2 (3.1 eV), and T_3 (3.4 eV) states are lower than the C-H bond energy (4 eV), hence the presence of the energy potential barriers is also likely to limit such a process. If due to the dominant ESPT process only a small fraction of the excited molecules remains at the triplet state, this would explain relatively slow, yet observable, photodegradation in 4NC.

Ultrafast time scales of ESPT in 4NC indicate the role of triplet states toward the environmental photochemistry of 4NC and other nitrophenols may be minimal. Some studies have identified nitrosophenol compounds as potential intermediates in the photodegradation of nitrophenols,[53,82,90,112,177] which may be the result of an electron transfer processes following the ESPT. While nitroaromatics are often classified as having similar characteristics across the board, perhaps further delineation is necessary among these "push-pull" type nitrophenols. Nitrophenols are strong chromophores, their S_1 transitions are usually of $\pi\pi^*$ instead of $n\pi^*$ character, and they have strong indications toward being effective photoacids.

4.4 Conclusions

This work utilized transient absorption spectroscopy to compare the photophysical dynamics of 4NC in an organic environment (2-propanol) and the aqueous phase. Upon excitation at 340 nm, the S_1 state is immediately populated in both solvents. The mechanisms within the triplet manifold differ between the two solvents. In 2-propanol there are indications of isc into a triplet state, most likely T_2 or T_3 as indicated by quantum chemical calculations. There is no isc process apparent in the aqueous phase; instead, it appears to be an ultrafast ESPT producing ground-state 4NC anion within 10 ps. The resulting spectra at long delay times ($\sim$3 ns) in both solvents are spectrally similar to the mono-deprotonated anion $4NC^-$, indicating that ESPT happens in both solvents. Unlike in the aqueous phase, ESPT in 2-propanol takes longer as it appears to first go through a relatively short-lived S_1-to-T_n conversion. Because ESPT reduces the triplet state yield, it reduces the efficiency of the photodegradation of 4NC in either aqueous or organic matrices and minimizes the probability of secondary triplet-state chemistry of 4NC.

The results in this work could have implications toward the general treatment of nitrophenol photochemistry. While there is evidence of the short-lived triplet states, it is worth considering the role that the anion could play a significant role towards condensed-phase photodegradation of 4NC. The results show 4NC has photoacidic characteristics and this conclusion is in good agreement with recent studies on 4-nitrophenol. It is worth emphasizing that the ultrafast nature of the proton transfer in 4NC appears to approach the territory of "super" photoacids, particularly in water. Further studies should be done to quantify the rate of ESPT in 4NC or other para-nitrophenols.

Chapter 5

Unraveling the Ambiguities in the Theoretical Determination of Intersystem Crossing Rates

Recent works have sought to develop theoretical frameworks with which rate constants for intersystem crossing processes in organic molecules can be estimated. Built upon Fermi's Golden Rule and the energy gap law, a handful of useful equations have been developed that combine statistical mechanics with quantities that may be obtained from quantum chemical calculations. It is evident from a review of relevant literature that there is some ambiguity in the application of this framework in practice. This work seeks to highlight and dispose of any ambiguity and apply the framework on nitrobenzene as a reference molecule. This work is provided in this dissertation as an extension to the computational work done in Chapter 4, and as a potential guide for future researchers trying to address similar questions.

5.1 Background

Intersystem crossing is a nonradiative electronic transition in which an electron changes spin, changing the overall spin multiplicity of the molecule. Although singlet-to-triplet optical transitions are normally forbidden by the selection rules proposed by the formalisms of quantum mechanics, spin-orbit coupling between states results in a mixing of singlet/triplet character, producing new states which are not as rigidly confined by formal selection rules. Many organic molecules, including nitrobenzene and nitrophenols, have a high propensity toward excited-state intersystem crossing processes. The quantification of intersystem crossing rates can be difficult with current experimental methods. Consequently, substantial efforts have been dedicated to devising a theoretical framework for the determination of intersystem crossing rates through a combination of quantum mechanical and classical approaches.

In the quantum view, it has been well-established that nonradiative transitions can be described by first-order perturbation theory and is known as Fermi's Golden Rule. The transition probability (per unit time, also known as rate constant) W_q for intersystem crossing from state Ψ_i to state Ψ_f can be estimated with the expression in Equation 5.1 where $\hat{H}_{SO}$ is the time-dependent spin-orbit coupling Hamiltonian (which is implemented into many modern quantum chemical programs), and the delta function fulfils the requirement of energy conservation in the transition.

$$W_q = \frac{2\pi}{\hbar} \left| \left\langle \Psi_i | \hat{H}_{SO} | \Psi_f \right\rangle \right|^2 \delta \left(E_i - E_f \right) \tag{5.1}$$

From here it is common to assume that the spin-orbit coupling depends purely on the electronic part of the wavefunction. This yields the expression in Equation 5.2, where ψ_i and ψ_f represent the electronic parts of states Ψ_i and Ψ_f, and the overlap integrals $\langle \nu_{ji} | \nu_{kf} \rangle$ for the relevant

vibrational modes are factored out and summed.

$$W_q = \frac{2\pi}{\hbar} \left| \left\langle \psi_i | \hat{H}_{SO} | \psi_f \right\rangle \right|^2 \sum_k |\langle \nu_{ji} | \nu_{kf} \rangle|^2 \, \delta \left(E_{ji} - E_{kf} \right) \tag{5.2}$$

From a starting point similar to Equation 5.2, Englman & Jortner derive the utility of a line shape function as an approximation for the intractable summation terms.[200] These authors presented a theoretical approach with two limiting cases, a "weak vibronic coupling" limit and a "strong vibronic coupling" limit. These two regimes are presented in Figure 5.1. In this view, the strength of the interaction is driven by a change on molecular geometry, Δq, between the initial and final states. In the strong vibronic coupling case, the transition probability W_c is given by Equation 5.3, where C is the coupling constant between the initial and final states, E_M represents the energy change when switching geometries between initial and final states, and E_A (shown in Figure 5.1) is the energy difference between the crossing point of the two surfaces and the initial energy.

$$W_c = \frac{2\pi}{\hbar} C^2 \frac{1}{\sqrt{2\pi E_M k_B T}} \exp\left(-\frac{E_A}{k_B T} \right) \tag{5.3}$$

This expression is remarkably similar to the Marcus Theory expression for the electron transfer rate constant, k_{et}, provided in Equation 5.4. Nominally these two theories are used for different phenomena: the expressions derived by Englman & Jortner are meant to describe an intramolecular intersystem crossing process, while the Marcus theory is most used to describe the transfer of electrons in intermolecular chemical reactions. For this reason, the terms in Equation 5.4 are different, with $\Delta G^{\ddagger}$ being the change in Gibbs free energy between the reactants and the intersection of the reactant and product surfaces, which is pictorially equivalent to E_A in Figure 5.1. The λ in the pre-exponential factor is the reorganization energy, which is meant to account

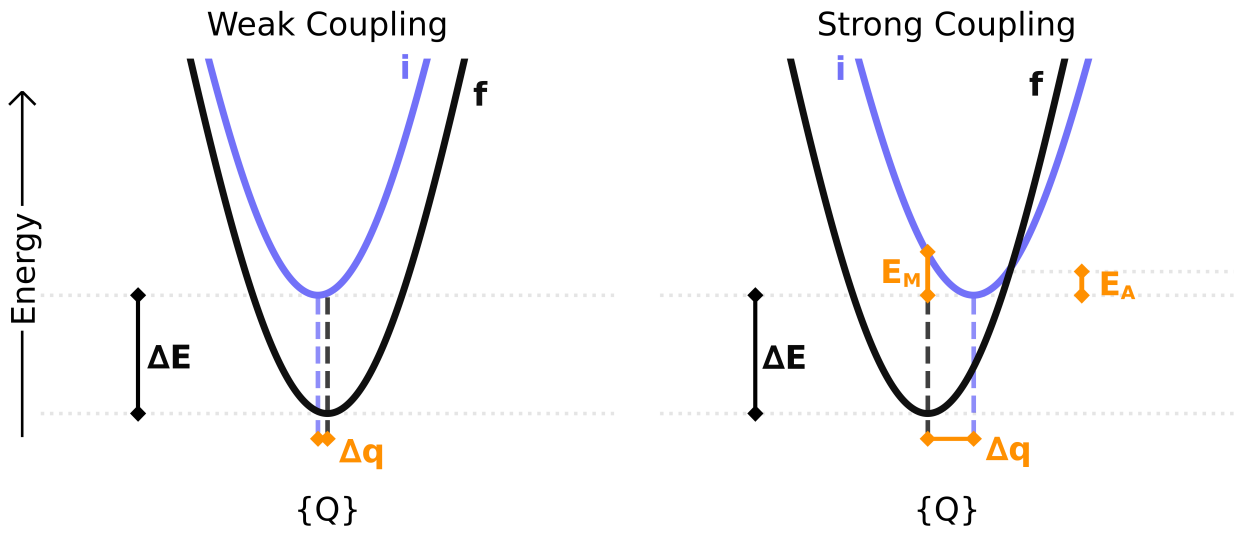

Figure 5.1: Diagrams representing two adiabatic potential energy surfaces as described by Englman & Jortner. In the Weak Coupling regime, there is a small difference in nuclear coordinate {Q} between initial (i, purple) and final (f, black) states, resulting in a negligibly small nuclear relaxation energy E_M between the two states. Conversely, in the Strong Coupling regime it can be seen that the large displacement in {Q} yields an appreciable nuclear relaxation energy, an appreciable value for E_M, and an energy gap between the initial state and the point of intersection between the two surfaces, E_A.

for the change in energy for switching from the initial and final geometries, similar to E_M.

$$k_{et} = \frac{2\pi}{\hbar} |H_{if}|^2 \frac{1}{\sqrt{4\pi\lambda k_B T}} \exp\left(-\frac{\Delta G^{\ddagger}}{k_B T}\right) \tag{5.4}$$

However, in both expressions it is more common to expand the E_A or $\Delta G^{\ddagger}$ terms using the relations in Equations 5.5 and 5.6, respectively. By doing so, W_c can be found from just ΔE and E_M, which are easy to find computationally, and k_{et} can be found from just ΔG° and λ, which again may be found computationally or even analytically.

$$E_A = \frac{(\Delta E - E_M)^2}{4E_M} \tag{5.5}$$

$$\Delta G^{\ddagger} = \frac{(\Delta G^{\circ} + \lambda)^2}{4\lambda} \tag{5.6}$$

These relationships both take advantage of the quadratic nature of the curves shown in Figure 5.1. In fact, both equations aim to estimate the intersection point of two energetic surfaces. It's noteworthy that despite having similarly defined parameters these equations may not appear mathematically equivalent. Without chemical intuition one may find this perplexing, particularly because diagrams that accompany these theories will often present both ΔE and ΔG_0 as positive values. Hidden in the context of Marcus theory is that these electron transfer reactions are generally exothermic, meaning ΔG_0 is inherently a negative value. Thus, these two formulations are practically equivalent, which has potentially led to confusion on how to apply them in practice.

A quick review of the literature on intersystem crossing reveals subtle inconsistencies in the utilization of Equation 5.3 in computational studies. For instance, a review by Penfold *et al.*[192] indicates the equivalent of E_A as $(\Delta E + \lambda)^2/4\lambda$, while a similar review by Marian reports $(\Delta E - \lambda)^2/4\lambda$.[190] The immediate discrepancy lies in the mix of notation between the theories of Englman & Jortner (with ΔE) and Marcus (with λ), leading to ambiguity in the addition/subtraction of λ. While it's understandable that these two remarkably similar notations might be combined to minimize redundancy, the lack of consistency can be challenging to decipher. Numerous works appear to use $\Delta E + \lambda$ while also having positive values for ΔE.[201–205] Interestingly, Schmidt *et al.* used $\Delta E + \lambda$ but also recognized that ΔE should be negative.[179] Other works maintain the "correct" positive sign for ΔE and then use $\Delta E - \lambda$ to solve for the isc rate constant,[206] yielding a result most true to the original theory.

The aim of this work is to illustrate and verify the utility of quantum chemical calculations toward estimating intersystem crossing rate constants, using the well-studied and relatively simple molecule nitrobenzene. This work will stick to the convention of Englman & Jortner, in some ways deviant from the recent literature, in the discussion of the energetics of nitrobenzene. While the introduction mostly focused on the limits of strong vibronic coupling and high temperature, the application of imposing no assumptions on temperature is also explored.

Nitrobenzene is a nice subject for this study since it is a relatively small aromatic molecule, it has been subject of both experimental and computational inquisition, and it undergoes intersystem crossing on ultrafast timescales.[125,207–212] Takezaki *et al.* (1998) observed that nitrobenzene undergoes intersystem crossing with a rate constant of 1.3-1.6 $\times$ 10^{11} s^{-1} (lifetime of approximately 6 ps).[208] These findings supported transient absorption measurements by Yip *et al.* that observed a $\leq$ 5 ps rise time of a triplet transient.[207] Further validation is provided by looking at similar molecules, such as 1-nitronapthalene and 1-nitropyrene, which also exhibit ultrafast intersystem crossing on the order of picoseconds.[129,130] Building upon the insights provided by other exhaustive computational studies on nitrobenzene excited states,[183,213,214] this work will attempt to use quantum chemical calculations to replicate measured intersystem crossing rate constants, with the hypothesis that they will also be on the order of picoseconds.

5.2 Methods

The Q-Chem 5.0 computational chemistry package was used for the entirety of this work.[96] Density functional theory was used for ground-state optimizations of nitrobenzene. Ground state geometry optimizations were performed with the hybrid functional of Purdue, Burke, and Enzehoff (PBE0)[98] and the people 6-311+G(d) basis set,[178] a combination which has worked well for nitroaromatics in previous works.[177,215] Excited-state calculations were performed with linear-response time-dependent density functional theory (TDDFT). With expected charge-transfer character in the excited states, calculations were done with the long-range corrected form of PBE0 (here referred to as LC-ωPBE0), which handles charge-transfer states better than its uncorrected counterpart.[216] For the sake of comparison to previous studies, both the aug-cc-pVDZ and 6-311++G(d,p) basis sets were used for excited state calculations.[178,217] Attempts were made to utilize the "state tracking" feature in Q-Chem during the optimization of the excited states, however, it was difficult to find convergence when states of the same transition character (i.e. two nπ^* states)

would become degenerate. Ultimately, the energy values used for calculating transition probabilities were pulled from energy surfaces calculated over a handful of interpolated coordinates.

5.3 Results and Discussion

5.3.1 Optimized geometries

For previously reported DFT (and ab initio) calculations in vacuo, the ground state (S_0) of nitrobenzene is planar with C_{2v} symmetry.[210,218] Since a solvation model was used in this work, symmetry was not restricted during geometry optimizations to allow for solvation effects. Solvation was approximated with the conductor-like polarized continuum model with ethanol as a solvent (ϵ = 24.5), since ethanol was a solvent used in experiments by Takezaki *et al.*[208] The planar symmetry of nitrobenzene is distorted when using the solvation model, resulting in an optimized geometry with broken symmetry.

The geometries of the excited states are less straightforward to determine. To aid in the interpretation of excited state optimizations, it is helpful to know the characteristics of each transition. Figure 5.2 shows the Natural Transition Orbitals (NTOs) for S_1 and the first five triplet states, T_1-T_5, at the reference point of the ground state geometry. The states S_1, T_3, and T_5 share $n\pi^*$ character, and the states T_1, T_2, and T_4 are all of $\pi\pi^*$ character, which is mostly in agreement to previous observations with B3LYP/aug-cc-pVDZ.[213] Referencing the states in the S_n/T_n notation can become ambiguous when discussing excited state geometry optimizations, because their energetic orderings can change at different molecular coordinates. To help prevent ambiguity, this work will use the notation shown in Table 5.1 to refer to the triplet excited states at geometries that deviate from the ground state, using the character of its NTO and the spin of the excited state. The number in front is the index for which that state appears energetically (at the ground state) within its own spin/character category.

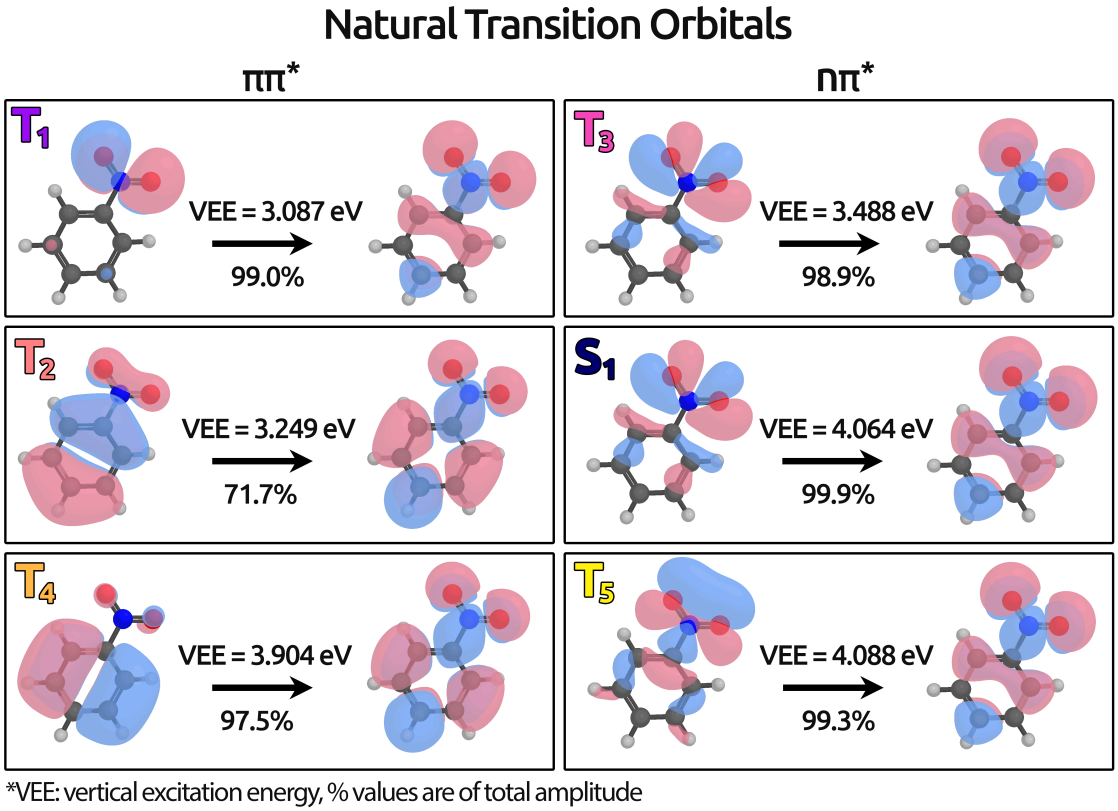

Figure 5.2: Natural transition orbitals of strongest amplitude for excited states in nitrobenzene as predicted by TD/LC-ωPBE0/aug-cc-pVDZ level of theory. The left column shows states that are of $\pi\pi^*$ transition character, and the right column shows states of nπ^* character. The vertical excitation energies of each state are provided along with the percentage of total amplitude of the illustrated transition toward each state.

Table 5.1: Notation used in this work for the excited states in nitrobenzene.

State @ S_0	Notation in this work
S_1	$1\,^1\mathrm{n}\pi^*$
T_1	$1\,^3\pi\pi^*$
T_2	$2\,^3\pi\pi^*$
T_3	$1\,^3\mathrm{n}\pi^*$
T_4	$3\,^3\pi\pi^*$
T_5	$2\,^3\mathrm{n}\pi^*$

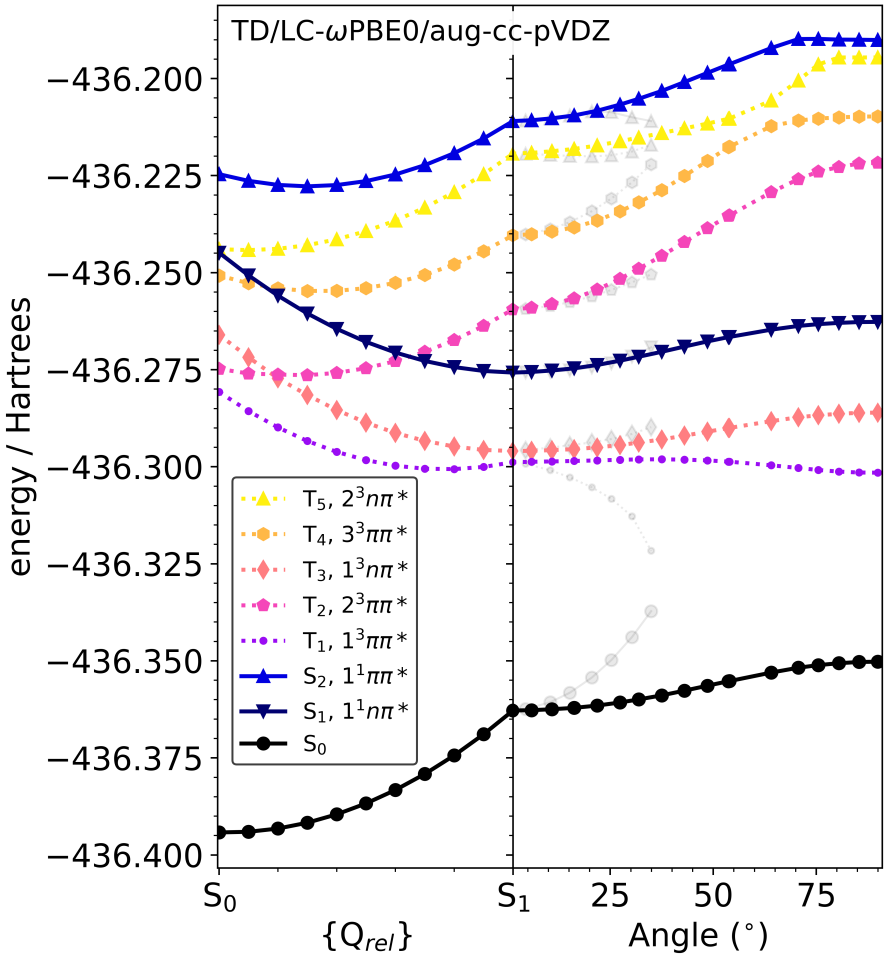

Figure 5.3: Total energy for singlet (S_0 = black, S_1 = navy blue, S_2 = blue) and triplet (T_1 = purple, T_2 = salmon, T_3 = pink, T_4 = light orange, T_5 = yellow) states in nitrobenzene within the optimization path from S_0 to S_1 (left plot) and at different -NO_2 torsion angles (full color) and -NO_2 bending angles (transparent traces).

Figure 5.3 shows the potential energy of the ground state and the first six excited states in nitrobenzene, along an interpolated coordinate between S_0 and S_1 (left panel) and along the -NO_2 torsion coordinate (right panel, color). States of the same character tend to follow the same trends: throughout this coordinate the energies of nπ^* states decrease and the energy of $\pi\pi^*$ states increase. The calculated excited state geometries are in good agreement with those calculated with varying levels of theory, which are nicely summarized in Giusanni & Worth.[214]

Importantly, this is a major difference from the observations by Quenneville *et al.*, who observed a conical intersection between S_0, S_1 and T_2 ($2\,^3\pi\pi^*$) at a combination of large torsion and bending angles. From the observations here, it appears that they did not account for the crossing of T_2 ($2\,^3\pi\pi^*$) and T_3 ($1\,^3n\pi^*$). Instead, the three-state conical intersection observed in that work is between S_0, S_1 ($1\,^1n\pi^*$) and T_3 ($1\,^3n\pi^*$). We have confirmed this with visualizations of the NTO's at the geometries provided in Quenneville *et al.* These differences have implications toward this work, as the driving force for such strong geometric deformations is said to be strong spin-orbit coupling at this intersection, driving intersystem crossing. Large deformations are not likely to play a role in the excited state dynamics of nitrobenzene, as suggested by the TDDFT calculations in this work and calculations done at higher levels of theory by Giussani & Worth.[214] Instead, the large deformations are likely only important toward photolytic degradation mechanisms,[214] although studies of nitrobenzene dynamics in the condensed phase suggest photolytic pathways are negligible.[212]

The surfaces in Figure 5.3 suggest that the crossing of S_1 ($1\,^1n\pi^*$) and T_2 ($2\,^3\pi\pi^*$) occurs within the S_1 relaxation coordinate, which is a potential answer for the short 5-6 ps lifetimes for S_1 reported in the literature. It is worth noting that more recent experiments suggest that the intersystem crossing lifetime could be sub-ps,[211] in which case it is even less likely that the molecule undergoes significant reconfiguration prior to crossing. Importantly, T_1 ($1\,^3n\pi^*$) and T_3 ($2\,^3n\pi^*$) are effectively nested with S_1 ($1\,^1n\pi^*$), implying that the strong vibronic coupling limit does not apply to these states, and Equation 5.3 is expected to perform poorly in predicting W_c for those states. With this in mind, the highest transition probability should be toward T_2 ($2\,^3\pi\pi^*$).

5.3.2 Estimated rate constants

The transition probabilities (shown as rate constants) of intersystem crossing were predicted with Equations 5.7 and 5.8 below. Equation 5.7 is equivalent to Equation 5.3 discussed in the introduction, with adapted notation to match the TDDFT calculations.

$$k_{isc} = \frac{2\pi}{\hbar} {H_{SO}}^2 \frac{1}{\sqrt{2\pi E_M k_B T}} \exp\left(-\frac{(\Delta E - E_M)^2}{4E_M k_B T}\right) \tag{5.7}$$

Englman & Jortner derived this expression to be used in the high temperature limit, as defined by $\beta\hbar\langle\omega\rangle \ll 1$, where $\beta = 1/(k_B T)$ and $\hbar\langle\omega\rangle$ is the mean vibrational frequency of the molecule expressed in energy units. From DFT calculations, $\langle\tilde{\nu}\rangle$ for nitrobenzene is ≈1260 cm^{-1}, meaning $\beta\hbar\langle\omega\rangle \approx 6$ at room temperature (300 K). Though room temperature is clearly not within the high temperature threshold, it is common to still use this expression even at relatively low temperatures.[179,219–224] Coincidentally, the low temperature limit ($\beta\hbar\langle\omega\rangle \gg 1$) also does not apply at room temperature, although it is arguably more applicable. Without imposing any temperature limits, the transition probability is said to depend on the effective temperature (Equation 5.8), which is expressed in energy units in Equation 5.9. At 300 K, $k_B T^* \approx 3\ k_B T$ using $\langle\tilde{\nu}\rangle$ = 1260 cm^{-1} .

$$k_{isc} = \frac{2\pi}{\hbar} {H_{SO}}^2 \frac{1}{\sqrt{2\pi E_M k_B T^*}} \exp\left(-\frac{(\Delta E - E_M)^2}{4E_M k_B T^*}\right) \tag{5.8}$$

$$k_B T^* = \frac{1}{2}\hbar\langle\omega\rangle \coth\left(\frac{\hbar\langle\omega\rangle}{2k_B T}\right) \tag{5.9}$$

The rate constants calculated with Equations 5.7 and 5.8 are shown in Table 5.2, along with the energy parameters obtained from TDDFT calculations. The largest rate constant, which is between S_1 and T_2, is two orders of magnitude smaller than the k ≈ 10^{11} s^{-1} target. Since the

Table 5.2: Spin-orbit coupling and calculated intersystem crossing rate constants (k_{isc}) for triplet states with S_1 in nitrobenzene predicted with the theory of Englman & Jortner, within the strong coupling approximation

Triplet State	ΔE **(eV) to** S_1	E_M **(eV) to** S_1	H_{SO} **(cm^{-1}) to** S_1	k_{isc} **to** S_1 **(s^{-1})**	
				Eq. 5.7	Eq. 5.8
T_1 ($1\,^3\pi\pi^*$)	0.6767	0.0385	79.8	4.8×10^{-32}	5.2×10^{-17}
T_2 ($2\,^3\pi\pi^*$)	0.0136	0.4147	13.8	2.5×10^{9}	2.1×10^{9}
T_3 ($1\,^3n\pi^*$)	0.5498	<0.0001	1.19	-	-
T_4 ($3\,^3\pi\pi^*$)	-0.5724	0.4147	9.80	7.4×10^{0}	1.1×10^{4}
T_5 ($2\,^3n\pi^*$)	-0.8649	0.8404	50.3	2.4×10^{-3}	1.7×10^{2}

rate constants for other pathways are negligible, summation of all k values (to the effective total isc rate constant) does not improve agreement in any meaningful way.

There is a minimal difference between the S_1-to-T_2 k_{isc} values with and without the high temperature limit simplification. The other rate constants all see increased orders of magnitude. Considering that the pre-exponential factor in Equation 5.8 is only 1.75 times larger than in Equation 5.9 (for nitrobenzene at 300 K), the effect of changing the exponential is clearly more significant. Based on this, it seems that using the high temperature approximation may produce reasonable values in the condition $E_M \gg \Delta E$.

Recent work by Shizu & Kaji revisited the approach toward estimating rate constants of different intramolecular excited-state processes, ultimately determining that their new method yields identical results for intersystem crossing to the approach of Englman & Jortner.[189] As part of their findings they acknowledged that the Gaussian distribution in the density of states term underestimates rate constants when compared to experimental findings for benzophenone, as it does in this work for nitrobenzene. Instead, the authors propose the use of a Lorentzian distribution for the density of states, which in their case better reproduced experimental observations. With a Lorentzian distribution, the transition probability can be found using Equation 5.10.

$$k_{isc} = \frac{2\pi}{\hbar} {H_{SO}}^2 \frac{1}{\pi} \frac{\gamma}{\Delta E^2 + \gamma^2} \tag{5.10}$$

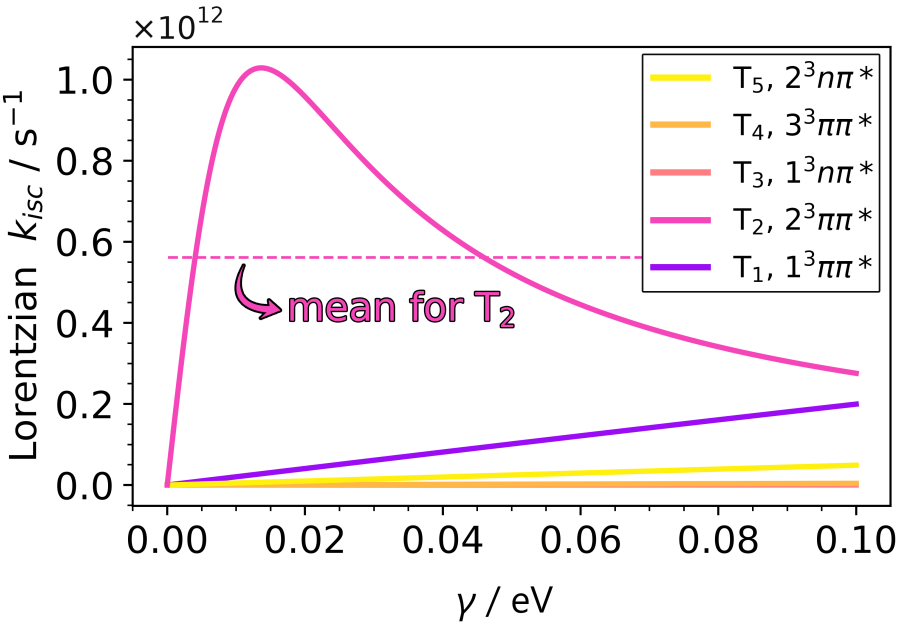

Figure 5.4: Transition probabilities (expressed as k_{isc}) for the intersystem crossing, as predicted by a Lorentzian distribution, between S_1 and the five lowest triplet states in nitrobenzene.

The issue with using the Lorentzian distribution is that the scaling parameter γ cannot be obtained from electronic structure calculations and must be approximated or determined empirically. Shizu & Kaji empirically determined γ for benzophenone from the full-width at half-maximum (fwhm) of its fluorescence/phosphorescence spectra.[189] In a different study on nitrophenols, the Lorentzian method was used to estimate the transition probabilities in 2-nitrophenol and 4-nitrophenol, producing values as high as 10^{11} s^{-1}.[180] The results for the nitrophenols suggest that γ = 0.04 eV was used, although it was not stated explicitly.

Figure 5.4 shows the dependence of k_{isc} for each triplet state as calculated by Equation 5.10 over a range of γ values, using the ΔE and H_{SO} values in Table 5.2. The states with relatively high (in magnitude) ΔE values, i.e. all but T_2 ($2\,^3\pi\pi^*$), are effectively linear within the range of γ shown, with relatively low transition probabilities. Consequently, the dominant transition is S_1-to-T_2 for the entire range. Although the choice of γ does influence the transition probability, the variance is roughly limited to being within one order of magnitude.

Table 5.3: Averaged transition probabilities $\langle k_{isc} \rangle$ for singlet to triplet intersystem crossing in nitrobenzene as predicted using a Lorentzian distribution over a γ = 0-0.136 eV range.

Triplet State	ΔE **(eV) from** S_1	H_{SO} **(cm**$^{-1}$**) with** S_1	$\langle k_{isc} \rangle$ **(s**$^{-1}$**) from** S_1
T_1 ($1\,^3\pi\pi^*$)	0.6767	79.8	1.4×10^{11}
T_2 ($2\,^3\pi\pi^*$)	0.0136	13.8	4.7×10^{11}
T_3 ($1\,^3n\pi^*$)	0.5498	1.19	4.6×10^{7}
T_4 ($3\,^3\pi\pi^*$)	-0.5724	9.80	2.9×10^{9}
T_5 ($2\,^3n\pi^*$)	-0.8649	50.3	3.3×10^{10}

H_{SO} was calculated at the ground state geometry.

The averaged values of k_{isc} (denoted as $\langle k_{isc} \rangle$) over the γ = 0-0.136 eV range are shown in Table 5.3. The upper limit of the range corresponds to $\sim$10 $\Delta E_{S_1-T_2}$, which between 300 and 400 nm corresponds to a fwhm of 10-20 nm. This fwhm is rather narrow for typical phosphorescence spectra in organic molecules, but it does match relatively well with some transient absorption bands reported for nitrobenzene.[212] Even so, extending the range to higher energies would have minimal impact on the magnitude of $\langle k_{isc} \rangle$, and would actually bring it closer toward the 10^{11} s^{-1} experimental reference. The mean value of k_{isc} in this range for T_2 is 5.6 $\times$ 10^{11} s^{-1}, which corresponds to a lifetime of $\sim$1.7 ps. This value is in much better agreement to the ultrafast intersystem crossing lifetimes reported in the literature than in the Gaussian case. In the case of nitrobenzene, the use of the Lorentzian proposed by Shizu & Kaji is justified. Expectedly, the Lorentzian method may over-predict the transition probabilities between states with relatively large energy gaps. Given the arbitrary nature of the γ scaling parameter, it is suggested here that reporting the average k_{isc} value (over a reported γ range) seems like a reasonable substitute in the absence of empirical information about a molecule, though caution should to be taken when interpreting results between states with large energy gaps.

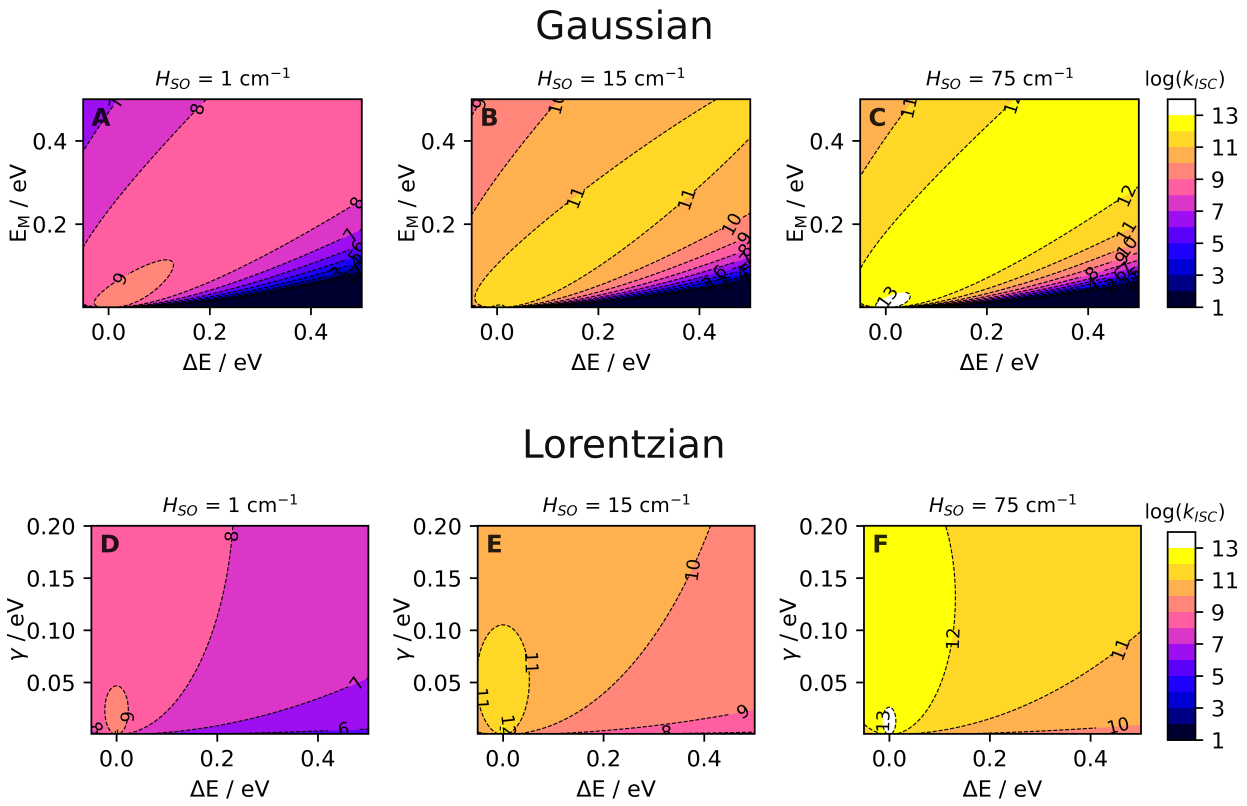

Figure 5.5: Psuedocolor/contour plots for log(k_{isc}) values produced by the Gaussian (top) and Lorentzian (bottom) distributions in the k_{isc} expression over ranges of energy values.

5.3.3 Theoretical Overview

Figure 5.5 presents the array of log(k_{isc}) values over typical ranges of the ΔE, E_M, and γ. Three different H_{SO} scenarios are presented to illustrate weak, intermediate, and strong spin-orbit coupling. Each color represents a different order of magnitude for k_{isc}, as is also indicated by the contour lines. In the Gaussian scenario, corresponding to Equation 5.7, the highest k_{isc} values roughly follow a one-to-one line between ΔE and E_M. This is expected, as the exponential part of Equation 5.7 is only significant in the limit that the two are similar to each other. The combination of high ΔE and low E_M yields especially low k_{isc}, which is expected since this scenario falls into the weak vibronic coupling regime presented by Englman & Jortner, where Equation 5.7 is not applicable.

From this point of view, it becomes clear that the Gaussian distribution has strict requirements to produce ultrafast k_{isc} values. The reason that this framework may not accurately describe the nature of nitroaromatics is likely due to the main assumption used to develop the theory: it is designed to describe transitions between two states with Parabolic-shaped energy surfaces. With the numerous degrees of freedom present in nitroaromatics, the most important of which tend to be C-N bond length, -NO_2 rotation, -NO_2 pyramidalization, and the ONO bond angles, the energy surfaces of these molecules tend to be more complex than simple Gaussian energy wells. This could be a justification toward adopting a Lorentzian form for the vibrational component of Equation 5.2, which allows for ΔE to be the major driving force behind k_{isc}. Combined with the relatively large spin-orbit couplings seen in nitroaromatics, Equation 5.10 is able to reproduce values more akin to the experimentally measured intersystem crossing rate constants. Future studies could potentially evaluate and present both, seeing as they require the same quantum chemical calculations, particularly for molecules that undergo large nuclear rearrangements upon photoexcitation.

5.4 Implications for Calculations in Chapter 4

The rate constants calculated in Chapter 4 were done with the Marcus theory form of the transition probability expression, meaning ΔE + λ was used (Eq. 4.2). This choice was made on account of the fact that this form is presented in heavily cited reviews. In light of the previous discussions, it seems beneficial to revisit the work in Chapter 4. In the case of 4-nitrocatechol, switching to the Englman & Jortner expression (Eq. 5.7) doesn't change the overall picture, where the Gaussian dependence results in relatively small k_{isc}. Table 5.4 shows the kisc values predicted with the Gaussian expressions of Marcus (Eq. 4.2) and Englman & Jortner (Eq. 5.7), and by the Lorentzian form (Eq. 5.10). The isc transition to T_1 is ignored here since S_1 is effectively nested with T_1, meaning the strong vibronic coupling limit of Englman & Jortner does not apply. What

Table 5.4: Values for k_{isc} in 4-nitrocatechol based on theoretical calculations in Chapter 4

Triplet State	H_{SO} **(cm^{-1}) with S$_1$**		k_{isc} **(s^{-1}) from S$_1$**	
		Eq. 4.1-4.2	Eq. 5.7	Eq. 5.10
T_2	0.346	1.36×10^2	4.66×10^5	5.04×10^6
T_3	15.3	4.53×10^7	7.36×10^3	9.61×10^9

was the most probable transition, the isc from S_1 to T_3, is unfavored by the Eq. 5.7 expression, likely due to ΔE being negative (the T_3 minimum of 4-nitrocatechol is higher in energy than the S_1 minimum). The Lorentzian expression produces the largest kisc constant ($\sim 10^{10}$ s^{-1}), which is a lifetime of $\sim$100 ps. This lifetime is more in line with the experimental observations that suggested isc on the order of 10-100 ps in 2-propanol.

It is unclear if it is fair to say that the typical Englman & Jortner theory fails to describe the excited state dynamics of 4-nitrocatechol. While the Lorentzian distribution does replicate the ultrafast isc seemingly observed in 4-nitrocatechol, it relies on guessing the scaling parameter γ. It is possible that higher levels of theory (TDA/PBE0/6-311+G(d) was used) could result in more accurate estimations of the excited state energies. The Tamm-Dancoff Approximation (TDA) was used due to the presence of twisted charge-transfer character in the 4-nitrocatechol excited states. Similarly to the results for nitrobenzene shown here, the S_1 to T_n crossings occur without major -NO_2 rotation and thus it may have been unnecessary to have used the approximation when isc may occur without such large molecular deformations.

5.5 Conclusions

The original theory of Englman & Jortner was compared to more recent publications, highlighting discrepancies in the utilization of theoretical frameworks toward the estimation of intersystem crossing transition probabilities. This work suggests that deviating from sharing notation with electron transfer theory may help prevent misuse of the Englman & Jortner framework. Also

acknowledged here is the benefit of using a Lorentzian distribution, particularly in molecules which are expected to undergo intersystem crossing on picosecond timescales. It is acknowledged that the accuracy of this solution is dependent on strong spin-orbit coupling and a relatively low energy gap between the singlet and triplet state. Accordingly, the reported ultrafast S_1-to-T_2 intersystem crossing in nitrobenzene is successfully reproduced using energetic values obtained from TDDFT calculations when a Lorentzian distribution is used, and the use of Englman & Jortner theory seems to break down when describing ultrafast isc processes.

Chapter 6

Isomeric Identification of the Nitroindole Chromophore in Indole + NO_3 Organic Aerosol

Oxidation of indole by nitrate radical (NO_3) was previously proposed to form nitroindole, largely responsible for the brown color of indole secondary organic aerosol (SOA). As there are seven known nitroindole isomers, we used chromatographic separation to show that a single nitroindole isomer is produced in the indole + NO_3 reaction, and definitively assigned it to 3-nitroindole by comparison with chromatograms of nitroindole standards. Mass spectra of aerosolized 3-nitroindole particles were recorded with an aerosol mass spectrometer (AMS), and directly compared to mass spectra of SOA from a smog chamber oxidation of indole by NO_3 in order to help identify peaks unique to nitroindole (*m/z* 162, 132, and 116). Quantum chemical calculations were done to determine the energetics of hypothesized indole + NO_3 intermediates and products. The combination of these data suggests a mechanism where a hydrogen atom is first abstracted from the N-H bond in indole, followed by isomerization to a carbon-centered radical in 3-position, and followed by addition of NO_2. Alternative mechanisms involving a direct abstraction of an H-atom

from a C-H bond or an NO_3 addition to the ring, followed by NO_2 addition and elimination of HNO_3 are predicted to be energetically unfavorable.

6.1 Background

The importance of secondary organic aerosol (SOA) in the atmosphere is well established, with many studies highlighting the role of SOA in radiative forcing and cloud formation.[52,225–233] Various atmospheric oxidants contribute toward atmospheric SOA formation from volatile organic compounds (VOCs), however, the nitrate radical (NO_3) is unique in that its strongest contribution occurs during nighttime.[234] Nitrate radical can react with both biogenic and anthropogenic VOCs to produce light-absorbing aerosol.[40,235,236] Recent studies have examined the formation of SOA from indole, a VOC emitted by plants, revealing strong light absorption by indole SOA formed in the presence of nitrogen oxides.[237,238]

The nitrate radical reacts with monoterpenes and aromatic compounds by different mechanisms, resulting in nitric acid esters (R-ONO_2) for the former and nitroaromatics (Ar-NO_2) for the latter.[148,236,239,240] As an aromatic molecule, indole has a higher likelihood of forming aromatic nitro compounds (Ar-NO_2), which are known to be strong chromophores.[241] Accordingly, the dominant chromophore in indole/NO_3 SOA was assigned to be a nitroindole,[237] though definitive assignment of the specific isomer was not possible. More recent work by Jiang and coworkers proposed that the dominant isomer is 3-nitroindole, though no comparisons were drawn between the SOA and an analytical reference.[238] From their proposed mechanism, it is assumed that OH and NO_3 act similarly by abstracting a hydrogen from indole, followed by addition of NO_2 to the resulting radical. The goals of this work are to better constrain the mechanism of indole oxidation and to confirm the identity of the nitroindole isomer formed in the indole + NO_3 reaction with a combination of experimental and quantum chemical methods.

6.2 Methods

6.2.1 Materials and Equipment

Reference standards for several nitroindole isomers were prepared in 2-propanol (MilliporeSigma, ACS grade) with mass concentrations around 0.2 mg/mL. The nitroindoles investigated were 3-nitroindole (BLD Pharm, 98%), 4-nitroindole, 5-nitroindole, 6-nitroindole, and 7-nitroindole (each Fisher Scientific, >98%). UV/Vis absorption spectra were recorded over 200-700 nm range with a Shimadzu UV-2450 spectrophotometer. Separation of compounds in the indole + NO_3 SOA was done with ultra-performance liquid chromatography (UPLC) via an ACQUITY HSS T3 C_{18} column (100 Å, 1.8 µm, 2.1 mm $\times$ 100 mm). A Vanquish Horizon photodiode array spectrophotometer (wavelength scan range of 190-680 nm) was used to compare absorption spectra of separated indole + NO_3 SOA chromophores to those of reference standards. The formula of the main chromophore in the SOA was verified to be $C_8H_6N_2O_2$ via a Q Exactive Plus high-resolution mass spectrometer, consistent with its previous assignment to a nitroindole isomer.

6.2.2 Experimental Methods

Indole/NO_3 SOA was generated in a 5 m^3 smog chamber in batch mode similar to previous work.[237] Nitrate radical was generated by the simultaneous injection of 100 ppb of NO and a slight excess of O_3 ($\sim$300 ppb). Under these conditions, NO is converted into NO_2 and subsequently NO_3. Since indole exhibits nearly 10^6 times higher reactivity toward NO_3 than O_3,[242] reactions of indole with NO_3 are favored, even with the slight excess of O_3. A 200 µL aliquot of a 100 mg/mL solution of indole in methanol was then gently evaporated into a 2 SLM flow of purge air and passed through a heated inlet into the chamber, yielding an indole mixing ratio around 100 ppb. The SOA was collected after 3 hours of reaction by pulling air from the chamber through a 0.2 µm PTFE filter (Merck Millipore, 47 mm diameter).

For experiments with a time-of-flight aerosol mass spectrometer (ToF-AMS , Aerodyne) the mass loadings of all reactants were lowered, to around 30 ppb of indole, 80 ppb of NO, and 200 ppb of O_3. For sampling into the AMS, the chamber was connected to a Y-shaped fitting on the inlet of the AMS. A flow of purge air was attached to the other side of the Y-fitting to further dilute the samples air by a factor of 10. Standard 3-nitroindole particles were generated by aerosolizing a 0.10 mg/mL solution of 3-nitroindole in methanol with a TSI constant output atomizer at $\sim$ 2 SLM, sending the flow through a series of adsorbent driers to remove excess methanol, and injecting it into a 130 L Teflon bag. The ToF-AMS sampled directly from the bag, both with and without the 10-fold dilution. A scanning mobility particle sizer (TSI 3080) and condensation particle counter (TSI 3775) were used to measure size distributions of both the aerosolized 3-nitroindole particles and of the SOA in the smog chamber. AMS data analysis was done with Squirrel 1.66E and Pika 1.26E.

6.2.3 Computational Methods

Electronic structure calculations were done to provide insight into the energetics of a handful of potential indole + NO_3 reaction mechanisms. The Q-Chem 6.1 computational chemistry package was used for the entirety of this work.[96] Density functional theory (DFT) calculations were done with the PBE0 hybrid functional,[98] which has previously been used to estimate bond dissociation energies in other nitroaromatics with absolute errors as low as 1 kcal/mol.[243] For structures more critical to the hypothesized reaction pathway, second-order Møller-Plesset perturbation theory (MP2) was also used to reoptimize structures. The 6-311++G(d,p) basis set was used for all calculations,[178] employing the extra diffuse functions and polarization functions in an attempt to capture the effects of the unpaired electrons in the oxidations (NO_2 and NO_3) and the intermediates.

Harmonic vibrational frequency calculations were done with optimized geometries. The presence of an imaginary frequency was used as an indicator of potential transition state struc-

tures. Thermochemistry data were derived from the frequency calculations using the standard formulas implemented in Q-Chem. These data were calculated in standard conditions, and no scaling factors or other corrections were made to the resulting values. References to previous calculations for indole,[244] and to experimental measurements in pyrrole (a substructural component of indole) were made address the accuracy of these theoretical findings.[245]

6.3 Results and Discussion

6.3.1 UV/Vis Analysis

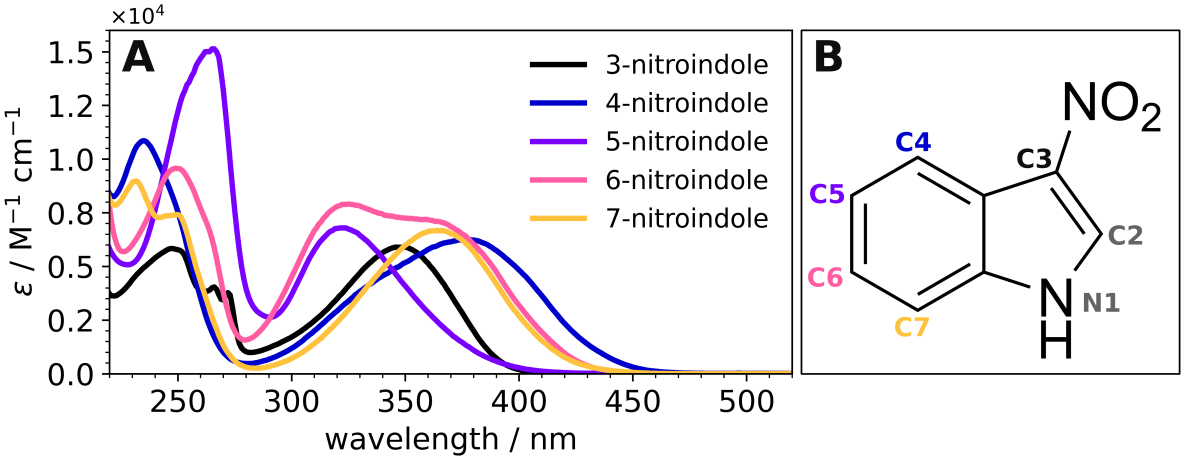

Figure 6.1: (A) Molar absorption coefficient spectra of the 3-, 4-, 5-, 6-, and 7-nitroindole isomers in 2-propanol. (B) Structure of 3-nitroindole, with numeric labels for the other positions (P) of the indole backbone.

The UV/vis absorption spectra of each nitroindole isomer were measured and scaled by their concentrations in 2-propanol to produce the molar absorption coefficient in Figure 6.1A. The structure of 3-nitroindole and labels for other isomeric positions are provided in Figure 6.1B. Most isomers exhibit one broadly absorbing peak in the near-UV (300-400 nm) range, although 6-nitroindole has two maxima in this range. The absorption spectrum for 4-nitroindole extends

furthest into the visible range. Absorption spectra of 3-nitroindole and 5-nitroindole are largely confined to the near-UV range, with peaks located at 349 nm and 322 nm, respectively.

6.3.2 Chromatography and HRMS

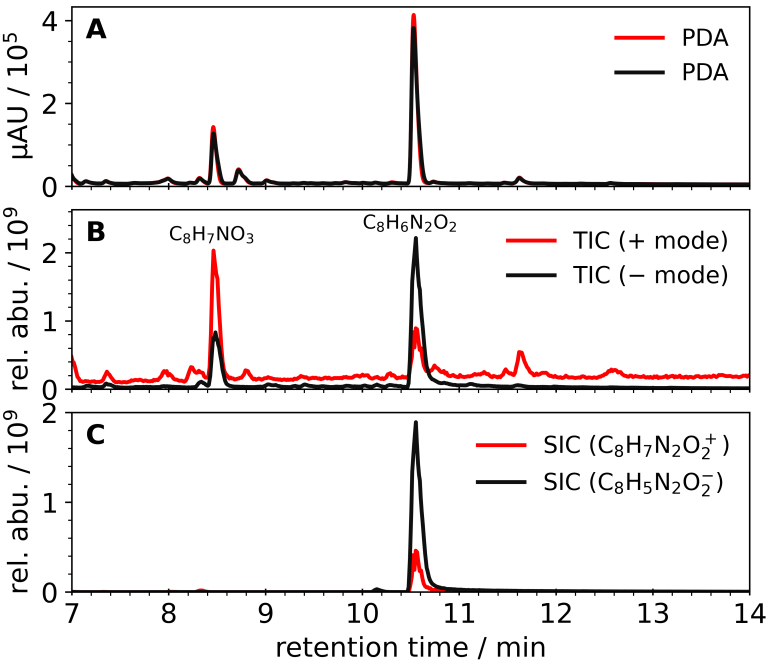

Figure 6.2: PDA (panel A), total ion current (TIC, panel B), and selected ion current (SIC, panel C) chromatograms for indole + NO_3 SOA, run in electrospray ionization positive mode (red) and negative mode (black).

The PDA chromatograms for the indole + NO_3 SOA sample reveal a handful of light-absorbing species eluting at various times (Fig. 6.2), in good agreement with previous findings for this type of SOA.[237] The major chromophore eluting at 10.5 min is detectable at *m/z* 161.0356 ($C_8H_5N_2O_2^-$) in negative ion mode and *m/z* 163.0500 ($C_8H_7N_2O_2^+$) in positive ion mode. The $C_8H_6N_2O_2$ formula of the neutral species is consistent with its previous assignment to a nitroindole isomer. The selected ion chromatograms for these ions (Fig. 6.2) produce a single dominant peak, with other peaks being more than an order of magnitude smaller, suggesting that a single isomer of nitroindole is preferentially formed. This isomer can be unambiguously identified to 3-nitroindole

by matching both the PDA retention times (Fig. 6.3A-B) and the PDA UV/Vis absorption spectra (Fig. 6.3G-H).

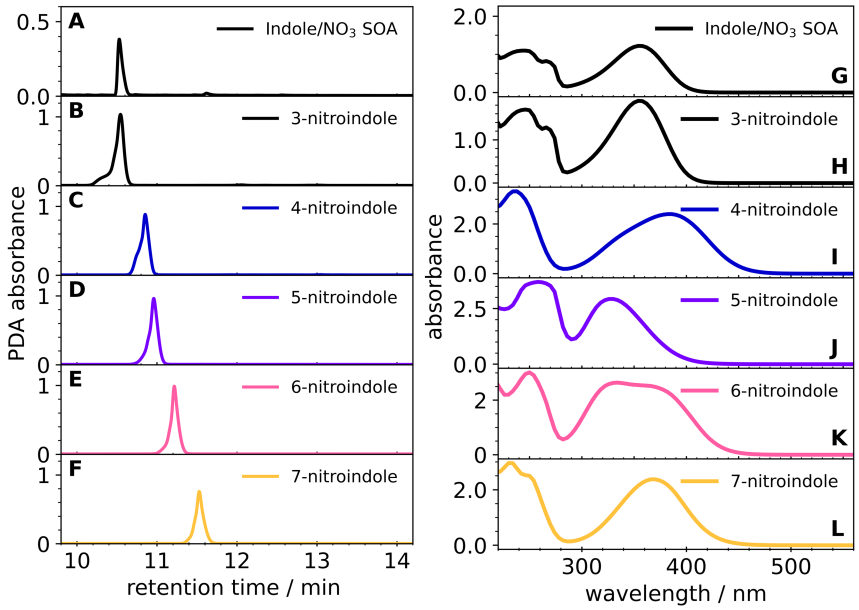

Figure 6.3: Photodiode array detector chromatograms for indole + NO_3 SOA and five isomeric nitroindole standards (A-F) and the absorption spectra at the peak of each chromatogram (G-L). The dashed lines in G-L are absorption spectra collected in in 2-propanol with the UV/Vis spectrophotometer.

The absorption spectra had slight differences between the measurements taken in different solvents, with the spectra recorded in the UPLC mobile phase (ACN and H_2O) typically exhibiting a redshift in the visible region compared to spectra recorded in 2-propanol (Fig. 6.4). This could be indicative that the lower lying excited singlet states are more polar compared to their ground states. The effects of changing solvent are less obvious for higher excited states since the resolution for peaks below 300 nm is inferior for the PDA in the UPLC system.

It is clear from the combination of these results that 3-nitroindole isomer is the dominant, if not the only, isomer which is formed prior to SOA collection. Although 2-nitroindole was not commercially available for testing, the exact match of 3-nitroindole toward the SOA chromophore at all three of the 250 nm, 270 nm, and 354 nm peaks is unlikely to be mirrored by 2-nitroindole in view of the large differences between absorption spectra of nitroindole isomers.

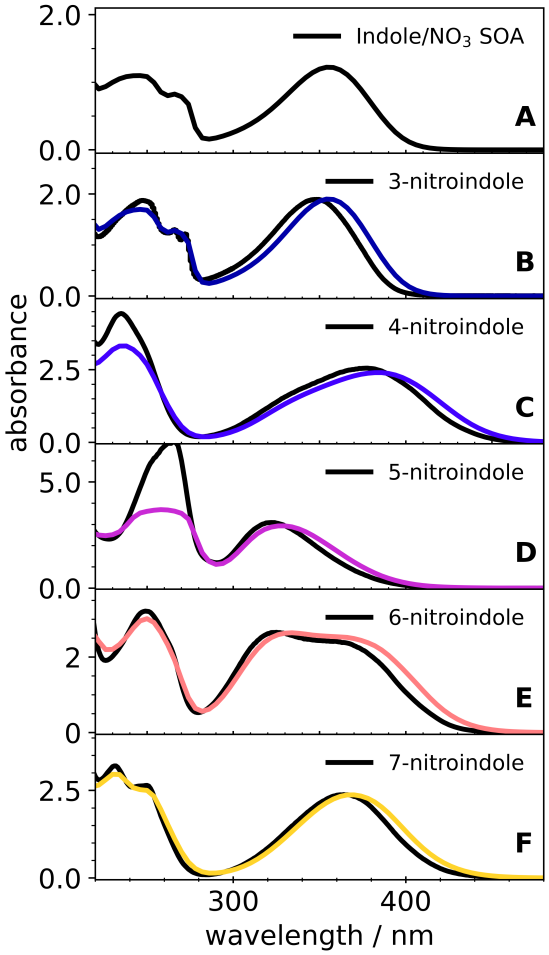

Figure 6.4: UV/Vis absorption spectra for each nitroindole isomer evaluated in this work. Small spectral shifts are observed relative to the peak wavelengths in the UPLC-PDA measurements, likely due to the different solvent (water-acetonitrile mixture at pH = 3). Colored traces were measured with the PDA, and the black traces were recorded with the bench-top UV/Vis.

6.3.3 Aerosol Mass Spectrometry

Figure 6.5 shows the unit-mass resolution ToF-AMS spectra for indole + NO_3 SOA and the 3-nitroindole standard. There is a striking resemblance between the fragmentation patterns of the 3-nitroindole standard and the SOA. The overwhelming similarities between the AMS spectra of the standard and of the SOA are indicative that the indole/NO_3 is predominantly composed of nitroindole.

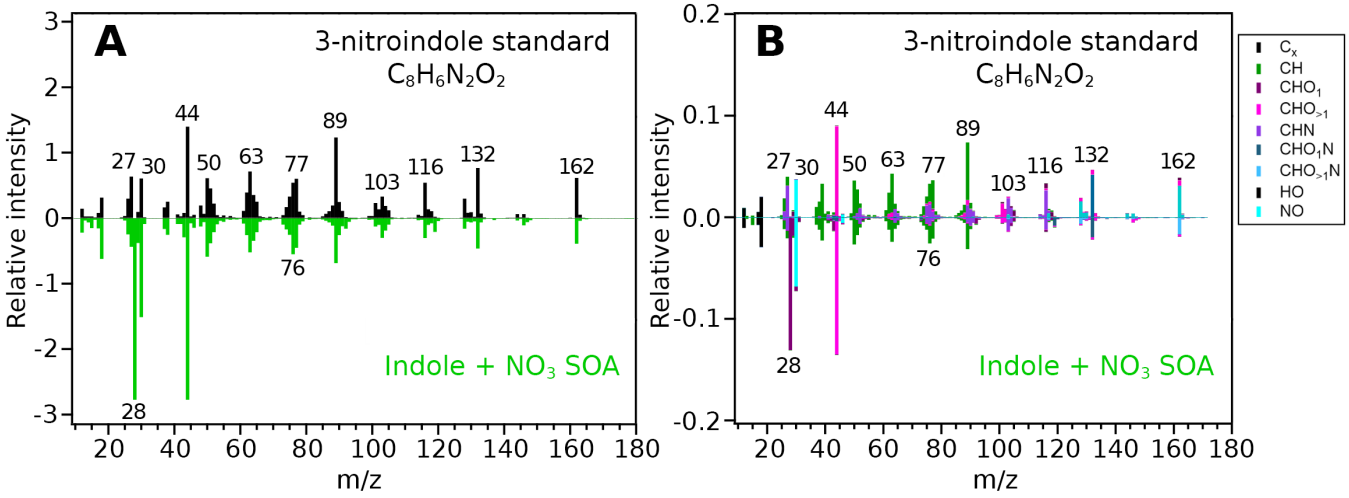

Figure 6.5: Unit mass resolution ToF-AMS spectra of aerosolized 3-nitroindole particles (top) and indole + NO_3 SOA (bottom), each measured with two different levels of dilution flow.

Proposed assignments to the major fragments observed in the nitroindole standard AMS spectrum are presented in Table 6.1. The peak observed at *m/z* 162 corresponds to 3-nitroindole radical cation. The peaks and *m/z* 132 and 116 correspond to loss of NO and NO_2, respectively, and peaks at lower *m/z* values are due to more extensive ion fragmentation. Given the strong similarities in ToF-AMS spectra of 3-nitroindole and indole + NO_3 SOA, the dominant ions (*m/z* 162, 132, and 116) can potentially be used to identify nitroindole in ambient samples. It should be noted that the electron impact ionization (the type of ionization used in AMS) produces similar ion fragmentation patterns for isomers of nitroindole, so ToF-AMS would detect a collection of all of the isomers.[246]

Table 6.1: Observed ions with proposed formulas and fragmentation schemes for aerosolized 3-nitroindole particles measured with AMS

m/z	Formula	Fragmentation Scheme
162	$C_8H_6N_2O_2$+	M+
132	C_8H_6NO+	[M-NO]+
116	C_8H_6N+	[M-NO_2]+
103	C_7H_5N+	[M-NO_2-CH]+
89	C_7H_5+	[M-NO_2-CH-N]+

6.3.4 Potential Indole + NO_3 Reaction Mechanisms

The net reaction to convert indole into nitroindole is likely to be described as a reaction of indole, NO_3, and NO_2 to yield nitroindole and HNO_3 in the gas phase. Jiang *et al.*[238] proposed that the mechanism involves a two-step process, in which the nitrate radical first abstracts a hydrogen from a C-H bond in indole to produce an indole radical and nitric acid (R6.1). The carbon-centered indole radical can then undergo a recombination with an NO_2 radical to form nitroindole (R6.2). The conditions in the current work would allow for the presence of NO_2 through incomplete NO_2 $\rightarrow NO_3$ conversion by O_3.

$$C_8H_7N + NO_3 \rightarrow C_8H_6N \text{ (indole radical)} + HNO_3 \quad \text{(R6.1)}$$

$$C_8H_6N + NO_2 \rightarrow C_8H_6N_2O_2 \text{ (nitroindole)} \quad \text{(R6.2)}$$

The hydrogen abstraction reaction R6.1 should proceed at the position of the weakest bond in indole. Jiang *et al.*[238] assumed that H-atom in P3 is the one that is being abstracted, which is a reasonable guess. To our knowledge, no measurements of bond dissociation energies (BDEs) have been reported for indole, however, theoretical calculations have estimated the BDE of each of its C-H bond and the N-H bond. These calculations, done with B3LYP/6-31G(d), suggest that the C-H bonds on the benzene ring of indole are weaker (111.1-111.5 kcal/mol) compared to the pyrrole ring (117.5 kcal/mol at P2, 118.0 kcal/mol at P3).[244] It is also worth noting that the N-H bond is predicted to be much weaker (86.9 kcal/mol),[244] which could indicate that hydrogen abstraction could occur from the N-H bond, as opposed to the C-H bond. Studies of the reaction between NO_3 and benzene have shown that the hydrogens in benzene are resistant toward hydrogen abstraction,[247,248] and this characteristic likely translates to indole as well.

As an indirect confirmation of the hypothesis of the hydrogen abstraction by NO_3 at the nitrogen position, such a mechanism was proposed to occur in pyrrole by Mayorga *et al.*[249] Importantly, the resulting nitrogen-centered radical is stabilized by resonance, which shifts the free electron to form a carbon-centered radical at P3. Such a process could reasonably occur on the

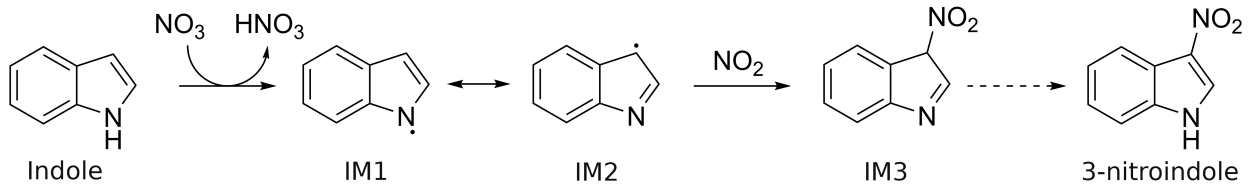

Figure 6.6: Proposed hydrogen abstraction mechanism for the formation of 3-nitroindole from the reaction of indole and NO_3.

pyrrole ring of indole, as is shown in Figure 6.6. The resonance does not readily extend to the more stable benzene ring in indole, leading to the dominant formation of 3-nitroindole in indole oxidation by NO_3. The most uncertain part of this mechanism is the last step, in which the which was regarded to be a hydrogen shift in pyrrole.[249] Given the planar structure of indole, subsequent reactions are likely required to remove the hydrogen from P3 in intermediate 3 (IM3) and add a hydrogen back to the nitrogen in the 1 position. This could require collisions with other molecules or proceed by tunneling. The mechanism of this last step was not investigated in this work.

We also considered an alternative mechanism, in which the NO_3 attaches to the closed-shell indole, followed by addition of NO_2 and elimination of HNO_3. A computational study by Li *et al.*[250] of the reaction of indole with acetonitrile (CH_2CN) and trifluoromethyl (CF_3) radicals found that these radicals preferentially attach to P2.[250] It should be noted that their study was approaching this problem from the perspective of synthetic organic chemistry, with an emphasis on these reactions as they might occur in a solvent. It is perhaps for that reason that radical reactions with the N-H bond were ignored in that work. While the insights regarding the energetics of radical addition brought that study are useful (they did provide results for the gas phase), the subsequent reaction steps (namely deprotonation) outlined in that work are likely to be less applicable to the gas phase setting of this indole + NO_3 organic aerosol formation.

6.3.5 Computational Results for Hydrogen Abstraction

The thermochemistry data resulting from the electronic structure calculations of the resulting products from hydrogen abstraction at each position are provided in Table 6.2. DFT at the PBE0/6-311++G(d,p) level was used for all potentially abstractable hydrogen atoms, and MP2/6-311++G(d,p) was used only for abstraction at P1, P2, and P3 to minimize computational expense. The PBE0/6-311++G(d,p) calculations seemed to be fairly accurate, as the estimated BDEs were similar to those calculated in previous studies and comparable to those measured in pyrrole. The initial step (Reaction 6.1) is energetically uphill for H abstraction from all C-H bonds, and slightly more so for the C-H bonds in the 2 and 3 positions (P2 and P3). Importantly, only the abstraction from the N-H bond is predicted to be exergonic.

Table 6.2: Thermochemistry data at the PBE0/6-311++G(d,p) and [MP2/6-311++G(d,p)] levels for the hydrogen abstraction reaction

Reaction Site	$\Delta E + ZPE$ **(kcal/mol)**	ΔH **(kcal/mol)**	ΔG **(kcal/mol)**
2	14.8 [18.9]	16.8 [26.4]	16.5 [26.5]
3	15.5 [21.5]	17.7 [29.5]	17.7 [29.9]
4	8.45	10.6	10.5
5	8.41	10.4	10.3
6	8.37	10.4	10.4
7	8.79	11.0	10.9
N*	-10.6 [-6.11]	-9.28 [-2.79]	-9.25 [-2.53]

*These data are for the reaction producing the IM1 structure, not the minimal energy structure IM2

A stepwise presentation of the reaction energetics for the indole + NO_3 + NO_2 pathway for hydrogen abstraction from P1 is presented in Figure 6.7. All energy values correspond to the minimized structures, with exception to IM1 which was approximated by simply removing the P1 hydrogen from the minimized indole structure. Optimization of IM1 resulted in IM2, consistent with lower energy of the latter. For the hydrogen abstraction reaction, both intermediates IM1 and IM2 result from abstraction from P1 are both energetically favorable, with the carbon-centered

radical form being the most stable. The spin density is shown to highlight the shifting of the unpaired electron to be predominantly around P3 in the IM2 structure.

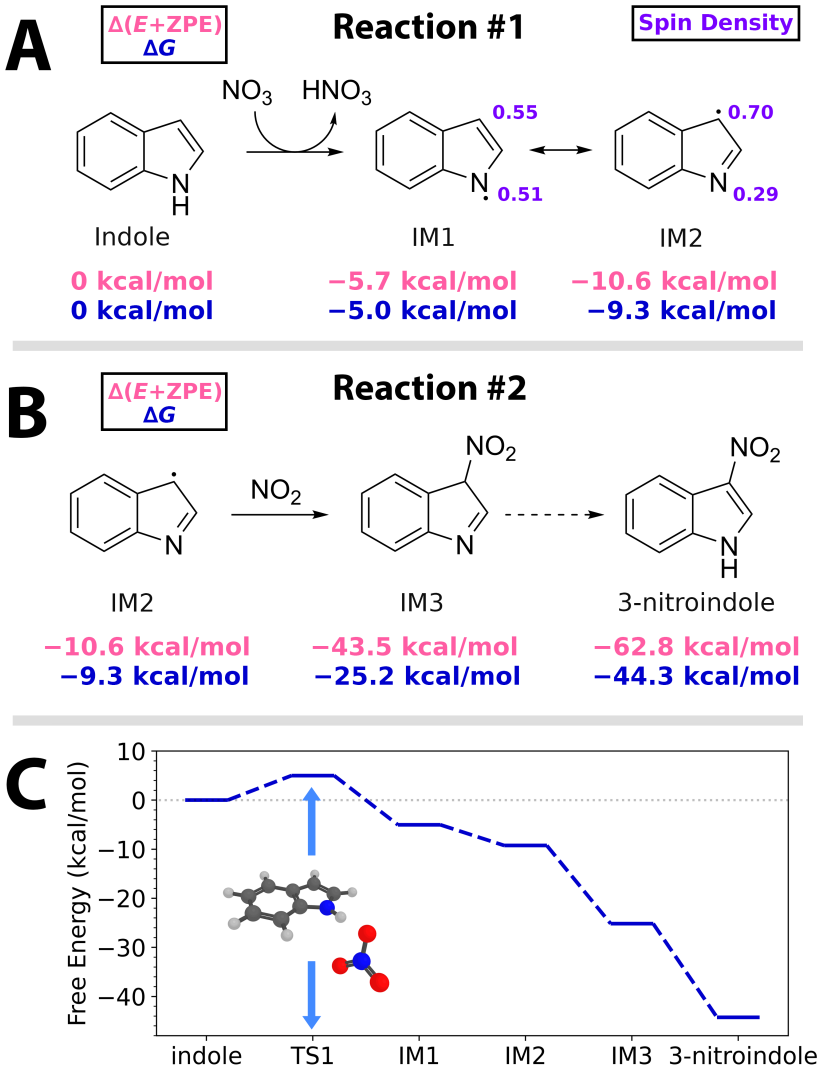

Figure 6.7: Thermochemical results at the PBE0/6-311++G(d,p) level for the hydrogen abstraction mechanism initiated by removal of the hydrogen at the N position (P1). $\Delta(E$+ZPE) values are provided in pink, and ΔG values are provided in blue, with reference to the reactants (including the oxidant) in each reaction.

Reaction 2, being a radical recombination reaction, should happen efficiently and potentially be barrierless.[251] The former is supported by the overall reaction being highly exergonic. While the remaining steps between IM3 and 3-nitroindole are uncertain, there is evidence that the yield for the IM3 $\rightarrow$ 3-nitroindole process is almost 100% by the striking lack of other isomers in the selected ion chromatograms (Fig. 6.2).

Given that this mechanism should be able to describe both OH and NO_3 initiated reactions, the conversion from IM3 to 3-nitroindole is likely to also be a multistep process. No attempt was made to model this process in this work. The simplest explanation would be that the excess energy after recombination would result in having sufficient energy for the internal hydrogen shift process. The alternative option would be another hydrogen abstraction process, in which the hydrogen is removed from P3 and subsequently returned to P1 by either HNO_3 or by another indole molecule. In environmental conditions, other hydrogen sources would be available as well.

6.3.6 An Unfavored Alternative: NO_3 Attachment

Given the previous studies which showed that attachment at P2 was favored in indole for other radicals, the analogous reaction was tested here for NO_3 with DFT. Limitations in computational resources made it difficult to compute frequencies for many of the intermediates at the MP2 level. Namely, the finite difference calculations required to compute the frequencies, which inherently take a long time, were often interrupted by issues with the SCF calculations. In some cases, warnings regarding linear dependencies in the AO basis sets appeared, which we attempted to alleviate with tighter screening thresholds and even trying less diffuse basis sets. Given these difficulties, and the appearance of two large transition state energy barriers predicted by DFT in Fig. 6.8, we elected to pause on the MP2 calculations for this pathway.

6.4 Conclusions

This work has provided strong evidence that 3-nitroindole is the major molecular component of indole + NO_3 secondary organic aerosol. The identification was confirmed by matching the retention time in chromatography, the shape of the absorption spectrum in UV/Vis spectroscopy, and the accurate mass-to-charge ratio in mass spectrometry. Furthermore, we were able to provide

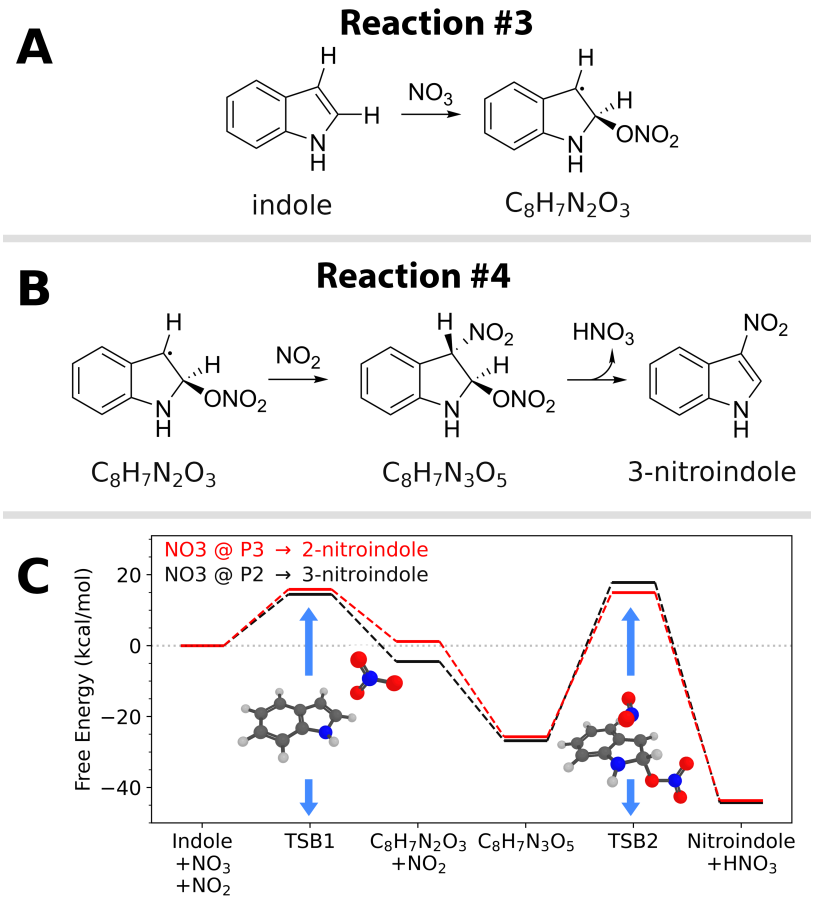

Figure 6.8: Hypothetical reaction mechanisms for a reaction pathway in which the NO3 attaches directly to pyrrole component of indole. This pathway is comprised of A) Reaction #3 and B) Reaction #4, which represent the attachment of NO_3 and NO_2 respectively. In C) is a free energy diagram (PBE0/6-311++G(d,p)) showing the Gibbs free energies of each structure with respect to all three reactants (indole, NO_3, and NO_2).

mechanistic justification for the dominant formation of 3-nitroindole with the aid of electronic structure calculations. The most likely mechanism appears to be initiated by NO_3 abstracting the hydrogen from the indole's N-H bond. Through resonance, the free electron density is shifted to the carbon in the 3 position of indole, priming the indole radical for a recombination reaction with NO_2, producing 3-nitroindole. We were able to rule out alternative mechanisms in which NO_3 either abstracts a hydrogen atom directly from a C-H bond or is added to indole instead of abstracting a hydrogen atom.

The ToF-AMS mass spectra were also remarkably similar between the SOA and the standard, with the parent ion (*m/z* 162) present in both the SOA and the standard. Various fragmentation peaks were also present, and shared similarities to electron ionization mass spectra of nitroindoles in the literature. It may be worth extending the *m/z* range of high-resolution ToF-AMS analysis to larger *m/z* (namely 132 and 162) when there is potential for indole oxidation products to be present, such as ambient measurements near animal husbandry facilities or during times of significant plant blooming.

Chapter 7

Summary of the Dissertation

This work has shed light on the optical properties of various nitroaromatic molecules that are often found in the atmosphere. The following questions were investigated:

1. Do the anions of nitrophenols have different photochemistry in non-aqueous solutions?
2. Do 4-nitrocatechol and 2,4-dinitrophenol undergo photochemical reactions in highly viscous organic matrices?
3. Do the photophysics of 4-nitrocatechol match observations with its photochemistry?
4. Can time-dependent density functional theory be used to reliably estimate intersystem crossing rates?
5. What is the major chromophore resulting from the indole + NO_3 reaction?

For the first point, it was shown that 2-nitrophenol and 4-nitrophenol (and also their anions) do not have drastically different photochemical degradation rates from previous observations for these molecules in aqueous solutions. The only molecule to show significantly more efficient photochemistry in the organic phase (liquid 2-propanol) was 2,4-dinitrophenol. Experiments with 2,4,6-trinitrophenol proved notably difficult, as the molecule is a strong acid that exists predominantly in the deprotonated form regardless of the choices of solvent or pH. The photochemical degradation of 2,4,6-trinitrophenol was similar to the less-substituted nitrophenols.

To investigate more toward the optical properties and photochemistry of nitroaromatics in highly viscous organic matrcies, isomalt was used as an organic aerosol proxy. The absorption spectrum of 4-nitrocatechol in the solid isomalt was effectively the same as in the liquid alcohol solvents, despite a slight redshift in the solid. The photochemistry of 4-nitrocatechol occured at similar rates between the liquid and solid organic matrices. Despite having similar rates, the products from photochemical reactions were observed to be different, with products corresponding to addition of -OH observed when 2-propanol was used as the solvent and products corresponding to reactions between two 4-nitrocatechol molecules observed when solid isomalt was used as the matrix.

Both the absorption spectrum and photochemistry of 2,4-dinitrophenol differed between the solid isomalt and the liquid alcohols. Of all of the molecules evaluated, 2,4-dinitrophenol had the most drastic changes in its absorption spectrum upon changing the solvent. In liquid alcohols, the absorption spectrum contained two separate absorption bands of roughly equal intensity. In the aqueous phase, the absorption bands were not as well separated and had different intensities. Surprisingly, the absorption spectrum of 2,4-dinitrophenol in isomalt more closely resembled the spectrum of the aqueous phase. An attempt was made to explain these differences using time-dependent density functional theory on explicity solvated complexes of 2,4-dinitrophenol with water and 2-propanol. The effects of explicit solvation were minimal, but did result in minor separation between the absorption bands when 2-propanol was included.

Based on an assumption that 4-nitrocatechol should photochemically react through excited triplet states, transient absorption experiments were conducted on 4-nitrocatechol with the hypothesis that such states would be observed on ultrafast time scales. Again, comparisons were made between experiments in the aqueous phase and the liquid organic phase. The transient absorption of 4-nitrocatechol after excitation to the first excited singlet state was probed using an ultrafast pump-probe spectroscopy setup. Stark differences in 4-nitrocatechol excited state absorption spectra depending on the solvent. In the aqueous phase, the excited state lifetimes

were ultrashort, with much of the transient absorption disappearing in less than a few picoseconds. The excited state absorption bands were much stronger in 2-propanol, and remained for up to 100 picoseconds. From these observations it was concluded that triplets states are minimally populated in 4-nitrocatechol when dissolved in water. From the transient absorption spectra at longer time delays (around 3 nanoseconds) it was concluded that 4-nitrocatechol behaves as a photoacid in both water and 2-propanol. These conclusions provide nice context to the results from the photochemistry studies of 4-nitrocatechol, where photodegradation in water was negligible and photodegradation in 2-propanol was appreciable but also relatively slow. In the case of 4-nitrocatechol in protic solvents, a significant portion of excited state population results in deprotonation of the molecule, minimizing the impact of photochemistry toward its removal.

An attempt was also made to reconcile the disparate use of Fermi's golden rule and the energy gap law to computationally describe intersystem crossing in organic molecules. Plagued by mismatched notation and inconsistent application in the literature, the theoretical framework was reviewed and applied to predict the intersystem crossing rate constants in nitrobenzene. In comparison to experimental observations in the literature, the best match in theoretical rate constant determination was provided by the unconventional use of a Lorentzian-like equation.

The final chapter of this dissertation changes gears from its focus on photochemistry to investigate the secondary organic aerosol formed from reactions of indole and the nitrate radical, NO_3. Specifically, previous studies observed a strongly absorbing product in this aerosol that has a molecular formula matching with nitroindole. Despite having multiple sites upon which an NO_2 group could be added to indole, it appeared that only one isomer was dominantly formed. Since no previous studies were able to provide comparison to nitroindole standards, the exact isomer needed to be confirmed. As such, the analytical trifecta of chromatography, UV/Vis spectrscopy, and mass spectrometry was used to confirm that 3-nitroindole is the isomer formed in the indole + NO_3 secondary organic aerosol. Upon finding this as the product, density functional theory was used to confirm the mechanism by which 3-nitroindole is formed. This work showed that

the reaction occurs via hydrogen abstraction from the N-H bond in indole, after which the intermediate is stabilized by resonance to promote NO_2 addition at the 3 position of the intermediate radical.

The work with indole was undoubtedly the most conclusive work of this dissertation. Some questions still remain from the other parts of this work:

1. The differences in photochemical products in 4-nitrocatechol make it difficult to tease out the role of viscosity toward photodegradation. Would reactions between two 4-nitrocatechol molecules take over if experiments in 2-propanol are done in anoxic conditions? If so, would the reaction rate slow down in the case that two 4-nitrocatechol molecules need to diffuse toward each other in solution? To answer these questions, future experiments should examine the photochemistry of 4-nitrocatechol as a function of O_2 concentration.
2. Why does 2,4-dinitrophenol have differently shaped absorption spectra in different solvents/matrices? We considered differences in solvation but did not consider major solvent-dependent geometric reconfigurations of 2,4-dinitrophenol, which would also cause considerable spectral differences. To investigate these unique optical properties, more sophisticated solvation models should be tested in quantum chemical calculations. Measurements could also be taken in a cryogenic argon matrix to hone in on the effects of specific intramolecular interactions.
3. There appeared to be a small exicted state absorption signal potentially by triplet states in 4-nitrocatechol, even at long time scales. What fraction of the overall excited population ends up in a long-lived triplet state? Does the quantum yield of that process match the photochemical reaction yield we observed? Further experiments should evaluate the yield of singlet oxygen ($^1O_2$) in solution, which is a common product from the reaction of organic triplet states with dissolved oxygen. Phosphorescence experiments could also detect the loss of triplet 4-nitrocatechol directly.

Bibliography

(*1*) Gaston, C. J., Lopez-Hilfiker, F. D., Whybrew, L. E., Hadley, O., McNair, F., Gao, H., Jaffe, D. A., and Thornton, J. A. (2016). Online molecular characterization of fine particulate matter in Port Angeles, WA: Evidence for a major impact from residential wood smoke. *Atmospheric Environment 138*, 99–107.

(*2*) Al-Naiema, I. M., and Stone, E. A. (2017). Evaluation of anthropogenic secondary organic aerosol tracers from aromatic hydrocarbons. *Atmospheric Chemistry and Physics 17*, 2053–2065.

(*3*) Palm, B. B. et al. (2020). Quantification of organic aerosol and brown carbon evolution in fresh wildfire plumes. *Proceedings of the National Academy of Sciences 117*, 29469–29477.

(*4*) Yassine, M. M., Suski, M., and Dabek-Zlotorzynska, E. (2020). Characterization of benzene polycarboxylic acids and polar nitroaromatic compounds in atmospheric aerosols using UPLC-MS/MS. *Journal of Chromatography A 1630*, 461507.

(*5*) Washenfelder, R. A. et al. (2022). Complexity in the Evolution, Composition, and Spectroscopy of Brown Carbon in Aircraft Measurements of Wildfire Plumes. *Geophysical Research Letters 49*, e2022GL098951.

(*6*) Claeys, M., Vermeylen, R., Yasmeen, F., Gómez-González, Y., Chi, X., Maenhaut, W., Mészáros, T., and Salma, I. (2012). Chemical characterisation of humic-like substances from urban, rural and tropical biomass burning environments using liquid chromatography with UV/vis

photodiode array detection and electrospray ionisation mass spectrometry. *Environmental Chemistry 9*, 273–284.

(*7*) Caumo, S. E. S., Claeys, M., Maenhaut, W., Vermeylen, R., Behrouzi, S., Safi Shalamzari, M., and Vasconcellos, P. C. (2016). Physicochemical characterization of winter PM10 aerosol impacted by sugarcane burning from São Paulo city, Brazil. *Atmospheric Environment 145*, 272–279.

(*8*) Wu, H. et al. (2021). Rapid transformation of ambient absorbing aerosols from West African biomass burning. *Atmospheric Chemistry and Physics 21*, 9417–9440.

(*9*) Desyaterik, Y., Sun, Y., Shen, X., Lee, T., Wang, X., Wang, T., and Collett Jr., J. L. (2013). Speciation of "brown" carbon in cloud water impacted by agricultural biomass burning in eastern China. *Journal of Geophysical Research: Atmospheres 118*, 7389–7399.

(*10*) Lin, P., Bluvshtein, N., Rudich, Y., Nizkorodov, S. A., Laskin, J., and Laskin, A. (2017). Molecular Chemistry of Atmospheric Brown Carbon Inferred from a Nationwide Biomass Burning Event. *Environmental Science & Technology 51*, 11561–11570.

(*11*) Chow, K. S., Huang, X. H. H., and Yu, J. Z. (2015). Quantification of nitroaromatic compounds in atmospheric fine particulate matter in Hong Kong over 3 years: field measurement evidence for secondary formation derived from biomass burning emissions. *Environmental Chemistry 13*, 665–673.

(*12*) Bluvshtein, N. et al. (2017). Broadband optical properties of biomass-burning aerosol and identification of brown carbon chromophores. *Journal of Geophysical Research: Atmospheres 122*, 5441–5456.

(*13*) Lin, N.-H. et al. (2013). An overview of regional experiments on biomass burning aerosols and related pollutants in Southeast Asia: From BASE-ASIA and the Dongsha Experiment to 7-SEAS. *Atmospheric Environment 78*, 1–19.

(*14*) Wang, Y. et al. (2017). Molecular Characterization of Nitrogen-Containing Organic Compounds in Humic-like Substances Emitted from Straw Residue Burning. *Environmental Science & Technology 51*, 5951–5961.

(*15*) Ikemori, F., Nakayama, T., and Hasegawa, H. (2019). Characterization and possible sources of nitrated mono- and di-aromatic hydrocarbons containing hydroxyl and/or carboxyl functional groups in ambient particles in Nagoya, Japan. *Atmospheric Environment 211*, 91–102.

(*16*) Li, X., Wang, Y., Hu, M., Tan, T., Li, M., Wu, Z., Chen, S., and Tang, X. (2020). Characterizing chemical composition and light absorption of nitroaromatic compounds in the winter of Beijing. *Atmospheric Environment 237*, 117712.

(*17*) Salvador, C. M. G. et al. (2021). Ambient nitro-aromatic compounds – biomass burning versus secondary formation in rural China. *Atmospheric Chemistry and Physics 21*, 1389–1406.

(*18*) Wang, Z., Zhang, J., Zhang, L., Liang, Y., and Shi, Q. (2021). Characterization of nitroaromatic compounds in atmospheric particulate matter from Beijing. *Atmospheric Environment 246*, 118046.

(*19*) Zhang, L., Son, J. H., Bai, Z., Zhang, W., Li, L., Wang, L., and Chen, J. (2022). Characterizing Atmospheric Brown Carbon and Its Emission Sources during Wintertime in Shanghai, China. *Atmosphere 13*, 991.

(*20*) Iinuma, Y., Keywood, M., and Herrmann, H. (2016). Characterization of primary and secondary organic aerosols in Melbourne airshed: The influence of biogenic emissions, wood smoke and bushfires. *Atmospheric Environment 130*, 54–63.

(*21*) Cecinato, A., Di Palo, V., Pomata, D., Tomasi Scianò, M. C., and Possanzini, M. (2005). Measurement of phase-distributed nitrophenols in Rome ambient air. *Chemosphere 59*, 679–683.

(*22*) Iinuma, Y., Böge, O., Gräfe, R., and Herrmann, H. (2010). Methyl-Nitrocatechols: Atmospheric Tracer Compounds for Biomass Burning Secondary Organic Aerosols. *Environmental Science & Technology 44*, 8453–8459.

(*23*) Zhang, Y. Y., Müller, L., Winterhalter, R., Moortgat, G. K., Hoffmann, T., and Pöschl, U. (2010). Seasonal cycle and temperature dependence of pinene oxidation products, dicarboxylic acids and nitrophenols in fine and coarse air particulate matter. *Atmospheric Chemistry and Physics 10*, 7859–7873.

(*24*) Kitanovski, Z., Grgić, I., Vermeylen, R., Claeys, M., and Maenhaut, W. (2012). Liquid chromatography tandem mass spectrometry method for characterization of monoaromatic nitro-compounds in atmospheric particulate matter. *Journal of Chromatography A 1268*, 35–43.

(*25*) Mohr, C. et al. (2013). Contribution of Nitrated Phenols to Wood Burning Brown Carbon Light Absorption in Detling, United Kingdom during Winter Time. *Environmental Science & Technology 47*, 6316–6324.

(*26*) Teich, M., van Pinxteren, D., Wang, M., Kecorius, S., Wang, Z., Müller, T., Močnik, G., and Herrmann, H. (2017). Contributions of nitrated aromatic compounds to the light absorption of water-soluble and particulate brown carbon in different atmospheric environments in Germany and China. *Atmospheric Chemistry and Physics 17*, 1653–1672.

(*27*) Kitanovski, Z., Shahpoury, P., Samara, C., Voliotis, A., and Lammel, G. (2020). Composition and mass size distribution of nitrated and oxygenated aromatic compounds in ambient particulate matter from southern and central Europe – implications for the origin. *Atmospheric Chemistry and Physics 20*, 2471–2487.

(*28*) Kitanovski, Z., Hovorka, J., Kuta, J., Leoni, C., Prokeš, R., Sáňka, O., Shahpoury, P., and Lammel, G. (2021). Nitrated monoaromatic hydrocarbons (nitrophenols, nitrocatechols, nitrosalicylic acids) in ambient air: levels, mass size distributions and inhalation bioaccessibility. *Environmental Science and Pollution Research 28*, 59131–59140.

(*29*) Frka, S., Šala, M., Brodnik, H., Štefane, B., Kroflič, A., and Grgić, I. (2022). Seasonal variability of nitroaromatic compounds in ambient aerosols: Mass size distribution, possible sources and contribution to water-soluble brown carbon light absorption. *Chemosphere 299*, 134381.

(*30*) Amarandei, C., Olariu, R. I., and Arsene, C. (2023). First insights into the molecular characteristics of atmospheric organic aerosols from Iasi, Romania: Behavior of biogenic *versus* anthropogenic contributions and potential implications. *Science of The Total Environment 877*, 162830.

(*31*) Iinuma, Y., Brüggemann, E., Gnauk, T., Müller, K., Andreae, M. O., Helas, G., Parmar, R., and Herrmann, H. (2007). Source characterization of biomass burning particles: The combustion of selected European conifers, African hardwood, savanna grass, and German and Indonesian peat. *Journal of Geophysical Research: Atmospheres 112*, DOI: 10.1029/2006JD007120.

(*32*) Laskin, A., Smith, J. S., and Laskin, J. (2009). Molecular Characterization of Nitrogen-Containing Organic Compounds in Biomass Burning Aerosols Using High-Resolution Mass Spectrometry. *Environmental Science & Technology 43*, 3764–3771.

(*33*) Lin, P., Aiona, P. K., Li, Y., Shiraiwa, M., Laskin, J., Nizkorodov, S. A., and Laskin, A. (2016). Molecular Characterization of Brown Carbon in Biomass Burning Aerosol Particles. *Environmental Science & Technology 50*, 11815–11824.

(*34*) Fleming, L. T., Lin, P., Roberts, J. M., Selimovic, V., Yokelson, R., Laskin, J., Laskin, A., and Nizkorodov, S. A. (2020). Molecular composition and photochemical lifetimes of brown carbon chromophores in biomass burning organic aerosol. *Atmospheric Chemistry and Physics 20*, 1105–1129.

(*35*) Kahnt, A., Behrouzi, S., Vermeylen, R., Safi Shalamzari, M., Vercauteren, J., Roekens, E., Claeys, M., and Maenhaut, W. (2013). One-year study of nitro-organic compounds and

their relation to wood burning in PM10 aerosol from a rural site in Belgium. *Atmospheric Environment 81*, 561–568.

(*36*) Li, X., Jiang, L., Hoa, L. P., Lyu, Y., Xu, T., Yang, X., Iinuma, Y., Chen, J., and Herrmann, H. (2016). Size distribution of particle-phase sugar and nitrophenol tracers during severe urban haze episodes in Shanghai. *Atmospheric Environment 145*, 115–127.

(*37*) Bertrand, A. et al. (2018). Evolution of the chemical fingerprint of biomass burning organic aerosol during aging. *Atmospheric Chemistry and Physics 18*, 7607–7624.

(*38*) Finewax, Z., de Gouw, J. A., and Ziemann, P. J. (2018). Identification and Quantification of 4-Nitrocatechol Formed from OH and NO3 Radical-Initiated Reactions of Catechol in Air in the Presence of NOx: Implications for Secondary Organic Aerosol Formation from Biomass Burning. *Environmental Science & Technology 52*, 1981–1989.

(*39*) Vidović, K., Lašič Jurković, D., Šala, M., Kroflič, A., and Grgić, I. (2018). Nighttime Aqueous-Phase Formation of Nitrocatechols in the Atmospheric Condensed Phase. *Environmental Science & Technology 52*, 9722–9730.

(*40*) Mayorga, R. J., Zhao, Z., and Zhang, H. (2021). Formation of secondary organic aerosol from nitrate radical oxidation of phenolic VOCs: Implications for nitration mechanisms and brown carbon formation. *Atmospheric Environment 244*, 117910.

(*41*) Kroflič, A., Anders, J., Drventić, I., Mettke, P., Böge, O., Mutzel, A., Kleffmann, J., and Herrmann, H. (2021). Guaiacol Nitration in a Simulated Atmospheric Aerosol with an Emphasis on Atmospheric Nitrophenol Formation Mechanisms. *ACS Earth and Space Chemistry 5*, 1083–1093.

(*42*) Fredrickson, C. D. et al. (2022). Formation and Evolution of Catechol-Derived SOA Mass, Composition, Volatility, and Light Absorption. *ACS Earth and Space Chemistry 6*, 1067–1079.

(*43*) Klodt, A. L., Adamek, M., Dibley, M., Nizkorodov, S. A., and O'Brien, R. E. (2022). Effects of the sample matrix on the photobleaching and photodegradation of toluene-derived secondary organic aerosol compounds. *Atmospheric Chemistry and Physics 22*, 10155–10171.

(*44*) Spalding, R. F., and Fulton, J. W. (1988). Groundwater munition residues and nitrate near Grand Island, Nebraska, U.S.A. *Journal of Contaminant Hydrology 2*, 139–153.

(*45*) Kjeldsen, P., Kjølholt, J., Schultz, B., Christensen, T. H., and Tjell, J. C. (1990). Sorption and degradation of chlorophenols, nitrophenols and organophosphorus pesticides in the subsoil under landfills — laboratory studies. *Journal of Contaminant Hydrology 6*, 165–184.

(*46*) Gil, Y., and Sinfort, C. (2005). Emission of pesticides to the air during sprayer application: A bibliographic review. *Atmospheric Environment 39*, 5183–5193.

(*47*) Scott, W. D. (1978). The pH of cloud water and the production of sulfate. *Atmospheric Environment (1967) 12*, 917–921.

(*48*) Turnock, S. T., Mann, G. W., Woodhouse, M. T., Dalvi, M., O'Connor, F. M., Carslaw, K. S., and Spracklen, D. V. (2019). The Impact of Changes in Cloud Water pH on Aerosol Radiative Forcing. *Geophysical Research Letters 46*, 4039–4048.

(*49*) Pearce, P. J., and Simkins, R. J. J. (1968). Acid strengths of some substituted picric acids. *Canadian Journal of Chemistry 46*, 241–248.

(*50*) Hinrichs, R. Z., Buczek, P., and Trivedi, J. J. (2016). Solar Absorption by Aerosol-Bound Nitrophenols Compared to Aqueous and Gaseous Nitrophenols. *Environmental Science & Technology 50*, 5661–5667.

(*51*) Barsotti, F., Bartels-Rausch, T., De Laurentiis, E., Ammann, M., Brigante, M., Mailhot, G., Maurino, V., Minero, C., and Vione, D. (2017). Photochemical Formation of Nitrite and Nitrous Acid (HONO) upon Irradiation of Nitrophenols in Aqueous Solution and in Viscous Secondary Organic Aerosol Proxy. *Environmental Science & Technology 51*, 7486–7495.

(*52*) Koop, T., Bookhold, J., Shiraiwa, M., and Pöschl, U. (2011). Glass transition and phase state of organic compounds: dependency on molecular properties and implications for secondary organic aerosols in the atmosphere. *Physical Chemistry Chemical Physics 13*, 19238–19255.

(*53*) Hinks, M. L., Brady, M. V., Lignell, H., Song, M., Grayson, J. W., Bertram, A. K., Lin, P., Laskin, A., Laskin, J., and Nizkorodov, S. A. (2016). Effect of viscosity on photodegradation rates in complex secondary organic aerosol materials. *Physical Chemistry Chemical Physics 18*, 8785–8793.

(*54*) Leuenberger, C., Czuczwa, J., Tremp, J., and Giger, W. (1988). Nitrated phenols in rain: Atmospheric occurrence of phytotoxic pollutants. *Chemosphere 17*, 511–515.

(*55*) Lüttke, J., Scheer, V., Levsen, K., Wünsch, G., Neil Cape, J., Hargreaves, K. J., Storeton-West, R. L., Acker, K., Wieprecht, W., and Jones, B. (1997). Occurrence and formation of nitrated phenols in and out of cloud. *Atmospheric Environment 31*, 2637–2648.

(*56*) Özel, M. Z., Hamilton, J. F., and Lewis, A. C. (2011). New Sensitive and Quantitative Analysis Method for Organic Nitrogen Compounds in Urban Aerosol Samples. *Environmental Science & Technology 45*, 1497–1505.

(*57*) Rubio, M. A., Lissi, E., Herrera, N., Pérez, V., and Fuentes, N. (2012). Phenol and nitrophenols in the air and dew waters of Santiago de Chile. *Chemosphere 86*, 1035–1039.

(*58*) Harrison, M. A. J., Barra, S., Borghesi, D., Vione, D., Arsene, C., and Iulian Olariu, R. (2005). Nitrated phenols in the atmosphere: a review. *Atmospheric Environment 39*, 231–248.

(*59*) Bejan, I., Aal, Y. A. E., Barnes, I., Benter, T., Bohn, B., Wiesen, P., and Kleffmann, J. (2006). The photolysis of ortho-nitrophenols: a new gas phase source of HONO. *Physical Chemistry Chemical Physics 8*, 2028–2035.

(*60*) Chen, J., Wenger, J. C., and Venables, D. S. (2011). Near-Ultraviolet Absorption Cross Sections of Nitrophenols and Their Potential Influence on Tropospheric Oxidation Capacity. *The Journal of Physical Chemistry A 115*, 12235–12242.

(*61*) Sangwan, M., and Zhu, L. (2016). Absorption Cross Sections of 2-Nitrophenol in the 295–400 nm Region and Photolysis of 2-Nitrophenol at 308 and 351 nm. *The Journal of Physical Chemistry A 120*, 9958–9967.

(*62*) Leier, J., Michenfelder, N. C., Unterreiner, A.-N., and Olzmann, M. (2021). Indications for an intermolecular photo-induced excited-state proton transfer of p-nitrophenol in water. *Molecular Physics 119*, e1975051.

(*63*) Hofmann, D., Hartmann, F., and Herrmann, H. (2008). Analysis of nitrophenols in cloud water with a miniaturized light-phase rotary perforator and HPLC-MS. *Analytical and Bioanalytical Chemistry 391*, 161–169.

(*64*) Ganranoo, L., Mishra, S. K., Azad, A. K., Shigihara, A., Dasgupta, P. K., Breitbach, Z. S., Armstrong, D. W., Grudpan, K., and Rappenglueck, B. (2010). Measurement of Nitrophenols in Rain and Air by Two-Dimensional Liquid ChromatographyChemically Active Liquid Core Waveguide Spectrometry. *Analytical Chemistry 82*, 5838–5843.

(*65*) Teich, M., van Pinxteren, D., and Herrmann, H. (2014). Determination of nitrophenolic compounds from atmospheric particles using hollow-fiber liquid-phase microextraction and capillary electrophoresis/mass spectrometry analysis. *ELECTROPHORESIS 35*, 1353–1361.

(*66*) Vione, D., Maurino, V., Minero, C., and Pelizzetti, E. (2005). Aqueous Atmospheric Chemistry: Formation of 2,4-Dinitrophenol upon Nitration of 2-Nitrophenol and 4-Nitrophenol in Solution. *Environmental Science & Technology 39*, 7921–7931.

(*67*) Xie, M., Chen, X., Hays, M. D., and Holder, A. L. (2019). Composition and light absorption of N-containing aromatic compounds in organic aerosols from laboratory biomass burning. *Atmospheric Chemistry and Physics 19*, 2899–2915.

(*68*) Yang, Y., Li, X., Shen, R., Liu, Z., Ji, D., and Wang, Y. (2020). Seasonal variation and sources of derivatized phenols in atmospheric fine particulate matter in North China Plain. *Journal of Environmental Sciences 89*, 136–144.

(*69*) Cai, D., Wang, X., George, C., Cheng, T., Herrmann, H., Li, X., and Chen, J. (2022). Formation of Secondary Nitroaromatic Compounds in Polluted Urban Environments. *Journal of Geophysical Research: Atmospheres 127*, e2021JD036167.

(*70*) Zhao, R., Lee, A. K. Y., Huang, L., Li, X., Yang, F., and Abbatt, J. P. D. (2015). Photochemical processing of aqueous atmospheric brown carbon. *Atmospheric Chemistry and Physics 15*, 6087–6100.

(*71*) Hems, R. F., and Abbatt, J. P. D. (2018). Aqueous Phase Photo-oxidation of Brown Carbon Nitrophenols: Reaction Kinetics, Mechanism, and Evolution of Light Absorption. *ACS Earth and Space Chemistry 2*, 225–234.

(*72*) Price, C. L., Preston, T. C., and Davies, J. F. (2022). Hygroscopic Growth, Phase Morphology, and Optical Properties of Model Aqueous Brown Carbon Aerosol. *Environmental Science & Technology 56*, 3941–3951.

(*73*) Amugoda, M., Singh, P., Salas, S., and Davies, J. F. (2024). Hygroscopicity and Volatility of Biomass Burning Aromatic and Nitroaromatic Compounds. *ACS ES&T Air 1*, 294–304.

(*74*) Bertram, A. K., Ivanov, A. V., Hunter, M., Molina, L. T., and Molina, M. J. (2001). The Reaction Probability of OH on Organic Surfaces of Tropospheric Interest. *The Journal of Physical Chemistry A 105*, 9415–9421.

(*75*) Smith, J. D., Kroll, J. H., Cappa, C. D., Che, D. L., Liu, C. L., Ahmed, M., Leone, S. R., Worsnop, D. R., and Wilson, K. R. (2009). The heterogeneous reaction of hydroxyl radicals with sub-micron squalane particles: a model system for understanding the oxidative aging of ambient aerosols. *Atmospheric Chemistry and Physics 9*, 3209–3222.

(*76*) George, I. J., and Abbatt, J. P. D. (2010). Chemical evolution of secondary organic aerosol from OH-initiated heterogeneous oxidation. *Atmospheric Chemistry and Physics 10*, 5551–5563.

(*77*) Roman, C., Arsene, C., Bejan, I. G., and Olariu, R. I. (2022). Investigations into the gas-phase photolysis and OH radical kinetics of nitrocatechols: implications of intramolecular interactions on their atmospheric behaviour. *Atmospheric Chemistry and Physics 22*, 2203–2219.

(*78*) Rippen, G., Zietz, E., Frank, R., Knacker, T., and Klöpffer, W. (1987). Do airborne nitrophenols contribute to forest decline? *Environmental Technology Letters 8*, 475–482.

(*79*) Natangelo, M., Mangiapan, S., Bagnati, R., Benfenati, E., and Fanelli, R. (1999). Increased concentrations of nitrophenols in leaves from a damaged forestal site. *Chemosphere 38*, 1495–1503.

(*80*) Tremp, J., Mattrel, P., Fingler, S., and Giger, W. (1993). Phenols and nitrophenols as tropospheric pollutants: Emissions from automobile exhausts and phase transfer in the atmosphere. *Water, Air, and Soil Pollution 68*, 113–123.

(*81*) Belloli, R., Barletta, B., Bolzacchini, E., Meinardi, S., Orlandi, M., and Rindone, B. (1999). Determination of toxic nitrophenols in the atmosphere by high-performance liquid chromatography. *Journal of Chromatography A 846*, 277–281.

(*82*) Dubowski, Y., and Hoffmann, M. R. (2000). Photochemical transformations in ice: Implications for the fate of chemical species. *Geophysical Research Letters 27*, 3321–3324.

(*83*) Vione, D., Maurino, V., Minero, C., Duncianu, M., Olariu, R.-I., Arsene, C., Sarakha, M., and Mailhot, G. (2009). Assessing the transformation kinetics of 2- and 4-nitrophenol in the atmospheric aqueous phase. Implications for the distribution of both nitroisomers in the atmosphere. *Atmospheric Environment 43*, 2321–2327.

(*84*) Lignell, H., Hinks, M. L., and Nizkorodov, S. A. (2014). Exploring matrix effects on photochemistry of organic aerosols. *Proceedings of the National Academy of Sciences 111*, 13780–13785.

(*85*) Ernst, H. A., Wolf, T. J. A., Schalk, O., González-García, N., Boguslavskiy, A. E., Stolow, A., Olzmann, M., and Unterreiner, A.-N. (2015). Ultrafast Dynamics of o-Nitrophenol: An Experimental and Theoretical Study. *The Journal of Physical Chemistry A 119*, 9225–9235.

(*86*) Vereecken, L., Chakravarty, H. K., Bohn, B., and Lelieveld, J. (2016). Theoretical Study on the Formation of H- and O-Atoms, HONO, OH, NO, and NO2 from the Lowest Lying Singlet and Triplet States in Ortho-Nitrophenol Photolysis. *International Journal of Chemical Kinetics 48*, 785–795.

(*87*) Atkinson, R., Aschmann, S. M., and Arey, J. (1992). Reactions of hydroxyl and nitrogen trioxide radicals with phenol, cresols, and 2-nitrophenol at 296 .+-. 2 K. *Environmental Science & Technology 26*, 1397–1403.

(*88*) Bolzacchini, E., Bruschi, M., Hjorth, J., Meinardi, S., Orlandi, M., Rindone, B., and Rosenbohm, E. (2001). Gas-Phase Reaction of Phenol with NO3. *Environmental Science & Technology 35*, 1791–1797.

(*89*) Vione, D., Maurino, V., Minero, C., and Pelizzetti, E. (2001). Phenol photonitration upon UV irradiation of nitrite in aqueous solution I: Effects of oxygen and 2-propanol. *Chemosphere 45*, 893–902.

(*90*) Dalton, A. B., and Nizkorodov, S. A. (2021). Photochemical Degradation of 4-Nitrocatechol and 2,4-Dinitrophenol in a Sugar-Glass Secondary Organic Aerosol Surrogate. *Environmental Science & Technology 55*, 14586–14594.

(*91*) Kroll, J. H., and Seinfeld, J. H. (2008). Chemistry of secondary organic aerosol: Formation and evolution of low-volatility organics in the atmosphere. *Atmospheric Environment 42*, 3593–3624.

(*92*) Grygoryeva, K., Kubečka, J., Pysanenko, A., Lengyel, J., Slavíček, P., and Fárník, M. (2016). Photochemistry of Nitrophenol Molecules and Clusters: Intra- vs Intermolecular Hydrogen Bond Dynamics. *The Journal of Physical Chemistry A 120*, 4139–4146.

(*93*) Hurley, R., and Testa, A. C. (1967). Nitrobenzene photochemistry. II. Protonation in the excited state. *Journal of the American Chemical Society 89*, 6917–6919.

(*94*) Hurley, R., and Testa, A. C. (1966). Photochemical n $\rightarrow$ * Excitation of Nitrobenzene. *Journal of the American Chemical Society 88*, 4330–4332.

(*95*) Döpp, D. In *Triplet States II*, ed. by Wild, U. P., Döpp, D., and Dürr, H., Berlin, Heidelberg, 1975, pp 49–85.

(*96*) Epifanovsky, E. et al. (2021). Software for the frontiers of quantum chemistry: An overview of developments in the Q-Chem 5 package. *The Journal of Chemical Physics 155*, 084801.

(*97*) Becke, A. D. (1993). Density-functional thermochemistry. III. The role of exact exchange. *The Journal of Chemical Physics 98*, 5648–5652.

(*98*) Adamo, C., and Barone, V. (1999). Toward reliable density functional methods without adjustable parameters: The PBE0 model. *The Journal of Chemical Physics 110*, 6158–6170.

(*99*) Cornard, J.-P., Rasmiwetti, and Merlin, J.-C. (2005). Molecular structure and spectroscopic properties of 4-nitrocatechol at different pH: UV–visible, Raman, DFT and TD-DFT calculations. *Chemical Physics 309*, 239–249.

(*100*) Reichardt, C., Vogt, R. A., and Crespo-Hernández, C. E. (2009). On the origin of ultrafast nonradiative transitions in nitro-polycyclic aromatic hydrocarbons: Excited-state dynamics in 1-nitronaphthalene. *The Journal of Chemical Physics 131*, 224518.

(*101*) Hirata, S., and Head-Gordon, M. (1999). Time-dependent density functional theory within the Tamm–Dancoff approximation. *Chemical Physics Letters 314*, 291–299.

(*102*) Peach, M. J. G., Williamson, M. J., and Tozer, D. J. (2011). Influence of Triplet Instabilities in TDDFT. *Journal of Chemical Theory and Computation 7*, 3578–3585.

(*103*) Barone, V., Cossi, M., and Tomasi, J. (1997). A new definition of cavities for the computation of solvation free energies by the polarizable continuum model. *The Journal of Chemical Physics 107*, 3210–3221.

(*104*) Truong, T. N., and Stefanovich, E. V. (1995). A new method for incorporating solvent effect into the classical, ab initio molecular orbital and density functional theory frameworks for arbitrary shape cavity. *Chemical Physics Letters 240*, 253–260.

(*105*) Martin, R. L. (2003). Natural transition orbitals. *The Journal of Chemical Physics 118*, 4775–4777.

(*106*) Glendening, E. D., Landis, C. R., and Weinhold, F. (2013). NBO 6.0: Natural bond orbital analysis program. *Journal of Computational Chemistry 34*, 1429–1437.

(*107*) Wanko, M., Houmøller, J., Støchkel, K., Kirketerp, M.-B. S., Petersen, M. Å., Nielsen, M. B., Nielsen, S. B., and Rubio, A. (2012). Substitution effects on the absorption spectra of nitrophenolate isomers. *Physical Chemistry Chemical Physics 14*, 12905–12911.

(*108*) Houmøller, J., Wanko, M., Rubio, A., and Nielsen, S. B. (2015). Effect of a Single Water Molecule on the Electronic Absorption by o- and p-Nitrophenolate: A Shift to the Red or to the Blue? *The Journal of Physical Chemistry A 119*, 11498–11503.

(*109*) Michenfelder, N. C., Ernst, H. A., Schweigert, C., Olzmann, M., and Unterreiner, A.-N. (2018). Ultrafast stimulated emission of nitrophenolates in organic and aqueous solutions. *Physical Chemistry Chemical Physics 20*, 10713–10720.

(*110*) Rondinini, S., Longhi, P., Mussini, P. R., and Mussini, T. (1987). Autoprotolysis constants in nonaqueous solvents and aqueous organic solvent mixtures. *Pure and Applied Chemistry 59*, 1693–1702.

(*111*) Ault, A. P. (2020). Aerosol Acidity: Novel Measurements and Implications for Atmospheric Chemistry. *Accounts of Chemical Research 53*, 1703–1714.

(*112*) Alif, A., Pilichowski, J.-F., and Boule, P. (1991). Photochemistry and environment XIII: Phototransformation of 2-nitrophenol in aqueous solution. *Journal of Photochemistry and Photobiology A: Chemistry 59*, 209–219.

(*113*) Braman, T., Dolvin, L., Thrasher, C., Yu, H., Walhout, E. Q., and O'Brien, R. E. (2020). Fresh versus Photo-recalcitrant Secondary Organic Aerosol: Effects of Organic Mixtures on Aqueous Photodegradation of 4-Nitrophenol. *Environmental Science & Technology Letters 7*, 248–253.

(*114*) Lemaire, J., Guth, J. A., Klais, O., Leahey, J., Merz, W., Philp, J., Wilmes, R., and Wolff, C. J. M. (1985). Ring test of a method for assessing the phototransformation of chemicals in water. *Chemosphere 14*, 53–77.

(*115*) Einschlag, F. S. G., Carlos, L., Capparelli, A. L., Braun, A. M., and Oliveros, E. (2002). Degradation of nitroaromatic compounds by the UV–H2O2 process using polychromatic radiation sources. *Photochemical & Photobiological Sciences 1*, 520–525.

(*116*) Albinet, A., Minero, C., and Vione, D. (2010). Phototransformation processes of 2,4-dinitrophenol, relevant to atmospheric water droplets. *Chemosphere 80*, 753–758.

(*117*) Epstein, S. A., Shemesh, D., Tran, V. T., Nizkorodov, S. A., and Gerber, R. B. (2012). Absorption Spectra and Photolysis of Methyl Peroxide in Liquid and Frozen Water. *The Journal of Physical Chemistry A 116*, 6068–6077.

(*118*) Harbach, P. H. P., Wormit, M., and Dreuw, A. (2014). The third-order algebraic diagrammatic construction method (ADC(3)) for the polarization propagator for closed-shell molecules: Efficient implementation and benchmarkinga). *The Journal of Chemical Physics 141*, 064113.

(*119*) Karimova, N. V., Luo, M., Grassian, V. H., and Gerber, R. B. (2020). Absorption spectra of benzoic acid in water at different pH and in the presence of salts: insights from the integration of experimental data and theoretical cluster models. *Physical Chemistry Chemical Physics 22*, 5046–5056.

(*120*) Karimova, N. V., Luo, M., Sit, I., Grassian, V. H., and Gerber, R. B. (2022). Absorption Spectra and the Electronic Structure of Gallic Acid in Water at Different pH: Experimental Data and Theoretical Cluster Models. *The Journal of Physical Chemistry A 126*, 190–197.

(*121*) Rao, L., Ke, H., Fu, G., Xu, X., and Yan, Y. (2009). Performance of Several Density Functional Theory Methods on Describing Hydrogen-Bond Interactions. *Journal of Chemical Theory and Computation 5*, 86–96.

(*122*) Suhr Kirketerp, M.-B., Åxman Petersen, M., Wanko, M., Andres Espinosa Leal, L., Zettergren, H., Raymo, F. M., Rubio, A., Brøndsted Nielsen, M., and Brøndsted Nielsen, S. (2009). Absorption Spectra of 4-Nitrophenolate Ions Measured in Vacuo and in Solution. *ChemPhysChem 10*, 1207–1209.

(*123*) Sim, E., Song, S., and Burke, K. (2018). Quantifying Density Errors in DFT. *The Journal of Physical Chemistry Letters 9*, 6385–6392.

(*124*) Chantzis, A., Laurent, A. D., Adamo, C., and Jacquemin, D. (2013). Is the Tamm-Dancoff Approximation Reliable for the Calculation of Absorption and Fluorescence Band Shapes? *Journal of Chemical Theory and Computation 9*, 4517–4525.

(*125*) Takezaki, M., Hirota, N., and Terazima, M. (1997). Nonradiative Relaxation Processes and Electronically Excited States of Nitrobenzene Studied by Picosecond Time-Resolved Transient Grating Method. *The Journal of Physical Chemistry A 101*, 3443–3448.

(*126*) Xu, C., Yu, L., Zhu, C., Yu, J., and Cao, Z. (2016). Intersystem crossing-branched excited-state intramolecular proton transfer for o-nitrophenol: An ab initio on-the-fly nonadiabatic molecular dynamic simulation. *Scientific Reports 6*, 26768.

(*127*) Hurley, R., and Testa, A. C. (1968). Triplet-state yield of aromatic nitro compounds. *Journal of the American Chemical Society 90*, 1949–1952.

(*128*) Vogt, R. A., Reichardt, C., and Crespo-Hernández, C. E. (2013). Excited-State Dynamics in Nitro-Naphthalene Derivatives: Intersystem Crossing to the Triplet Manifold in Hundreds of Femtoseconds. *The Journal of Physical Chemistry A 117*, 6580–6588.

(*129*) Crespo-Hernández, C. E., Burdzinski, G., and Arce, R. (2008). Environmental Photochemistry of Nitro-PAHs: Direct Observation of Ultrafast Intersystem Crossing in 1-Nitropyrene. *The Journal of Physical Chemistry A 112*, 6313–6319.

(*130*) Zugazagoitia, J. S., Collado-Fregoso, E., Plaza-Medina, E. F., and Peon, J. (2009). Relaxation in the Triplet Manifold of 1-Nitronaphthalene Observed by Transient Absorption Spectroscopy. *The Journal of Physical Chemistry A 113*, 805–810.

(*131*) Takezaki, M., Hirota, N., Terazima, M., Sato, H., Nakajima, T., and Kato, S. (1997). Geometries and Energies of Nitrobenzene Studied by CAS-SCF Calculations. *The Journal of Physical Chemistry A 101*, 5190–5195.

(*132*) McNeill, K., and Canonica, S. (2016). Triplet state dissolved organic matter in aquatic photochemistry: reaction mechanisms, substrate scope, and photophysical properties. *Environmental Science: Processes & Impacts 18*, 1381–1399.

(*133*) Blackshaw, K. J. et al. (2019). Nonstatistical Dissociation Dynamics of Nitroaromatic Chromophores. *The Journal of Physical Chemistry A 123*, 4262–4273.

(*134*) Hashimoto, S., Sunamoto, J., Fujii, H., and Kano, K. (1968). Photochemical Reduction of Nitrobenzene and Its Reduction Intermediates. III. The Photochemical Reduction of Nitrobenzene. *Bulletin of the Chemical Society of Japan 41*, 1249–1251.

(*135*) Hashimoto, S., and Kano, K. (1972). The Photochemical Reduction of Nitrobenzene and Its Reduction Intermediates. X. The Photochemical Reduction of the Monosubstituted Nitrobenzenes in 2-Propanol. *Bulletin of the Chemical Society of Japan 45*, 549–553.

(*136*) Gervasi, N. R., Topping, D. O., and Zuend, A. (2020). A predictive group-contribution model for the viscosity of aqueous organic aerosol. *Atmospheric Chemistry and Physics 20*, 2987–3008.

(*137*) Reid, J. P., Bertram, A. K., Topping, D. O., Laskin, A., Martin, S. T., Petters, M. D., Pope, F. D., and Rovelli, G. (2018). The viscosity of atmospherically relevant organic particles. *Nature Communications 9*, 956.

(*138*) Bateman, A. P., Bertram, A. K., and Martin, S. T. (2015). Hygroscopic Influence on the Semisolid-to-Liquid Transition of Secondary Organic Materials. *The Journal of Physical Chemistry A 119*, 4386–4395.

(*139*) Renbaum-Wolff, L., Grayson, J. W., Bateman, A. P., Kuwata, M., Sellier, M., Murray, B. J., Shilling, J. E., Martin, S. T., and Bertram, A. K. (2013). Viscosity of -pinene secondary organic material and implications for particle growth and reactivity. *Proceedings of the National Academy of Sciences 110*, 8014–8019.

(*140*) Kidd, C., Perraud, V., Wingen, L. M., and Finlayson-Pitts, B. J. (2014). Integrating phase and composition of secondary organic aerosol from the ozonolysis of -pinene. *Proceedings of the National Academy of Sciences 111*, 7552–7557.

(*141*) Maclean, A. M., Smith, N. R., Li, Y., Huang, Y., Hettiyadura, A. P. S., Crescenzo, G. V., Shiraiwa, M., Laskin, A., Nizkorodov, S. A., and Bertram, A. K. (2021). Humidity-Dependent Viscosity of Secondary Organic Aerosol from Ozonolysis of -Caryophyllene: Measurements, Predictions, and Implications. *ACS Earth and Space Chemistry 5*, 305–318.

(*142*) Zaveri, R. A. et al. (2018). Growth Kinetics and Size Distribution Dynamics of Viscous Secondary Organic Aerosol. *Environmental Science & Technology 52*, 1191–1199.

(*143*) Wang, B., O'Brien, R. E., Kelly, S. T., Shilling, J. E., Moffet, R. C., Gilles, M. K., and Laskin, A. (2015). Reactivity of Liquid and Semisolid Secondary Organic Carbon with Chloride and Nitrate in Atmospheric Aerosols. *The Journal of Physical Chemistry A 119*, 4498–4508.

(*144*) Shiraiwa, M., Ammann, M., Koop, T., and Pöschl, U. (2011). Gas uptake and chemical aging of semisolid organic aerosol particles. *Proceedings of the National Academy of Sciences 108*, 11003–11008.

(*145*) M. Power, R., H. Simpson, S., P. Reid, J., and J. Hudson, A. (2013). The transition from liquid to solid-like behaviour in ultrahigh viscosity aerosol particles. *Chemical Science 4*, 2597–2604.

(*146*) Rothfuss, N. E., and Petters, M. D. (2016). Coalescence-based assessment of aerosol phase state using dimers prepared through a dual-differential mobility analyzer technique. *Aerosol Science and Technology 50*, 1294–1305.

(*147*) Vaden, T. D., Imre, D., Beránek, J., Shrivastava, M., and Zelenyuk, A. (2011). Evaporation kinetics and phase of laboratory and ambient secondary organic aerosol. *Proceedings of the National Academy of Sciences 108*, 2190–2195.

(*148*) Perraud, V. et al. (2012). Nonequilibrium atmospheric secondary organic aerosol formation and growth. *Proceedings of the National Academy of Sciences 109*, 2836–2841.

(*149*) Wall, A. C. V., Perraud, V., M. Wingen, L., and J. Finlayson-Pitts, B. (2020). Evidence for a kinetically controlled burying mechanism for growth of high viscosity secondary organic aerosol. *Environmental Science: Processes & Impacts 22*, 66–83.

(*150*) Yli-Juuti, T. et al. (2017). Factors controlling the evaporation of secondary organic aerosol from -pinene ozonolysis. *Geophysical Research Letters 44*, 2562–2570.

(*151*) Al-Naiema, I. M., Offenberg, J. H., Madler, C. J., Lewandowski, M., Kettler, J., Fang, T., and Stone, E. A. (2020). Secondary organic aerosols from aromatic hydrocarbons and their contribution to fine particulate matter in Atlanta, Georgia. *Atmospheric Environment 223*, 117227.

(*152*) Yuan, W. et al. (2021). Measurement report: $PM_{2.5}$-bound nitrated aromatic compounds in Xi'an, Northwest China – seasonal variations and contributions to optical properties of brown carbon. *Atmospheric Chemistry and Physics 21*, 3685–3697.

(*153*) Lin, P., Liu, J., Shilling, J. E., Kathmann, S. M., Laskin, J., and Laskin, A. (2015). Molecular characterization of brown carbon (BrC) chromophores in secondary organic aerosol generated from photo-oxidation of toluene. *Physical Chemistry Chemical Physics 17*, 23312–23325.

(*154*) Nagarajan, K., R. Mallia, A., Muraleedharan, K., and Hariharan, M. (2017). Enhanced intersystem crossing in core-twisted aromatics. *Chemical Science 8*, 1776–1782.

(*155*) Alpert, P. A. et al. (2021). Photolytic radical persistence due to anoxia in viscous aerosol particles. *Nature Communications 12*, 1769.

(*156*) Kiland, K. J., Maclean, A. M., Kamal, S., and Bertram, A. K. (2019). Diffusion of Organic Molecules as a Function of Temperature in a Sucrose Matrix (a Proxy for Secondary Organic Aerosol). *The Journal of Physical Chemistry Letters 10*, 5902–5908.

(*157*) H. Marshall, F., Berkemeier, T., Shiraiwa, M., Nandy, L., B. Ohm, P., S. Dutcher, C., and P. Reid, J. (2018). Influence of particle viscosity on mass transfer and heterogeneous ozonolysis kinetics in aqueous–sucrose–maleic acid aerosol. *Physical Chemistry Chemical Physics 20*, 15560–15573.

(*158*) Russell, L. M., Hawkins, L. N., Frossard, A. A., Quinn, P. K., and Bates, T. S. (2010). Carbohydrate-like composition of submicron atmospheric particles and their production from ocean bubble bursting. *Proceedings of the National Academy of Sciences 107*, 6652–6657.

(*159*) Simoneit, B. R. T., Elias, V. O., Kobayashi, M., Kawamura, K., Rushdi, A. I., Medeiros, P. M., Rogge, W. F., and Didyk, B. M. (2004). SugarsDominant Water-Soluble Organic Compounds in Soils and Characterization as Tracers in Atmospheric Particulate Matter. *Environmental Science & Technology 38*, 5939–5949.

(*160*) Sentko, A., and Willibald-Ettle, I. In *Sweeteners and Sugar Alternatives in Food Technology*, 2012, pp 243–274.

(*161*) Cammenga, H. K., and Zielasko, B. (1996). Thermal behaviour of isomalt. *Thermochimica Acta 271*, 149–153.

(*162*) Nothnagel, E. A., and Zitter, R. N. (1976). The pH dependence of the ultraviolet and visible absorption and the resonance Raman spectra of 4-nitro-1,2-benzenediol in aqueous solution. *The Journal of Physical Chemistry 80*, 722–727.

(*163*) Ossola, R., Jönsson, O. M., Moor, K., and McNeill, K. (2021). Singlet Oxygen Quantum Yields in Environmental Waters. *Chemical Reviews 121*, 4100–4146.

(*164*) Corral Arroyo, P., Bartels-Rausch, T., Alpert, P. A., Dumas, S., Perrier, S., George, C., and Ammann, M. (2018). Particle-Phase Photosensitized Radical Production and Aerosol Aging. *Environmental Science & Technology 52*, 7680–7688.

(*165*) Lian, H.-Z., Wei, Y.-N., Liu, W.-W., and Li, D.-D. (2006). HPLC-UV Detection for Analysis of p-Benzoquinone Dioxime and p-Nitrosophenol, and Chromatographic Fingerprint Applied in Quality Control of Industrial p-Benzoquinone Dioxime. *Journal of Liquid Chromatography & Related Technologies 29*, 509–520.

(*166*) Dewar, M. J. S., Kubba, V. P., and Pettit, R. (1958). 625. New heteroaromatic compounds. Part II. Boron compounds isoconjugate with indole, 2 : 3-benzofuran, and thionaphthen. *Journal of the Chemical Society (Resumed)*, 3076–3079.

(*167*) Martynoff, M. (1949). Note de laboratoire: Spectres d'absorption de quelques p-quinones. *16*, 258–261.

(*168*) Xia, Q., Yin, J.-J., Zhao, Y., Wu, Y.-S., Wang, Y.-Q., Ma, L., Chen, S., Sun, X., Fu, P. P., and Yu, H. (2013). UVA Photoirradiation of Nitro-Polycyclic Aromatic Hydrocarbons—Induction of Reactive Oxygen Species and Formation of Lipid Peroxides †. *International Journal of Environmental Research and Public Health 10*, 1062–1084.

(*169*) Renard, P., Reed Harris, A. E., Rapf, R. J., Ravier, S., Demelas, C., Coulomb, B., Quivet, E., Vaida, V., and Monod, A. (2014). Aqueous Phase Oligomerization of Methyl Vinyl Ketone by Atmospheric Radical Reactions. *The Journal of Physical Chemistry C 118*, 29421–29430.

(*170*) Vidović, K., Kroflič, A., Šala, M., and Grgić, I. (2020). Aqueous-Phase Brown Carbon Formation from Aromatic Precursors under Sunlight Conditions. *Atmosphere 11*, 131.

(*171*) Xie, M., Chen, X., Hays, M. D., Lewandowski, M., Offenberg, J., Kleindienst, T. E., and Holder, A. L. (2017). Light Absorption of Secondary Organic Aerosol: Composition and Contribution of Nitroaromatic Compounds. *Environmental Science & Technology 51*, 11607–11616.

(*172*) Nitta, Y., Schalk, O., Kaneshima, K., and Sekikawa, T. (2019). Ultrafast Photolysis of o-Nitrophenol Studied by Time-Resolved Photoelectron Spectroscopy. *EPJ Web of Conferences 205*, ed. by Cerullo, G., Ogilvie, J., Kärtner, F., Khalil, M., and Li, R., 09022.

(*173*) Nitta, Y., Schalk, O., Igarashi, H., Wada, S., Tsutsumi, T., Saita, K., Taketsugu, T., and Sekikawa, T. (2021). Real-Time Probing of an Atmospheric Photochemical Reaction by Ultrashort Extreme Ultraviolet Pulses: Nitrous Acid Release from o-Nitrophenol. *The Journal of Physical Chemistry Letters 12*, 674–679.

(*174*) Bailey-Darland, S., Krueger, T. D., and Fang, C. (2023). Ultrafast Spectroscopies of Nitrophenols and Nitrophenolates in Solution: From Electronic Dynamics and Vibrational Structures to Photochemical and Environmental Implications. *Molecules 28*, 601.

(*175*) Ciamician, G., and Silber, P. (1886). Ueber die Einwirkung des Lichtes auf eine alkoholische Nitrobenzollösung. *Berichte der deutschen chemischen Gesellschaft 19*, 2899–2900.

(*176*) Barltrop, J. A., and Bunce, N. J. (1968). Organic photochemistry. Part VIII. The photochemical reduction of nitro-compounds. *Journal of the Chemical Society C: Organic*, 1467–1474.

(*177*) Dalton, A. B., Le, S. M., Karimova, N. V., Gerber, R. B., and Nizkorodov, S. A. (2023). Influence of solvent on the electronic structure and the photochemistry of nitrophenols. *Environmental Science: Atmospheres 3*, 257–267.

(*178*) Krishnan, R., Binkley, J. S., Seeger, R., and Pople, J. A. (1980). Self-consistent molecular orbital methods. XX. A basis set for correlated wave functions. *The Journal of Chemical Physics 72*, 650–654.

(*179*) Schmidt, K. et al. (2007). Intersystem Crossing Processes in Nonplanar Aromatic Heterocyclic Molecules. *The Journal of Physical Chemistry A 111*, 10490–10499.

(*180*) Guo, S., and Li, H. (2023). Photolysis of nitrophenols in gas phase and aqueous environment: a potential daytime source for atmospheric nitrous acid (HONO). *Environmental Science: Atmospheres 3*, 143–155.

(*181*) Furche, F., and Ahlrichs, R. (2002). Adiabatic time-dependent density functional methods for excited state properties. *The Journal of Chemical Physics 117*, 7433–7447.

(*182*) Wang, J., and Durbeej, B. (2020). How accurate are TD-DFT excited-state geometries compared to DFT ground-state geometries? *Journal of Computational Chemistry 41*, 1718–1729.

(*183*) Quenneville, J., Greenfield, M., Moore, D. S., McGrane, S. D., and Scharff, R. J. (2011). Quantum Chemistry Studies of Electronically Excited Nitrobenzene, TNA, and TNT. *The Journal of Physical Chemistry A 115*, 12286–12297.

(*184*) Cammi, R., Mennucci, B., and Tomasi, J. (2000). Fast Evaluation of Geometries and Properties of Excited Molecules in Solution: A Tamm-Dancoff Model with Application to 4-Dimethylaminobenzonitrile. *The Journal of Physical Chemistry A 104*, 5631–5637.

(*185*) Wang, Y.-L., and Wu, G.-S. (2008). Improving the TDDFT calculation of low-lying excited states for polycyclic aromatic hydrocarbons using the Tamm–Dancoff approximation. *International Journal of Quantum Chemistry 108*, 430–439.

(*186*) Risthaus, T., Hansen, A., and Grimme, S. (2014). Excited states using the simplified Tamm–Dancoff-Approach for range-separated hybrid density functionals: development and application. *Physical Chemistry Chemical Physics 16*, 14408–14419.

(*187*) Rather, S. R., Yadav, R., and Sen, P. (2011). Femtosecond Excited-State Dynamics of 4-Nitrophenyl Pyrrolidinemethanol: Evidence of Twisted Intramolecular Charge Transfer and Intersystem Crossing Involving the Nitro Group. *The Journal of Physical Chemistry A 115*, 8335–8343.

(*188*) El-Sayed, M. A. (1963). Spin—Orbit Coupling and the Radiationless Processes in Nitrogen Heterocyclics. *The Journal of Chemical Physics 38*, 2834–2838.

(*189*) Shizu, K., and Kaji, H. (2021). Theoretical Determination of Rate Constants from Excited States: Application to Benzophenone. *The Journal of Physical Chemistry A 125*, 9000–9010.

(*190*) Marian, C. M. (2021). Understanding and Controlling Intersystem Crossing in Molecules. *Annual Review of Physical Chemistry 72*, 617–640.

(*191*) Sousa, C., Domingo, A., and de Graaf, C. (2018). Effect of Second-Order Spin–Orbit Coupling on the Interaction between Spin States in Spin-Crossover Systems. *Chemistry – A European Journal 24*, 5146–5152.

(*192*) Penfold, T. J., Gindensperger, E., Daniel, C., and Marian, C. M. (2018). Spin-Vibronic Mechanism for Intersystem Crossing. *Chemical Reviews 118*, 6975–7025.

(*193*) Yanai, T., Tew, D. P., and Handy, N. C. (2004). A new hybrid exchange–correlation functional using the Coulomb-attenuating method (CAM-B3LYP). *Chemical Physics Letters 393*, 51–57.

(*194*) Kobayashi, R., and Amos, R. D. (2006). The application of CAM-B3LYP to the charge-transfer band problem of the zincbacteriochlorin–bacteriochlorin complex. *Chemical Physics Letters 420*, 106–109.

(*195*) Komjáti, B., Urai, Á., Hosztafi, S., Kökösi, J., Kováts, B., Nagy, J., and Horváth, P. (2016). Systematic study on the TD-DFT calculated electronic circular dichroism spectra of chiral aromatic nitro compounds: A comparison of B3LYP and CAM-B3LYP. *Spectrochimica Acta Part A: Molecular and Biomolecular Spectroscopy 155*, 95–102.

(*196*) Pines, E., Pines, D., Barak, T., Magnes, B.-Z., Tolbert, L. M., and Haubrich, J. E. (1998). Isotope and temperature effects in ultrafast proton-transfer from a strong excited-state acid. *Berichte der Bunsengesellschaft für physikalische Chemie 102*, 511–517.

(*197*) Arnaut, L. G., and Formosinho, S. J. (1993). Excited-state proton transfer reactions I. Fundamentals and intermolecular reactions. *Journal of Photochemistry and Photobiology A: Chemistry 75*, 1–20.

(*198*) Tolbert, L. M., and Solntsev, K. M. (2002). Excited-State Proton Transfer: From Constrained Systems to "Super" Photoacids to Superfast Proton Transfer. *Accounts of Chemical Research 35*, 19–27.

(*199*) Simkovitch, R., Karton-Lifshin, N., Shomer, S., Shabat, D., and Huppert, D. (2013). Ultrafast Excited-State Proton Transfer to the Solvent Occurs on a Hundred-Femtosecond Time-Scale. *The Journal of Physical Chemistry A 117*, 3405–3413.

(*200*) Englman, R., and Jortner, J. (1970). The energy gap law for radiationless transitions in large molecules. *Molecular Physics 18*, 145–164.

(*201*) Orozco-Gonzalez, Y., Coutinho, K., Peon, J., and Canuto, S. (2012). Theoretical study of the absorption and nonradiative deactivation of 1-nitronaphthalene in the low-lying singlet and triplet excited states including methanol and ethanol solvent effects. *The Journal of Chemical Physics 137*, 054307.

(*202*) Samanta, P. K., Kim, D., Coropceanu, V., and Brédas, J.-L. (2017). Up-Conversion Intersystem Crossing Rates in Organic Emitters for Thermally Activated Delayed Fluorescence: Impact of the Nature of Singlet vs Triplet Excited States. *Journal of the American Chemical Society 139*, 4042–4051.

(*203*) Aizawa, N., Harabuchi, Y., Maeda, S., and Pu, Y.-J. (2020). Kinetic prediction of reverse intersystem crossing in organic donor–acceptor molecules. *Nature Communications 11*, 3909.

(*204*) Garain, B. C., Samanta, P. K., and Pati, S. K. (2021). Intersystem Crossing in Boron-Based Donor–Spiro–Acceptor Organic Chromophore: A Detailed Theoretical Study. *The Journal of Physical Chemistry A 125*, 6674–6680.

(*205*) Serdiuk, I. E., Mońka, M., Kozakiewicz, K., Liberek, B., Bojarski, P., and Park, S. Y. (2021). Vibrationally Assisted Direct Intersystem Crossing between the Same Charge-Transfer States for Thermally Activated Delayed Fluorescence: Analysis by Marcus–Hush Theory Including Reorganization Energy. *The Journal of Physical Chemistry B 125*, 2696–2706.

(*206*) Bhandari, S., Sarkar, S., Schubert, A., Yamada, A., Payne, J., Ptaszek, M., Geva, E., and Dunietz, B. D. (2021). Intersystem Crossing in Tetrapyrrolic Macrocycles. A First-Principles Analysis. *The Journal of Physical Chemistry C 125*, 13493–13500.

(*207*) Yip, R. W., Sharma, D. K., Giasson, R., and Gravel, D. (1984). Picosecond excited-state absorption of alkylnitrobenzenes in solution. *The Journal of Physical Chemistry 88*, 5770–5772.

(*208*) Takezaki, M., Hirota, N., and Terazima, M. (1998). Relaxation of nitrobenzene from the excited singlet state. *The Journal of Chemical Physics 108*, 4685–4686.

(*209*) Thurston, R., Brister, M. M., Tan, L. Z., Champenois, E. G., Bakhti, S., Muddukrishna, P., Weber, T., Belkacem, A., Slaughter, D. S., and Shivaram, N. (2020). Ultrafast Dynamics of Excited Electronic States in Nitrobenzene Measured by Ultrafast Transient Polarization Spectroscopy. *The Journal of Physical Chemistry A 124*, 2573–2579.

(*210*) Saalbach, L., Kotsina, N., Crane, S. W., Paterson, M. J., and Townsend, D. (2021). Ultraviolet Excitation Dynamics of Nitrobenzenes. *The Journal of Physical Chemistry A 125*, 7174–7184.

(*211*) Crane, S. W., Garrow, M., Lane, P. D., Robertson, K., Waugh, A., Woolley, J. M., Stavros, V. G., Paterson, M. J., Greaves, S. J., and Townsend, D. (2023). The Value of Different Experimental Observables: A Transient Absorption Study of the Ultraviolet Excitation Dynamics Operating in Nitrobenzene. *The Journal of Physical Chemistry A 127*, 6425–6436.

(*212*) Lau, N. A. et al. (2024). Unraveling the Ultrafast Photochemical Dynamics of Nitrobenzene in Aqueous Solution. *Journal of the American Chemical Society 146*, 10407–10417.

(*213*) Krishnakumar, S., Das, A. K., Singh, P. J., Shastri, A., and Rajasekhar, B. N. (2016). Experimental and computational studies on the electronic excited states of nitrobenzene. *Journal of Quantitative Spectroscopy and Radiative Transfer 184*, 89–99.

(*214*) Giussani, A., and Worth, G. A. (2017). Insights into the Complex Photophysics and Photochemistry of the Simplest Nitroaromatic Compound: A CASPT2//CASSCF Study on Nitrobenzene. *Journal of Chemical Theory and Computation 13*, 2777–2788.

(*215*) Dalton, A. B., Fishman, D. A., and Nizkorodov, S. A. (2023). Ultrafast Excited-State Proton Transfer in 4-Nitrocatechol: Implications for the Photochemistry of Nitrophenols. *The Journal of Physical Chemistry A 127*, 8307–8315.

(*216*) Rohrdanz, M. A., Martins, K. M., and Herbert, J. M. (2009). A long-range-corrected density functional that performs well for both ground-state properties and time-dependent density functional theory excitation energies, including charge-transfer excited states. *The Journal of Chemical Physics 130*, 054112.

(*217*) Dunning, T. H., Jr. (1989). Gaussian basis sets for use in correlated molecular calculations. I. The atoms boron through neon and hydrogen. *The Journal of Chemical Physics 90*, 1007–1023.

(*218*) Sinha, H. K., and Yates, K. (1990). Ground- and excited-state dipole moments of some nitroaromatics: Evidence for extensive charge transfer in twisted nitrobenzene systems. *The Journal of Chemical Physics 93*, 7085–7093.

(*219*) Gould, I. R., Boiani, J. A., Gaillard, E. B., Goodman, J. L., and Farid, S. (2003). Intersystem Crossing in Charge-Transfer Excited States. *The Journal of Physical Chemistry A 107*, 3515–3524.

(*220*) Paul, L., Chakrabarti, S., and Ruud, K. (2017). Anomalous Phosphorescence from an Organometallic White-Light Phosphor. *The Journal of Physical Chemistry Letters 8*, 4893–4897.

(*221*) Xu, S., Yang, Q., Wan, Y., Chen, R., Wang, S., Si, Y., Yang, B., Liu, D., Zheng, C., and Huang, W. (2019). Predicting intersystem crossing efficiencies of organic molecules for efficient thermally activated delayed fluorescence. *Journal of Materials Chemistry C 7*, 9523–9530.

(*222*) Li, K., Tong, G. S. M., Yuan, J., Ma, C., Du, L., Yang, C., Kwok, W.-M., Phillips, D. L., and Che, C.-M. (2020). Excitation-Wavelength-Dependent and Auxiliary-Ligand-Tuned Intersystem-Crossing Efficiency in Cyclometalated Platinum(II) Complexes: Spectroscopic and Theoretical Studies. *Inorganic Chemistry 59*, 14654–14665.

(*223*) Zahariev, T., Shandurkov, D., Gutzov, S., Trendafilova, N., Enseling, D., Jüstel, T., and Georgieva, I. (2021). Phenanthroline chromophore as efficient antenna for Tb3+ green luminescence: A theoretical study. *Dyes and Pigments 185*, 108890.

(*224*) Shi, L., Xie, X., and Troisi, A. (2022). Rapid calculation of internal conversion and intersystem crossing rate for organic materials discovery. *The Journal of Chemical Physics 157*, 134106.

(*225*) Maria, S. F., Russell, L. M., Gilles, M. K., and Myneni, S. C. B. (2004). Organic Aerosol Growth Mechanisms and Their Climate-Forcing Implications. *Science 306*, 1921–1924.

(*226*) Hoyle, C. R., Myhre, G., Berntsen, T. K., and Isaksen, I. S. A. (2009). Anthropogenic influence on SOA and the resulting radiative forcing. *Atmospheric Chemistry and Physics 9*, 2715–2728.

(*227*) Spracklen, D. V. et al. (2011). Aerosol mass spectrometer constraint on the global secondary organic aerosol budget. *Atmospheric Chemistry and Physics 11*, 12109–12136.

(*228*) Li, K. et al. (2017). Enhanced Light Scattering of Secondary Organic Aerosols by Multiphase Reactions. *Environmental Science & Technology 51*, 1285–1292.

(*229*) Aiona, P. K., Luek, J. L., Timko, S. A., Powers, L. C., Gonsior, M., and Nizkorodov, S. A. (2018). Effect of Photolysis on Absorption and Fluorescence Spectra of Light-Absorbing Secondary Organic Aerosols. *ACS Earth and Space Chemistry 2*, 235–245.

(*230*) Zahardis, J., and Petrucci, G. A. (2007). The oleic acid-ozone heterogeneous reaction system: products, kinetics, secondary chemistry, and atmospheric implications of a model system – a review. *Atmospheric Chemistry and Physics 7*, 1237–1274.

(*231*) Murray, B. J. (2008). Inhibition of ice crystallisation in highly viscous aqueous organic acid droplets. *Atmospheric Chemistry and Physics 8*, 5423–5433.

(*232*) Berkemeier, T., Shiraiwa, M., Pöschl, U., and Koop, T. (2014). Competition between water uptake and ice nucleation by glassy organic aerosol particles. *Atmospheric Chemistry and Physics 14*, 12513–12531.

(*233*) Schill, G. P., De Haan, D. O., and Tolbert, M. A. (2014). Heterogeneous Ice Nucleation on Simulated Secondary Organic Aerosol. *Environmental Science & Technology 48*, 1675–1682.

(*234*) Edwards, P. M. et al. (2017). Transition from high- to low-NOx control of night-time oxidation in the southeastern US. *Nature Geoscience 10*, 490–495.

(*235*) Joo, T., Rivera-Rios, J. C., Takeuchi, M., Alvarado, M. J., and Ng, N. L. (2019). Secondary Organic Aerosol Formation from Reaction of 3-Methylfuran with Nitrate Radicals. *ACS Earth and Space Chemistry 3*, 922–934.

(*236*) He, Q. et al. (2021). Optical Properties of Secondary Organic Aerosol Produced by Nitrate Radical Oxidation of Biogenic Volatile Organic Compounds. *Environmental Science & Technology 55*, 2878–2889.

(*237*) Baboomian, V. J., He, Q., Montoya-Aguilera, J., Ali, N., Fleming, L. T., Lin, P., Laskin, A., Laskin, J., Rudich, Y., and Nizkorodov, S. A. (2023). Light absorption and scattering properties of indole secondary organic aerosol prepared under various oxidant and relative humidity conditions. *Aerosol Science and Technology 57*, 532–545.

(*238*) Jiang, F., Siemens, K., Linke, C., Li, Y., Gong, Y., Leisner, T., Laskin, A., and Saathoff, H. (2024). Molecular analysis of secondary organic aerosol and brown carbon from the oxidation of indole. *Atmospheric Chemistry and Physics 24*, 2639–2649.

(*239*) Ng, N. L. et al. (2008). Secondary organic aerosol (SOA) formation from reaction of isoprene with nitrate radicals (NO_3). *Atmospheric Chemistry and Physics 8*, 4117–4140.

(*240*) Fry, J. L. et al. (2014). Secondary Organic Aerosol Formation and Organic Nitrate Yield from NO3 Oxidation of Biogenic Hydrocarbons. *Environmental Science & Technology 48*, 11944–11953.

(*241*) Yan, J., Wang, X., Gong, P., and Wang, C. (2021). Nitrated polycyclic aromatic compounds in the atmospheric environment: A review. *Critical Reviews in Environmental Science and Technology 51*, 1159–1185.

(*242*) Atkinson, R., Tuazon, E. C., Arey, J., and Aschmann, S. M. (1995). Atmospheric and indoor chemistry of gas-phase indole, quinoline, and isoquinoline. *Atmospheric Environment 29*, 3423–3432.

(*243*) Su, X. F., Huang, W., and Wu, H. Y. (2014). Assessment of PBE0 Calculation of C-NO2 Bond Dissociation Energies for Nitroaromatic System. *Advanced Materials Research 915-916*, 675–678.

(*244*) Barckholtz, C., Barckholtz, T. A., and Hadad, C. M. (1999). CH and NH Bond Dissociation Energies of Small Aromatic Hydrocarbons. *Journal of the American Chemical Society 121*, 491–500.

(*245*) Blank, D. A., North, S. W., and Lee, Y. T. (1994). The ultraviolet photodissociation dynamics of pyrrole. *Chemical Physics 187*, 35–47.

(*246*) Wallace, W. E. In *NIST Chemistry WebBook, NIST Standard Reference Database Number 69*.

(*247*) Atkinson, R. (1991). Kinetics and Mechanisms of the Gas-Phase Reactions of the NO3 Radical with Organic Compounds. *Journal of Physical and Chemical Reference Data 20*, 459–507.

(*248*) Ren, Y., Zhou, L., Mellouki, A., Daële, V., Idir, M., Brown, S. S., Ruscic, B., Paton, R. S., McGillen, M. R., and Ravishankara, A. R. (2021). Reactions of NO_3 with aromatic aldehydes: gas-phase kinetics and insights into the mechanism of the reaction. *Atmospheric Chemistry and Physics 21*, 13537–13551.

(*249*) Mayorga, R., Chen, K., Raeofy, N., Woods, M., Lum, M., Zhao, Z., Zhang, W., Bahreini, R., Lin, Y.-H., and Zhang, H. (2022). Chemical Structure Regulates the Formation of Secondary Organic Aerosol and Brown Carbon in Nitrate Radical Oxidation of Pyrroles and Methylpyrroles. *Environmental Science & Technology 56*, 7761–7770.

(*250*) Li, Y., Vaz, R. J., Olson, S. H., Munson, M., Paras, N. A., and Conrad, J. (2020). Selectivity in the Addition of Electron-Deficient Radicals to the C2 Position of Indoles. *European Journal of Organic Chemistry 2020*, 5828–5832.

(*251*) Piletic, I. R., Edney, E. O., and Bartolotti, L. J. (2017). Barrierless Reactions with Loose Transition States Govern the Yields and Lifetimes of Organic Nitrates Derived from Isoprene. *The Journal of Physical Chemistry A 121*, 8306–8321.

Appendix A

DaltonView: TDDFT Visualization Software

Overview

DaltonView is an executable application developed in Python which can be used as a data visualization tool for time-dependent density functional theory (TDDFT) calculations. It is available both as standalone Python code and packaged as an executable program, allowing for the program to run on machines which do not have Python installed. The front-end of the application uses the widget-based Tk library. The back-end of the code employs *regular expressions* to extract numerical data from the text file, generating a spectrum using these numerical values.

The purpose of DaltonView is to generate excitation spectra (also known as absorption spectra) from TDDFT output files. The ability for the program to automatically fetch data can be a great time-saver when trying to analyze numerous output files, however it does not make this program novel. IQmol is a common tool used to analyze output files from quantum chemical calculations and is capable of tabulating and visualizing data out of TDDFT outputs from Q-Chem.

Unfortunately IQmol has limited export options, and only allows the user to save the image itself. Another common quantum chemical program, Gaussian (more specifically its visualization counterpart GaussView), also has built-in capabilities for spectra generation, and affords the user the ability to export their data. Unfortunately, unlike IQmol, Gaussian requires a license and thus may not be readily available on one's personal computer. This problem is compounded by these programs typically only being compatible for output files from their native quantum chemical program. Thus, DaltonView provides a free, open-source alternative to these programs, with the added benefit of being expandable to work with any TDDFT software.

To highlight the utility of processing files with DaltonView, a snippet of a Q-Chem TDDFT output file is provided below. The excitation energies, which are needed to produce an absorption spectrum, are printed hundreds of lines into the output file, and the details of each excitation spans multiple lines. The DaltonView program looks for lines containing "excitation energy (eV)" (line 612) and fetches the first decimal point number in the line, and stores it in its own array. The same is done to retrieve the values "Strength" (line 616) values, saving the user the need to copy-and-paste these values for the tens of states needed to produce an absorption spectrum.

```
609      -----------------------------------------------------
610                  TDDFT Excitation Energies
611      -----------------------------------------------------
612      Excited state   1: excitation energy (eV) =    3.5706
613      Total energy for state  1:              -586.59850571 au
614          Multiplicity: Singlet
615          Trans. Mom.: -1.4447 X   0.0000 Y  -0.4673 Z
616          Strength   :     0.2016803416
617          X: D( 39) --> V(  1) amplitude = -0.2237
618          X: D( 40) --> V(  1) amplitude =  0.9693
```

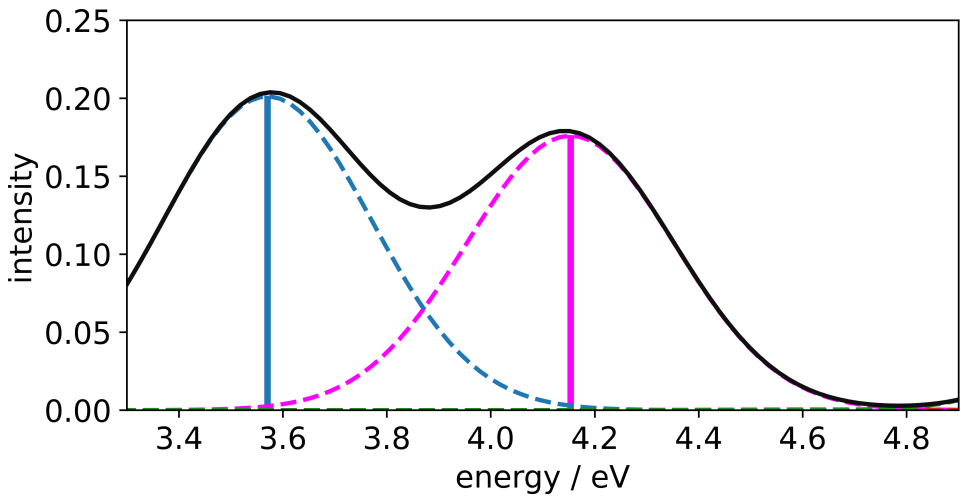

Figure A.1: Illustration of how single excitations are used to generate a simulated absorption spectrum.

The program works by broadening individual excitations into absorption bands with line shape distributions. This principle is illustrated in Fig. A.1. Each peak is generated with either Gaussian distribution (G),

$$G(\lambda) = \frac{f}{\sigma\sqrt{2\pi}} \exp\left(\frac{E - E_{VEE}}{\sqrt{2}\,\sigma}\right)^2, \tag{A.1}$$

or a Cauchy-Lorentz distribution (L),

$$L(\lambda) = \frac{f}{\pi}\left[\frac{\gamma}{(E - E_{VEE})^2 + \gamma^2}\right], \tag{A.2}$$

where in both equations E is a range of energy values (in electron volts), E_{VEE} is the excitation energy from the TDDFT calculation, and f is the oscillator strength of that excitation. In the case of the Cauchy-Lorentz distribution, the half-width at half-maximum (HWHM) is equivalent to the scaling parameter γ. For the Gaussian distribution, HWHM = $\sqrt{2\ln 2}\,\sigma$. The program allows for the user to specify the HWHM values, however, the choice of value is effectively empirical. Additional spectral features are planned for addition in the future, including wavelength depen-

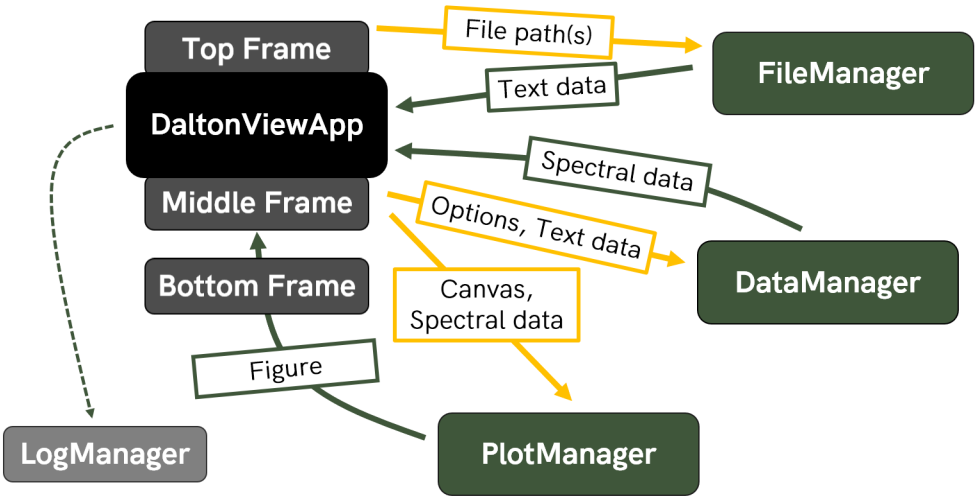

Figure A.2: Schematic illustration of how DaltonView processes a file. The diagram should be read from top to bottom.

dent HWHM values and the option to use a Voigt profile (a convolution of Lorentz and Gaussian functions) for the spectral lines.

To generate the spectrum, the individual peaks (such as the dashed lines in Fig. A.1) are convoluted by summation to generate a complete excitation spectrum. Since the resulting intensities from these spectra are somewhat arbitrary, the spectra are normalized to the maximum value before being displayed, yielding a normalized absorbance of 1 at the wavelength of maximum absorbance. Finally, after convolution of the spectra, the energy axis is converted to a wavelength axis (i.e., electron volts to nanometers).

Program Design

The general workflow of the program is illustrated in Figure A.2. The program is structured into a few individual classes which individually handle certain tasks. The *DaltonViewApp* class handles the graphical user interface (GUI) and acts as the hub of the application. Data processing and visualization are handled by the *FileManager*, *DataManager*, and *PlotManager* classes.

The *FileManager* reads in the input files provided by the user and sends that text data back to the main app. Text data is stored in the app object to avoid having to repeatedly open the same file while the user tweaks the spectral settings. The *DataManager* classes converts the text data into spectral data, using the options specified by the user in the GUI. First, the oscillator strength and vertical excitation energy values are extracted from each transition in the output file. These values are retrieved using *regular expressions*, a pattern matching tool that can be used to retrieve numbers from strings (among many other things).

The *DataManager* class is responsible for using the options specified by the user to compute simulated excitation spectra using the numerical data retrieved from the output file. As of this summary, the options available to the user include peak width (via the HWHM) and the peak shape (either Lorentzian or Gaussian). It is planned to include the ability to scale the HWHM according to the wavelength, since empirically it seems that real absorption bands at long wavelengths tend to have broader peak shapes. The addition of Voigt profiles (a combination of a Lorentzian and a Gaussian) has also been considered, although the scaling of such a peak shape may be overly complicated for simple use of the program.

Finally, once the data has been extracted and converted into a spectrum, the *PlotManager* takes the spectrum and adds it to the existing canvas in the GUI. This is undoubtedly the most inefficient part of the application, however, it tends to run without significant input lag for reasonable wavelength ranges.

Summary

DaltonView is a unique piece of software in that in unites the analysis for various different sources of quantum chemical data. While most of the popular TDDFT software has the ability to compute excitation spectra from output files, most of them are not compatible with output files from

other quantum chemical programs. As an open-source program, DaltonView allows for expansion to include TDDFT outputs from any quantum chemical codes. Another unique feature of this program is the ability for on-the-fly comparisons between theoretical excitation spectra and experimentally measured spectra. Such utility can provide a quantum chemist with rapid conclusions as to the accuracy of their theory. The ability to save images of the spectra allow for a direct pathway for the program to be used toward presentations and publications, potentially resulting in citations in peer-reviewed articles. As of the publication of this dissertation, the program currently supports outputs from Q-Chem, Gaussian, and GAMESS (thanks to Prof. Craig Murray for the latter), with the goal of including other programs and levels of theory in the future through open-source contributions and collaborations.

Appendix B

Cartesian Coordinates of Optimized Geometries of 4-Nitrocatechol

S_0 of 4NC optimized with PBE0/6-311+G(d)

		Coordinates (Angstroms)		
ATOM		X	Y	Z
1	N	-0.0087789546	0.0000100769	-0.0073873130
2	O	-0.0119896222	-0.0000593957	1.2140944359
3	O	1.0142342173	0.0000278806	-0.6754329068
4	C	-1.2794620086	0.0000537640	-0.6990483334
5	C	-2.4564518163	0.0000129367	0.0391570067
6	H	-2.4245271752	-0.0000520670	1.1210796826
7	C	-3.6665249069	0.0000577292	-0.6348455040
8	H	-4.6050710573	0.0000275899	-0.0912095852
9	C	-3.6944914087	0.0001430206	-2.0247791872
10	O	-4.8717819867	0.0001869136	-2.6665503790
11	H	-4.7253624022	0.0002474625	-3.6228406188
12	C	-1.2791504702	0.0001376266	-2.0943705981
13	H	-0.3469528147	0.0001682830	-2.6480857598
14	C	-2.4898322392	0.0001824422	-2.7545422679
15	O	-2.6426119822	0.0002645715	-4.0995957127
16	H	-1.7956110624	0.0002901588	-4.5595309399

S_1 of 4NC optimized with TD/TDA-PBE0/6-311+G(d)

		Coordinates (Angstroms)		
ATOM		X	Y	Z
1	N	0.0346687844	0.0002271697	-0.0975793027
2	O	0.3313157157	1.1333893480	0.4493955220
3	O	0.3296265425	-1.1364080354	0.4441677804
4	C	-1.2120351112	0.0005430255	-0.7780167790
5	C	-2.4111190777	-0.0003058610	-0.0023179166
6	H	-2.3301688292	-0.0006514203	1.0785216154
7	C	-3.6327423641	-0.0006575947	-0.6142358313
8	H	-4.5612855868	-0.0012156253	-0.0555257493
9	C	-3.6849549975	-0.0002493344	-2.0158238431
10	O	-4.8444039415	-0.0005640349	-2.6216021527
11	H	-4.7458261289	-0.0001714758	-3.5881795063
12	C	-1.2371205731	0.0010512410	-2.1594857622
13	H	-0.3173828722	0.0018657354	-2.7348979837
14	C	-2.4675179808	0.0006104898	-2.7925326498
15	O	-2.6754897779	0.0011177810	-4.0967184012
16	H	-1.8606138017	0.0016785914	-4.6177790399

T_1 of 4NC optimized with TD/TDA-PBE0/6-311+G(d)

		Coordinates (Angstroms)		
ATOM		X	Y	Z
1	N	-0.0323754433	-0.0000484005	-0.0324589941
2	O	-0.0654184389	0.0001374622	1.2401959703
3	O	1.0536274997	-0.0000447753	-0.6901186790
4	C	-1.2374189468	0.0000281842	-0.7180047701
5	C	-2.4797191436	0.0001572099	0.0291689390
6	H	-2.4247406003	0.0001710334	1.1090022525
7	C	-3.6818123623	0.0002513345	-0.6187055141
8	H	-4.6166346841	0.0003479488	-0.0694739360
9	C	-3.7192333413	0.0002151267	-2.0191116389
10	O	-4.8755140027	0.0003054714	-2.6598346273
11	H	-4.7510842637	0.0002554206	-3.6214281775
12	C	-1.2439294057	-0.0000243977	-2.1086790506
13	H	-0.3181279611	-0.0001330118	-2.6704115628
14	C	-2.4691691904	0.0000742824	-2.7583319459
15	O	-2.6290922594	0.0000540577	-4.0628740786
16	H	-1.7937074560	-0.0000469465	-4.5528341868

T_2 of 4NC optimized with TD/TDA-PBE0/6-311+G(d)

Coordinates (Angstroms)

ATOM		X	Y	Z
1	N	-0.0440982510	0.0205716136	-0.0439895440
2	O	-0.0782409631	-0.1343166337	1.2303056451
3	O	1.0601009063	0.0776028487	-0.6703509820
4	C	-1.2391900355	0.0106717761	-0.7255259891
5	C	-2.4742494564	0.0185282731	0.0239109980
6	H	-2.4146080916	0.0339291023	1.1036984657
7	C	-3.6822662260	0.0081975034	-0.6200699587
8	H	-4.6148575132	0.0148037301	-0.0681468417
9	C	-3.7192897396	-0.0028968873	-2.0142897532
10	O	-4.8704245468	-0.0063566725	-2.6561442667
11	H	-4.7476019419	-0.0113002614	-3.6180004226
12	C	-1.2419235854	0.0002036828	-2.1083107553
13	H	-0.3160367125	-0.0019882760	-2.6703145691
14	C	-2.4706084070	-0.0034048798	-2.7572398479
15	O	-2.6318070232	-0.0076409763	-4.0571114080
16	H	-1.7992384133	-0.0148939430	-4.5523207704

T_3 of 4NC optimized with TD/TDA-PBE0/6-311+G(d)

		Coordinates (Angstroms)		
ATOM		X	Y	Z
1	N	-0.0495805951	-0.0001661574	-0.0132072108
2	O	0.0628113797	-0.0229059342	1.2663436198
3	O	1.0667368399	0.0292916056	-0.6963005175
4	C	-1.2753733830	-0.0042991614	-0.6861005048
5	C	-2.4611178790	-0.0338862051	0.0401469136
6	H	-2.4420700148	-0.0543318716	1.1221932338
7	C	-3.6702264749	-0.0364316141	-0.6464557168
8	H	-4.6084454747	-0.0591351357	-0.1015184436
9	C	-3.7052349325	-0.0099382303	-2.0365417885
10	O	-4.8941544339	-0.0126103272	-2.6780436744
11	H	-4.7472680564	0.0119577189	-3.6328421865
12	C	-1.2858871080	0.0221464150	-2.0895586160
13	H	-0.3595117332	0.0449600778	-2.6518447836
14	C	-2.5018754723	0.0187223452	-2.7531916618
15	O	-2.6340847743	0.0417878133	-4.1014701886
16	H	-1.7791078874	0.0670386611	-4.5454284744